School of Electrical Engineering, Computing & Mathematical Sciences
Electrical and Computer Engineering

Determination of Noise Temperature and Beam Modelling of an Antenna Array with Example Application using MWA

Daniel Chu Xin Ung

This thesis is presented for the Degree of
Masters of Philosophy
of
Curtin University

October 2019

Declaration

To the best of my knowledge and belief this thesis contains no material previously published by any other person except where due acknowledgement has been made. This thesis contains no material which has been accepted for the award of any other degree or diploma in any university.

Signature: .....

Date: .....

"Wisdom is knowing what you don't know. Humility is admitting that you lack knowledge. Only then the pursuit of knowledge that produces wisdom can begin and the lifelong cycle continues."

- Daniel Ung

Abstract

In this thesis, we presented a framework for the characterization of antenna arrays with special application for phased arrays. Characterization of phased arrays involves the computation of effective area, receiver noise temperature (T_{rcv}), radiation efficiency (η_{rad}) and antenna temperature. We demonstrated that for phased arrays, the classical definition of effective area breaks down and we proposed a physically motivated definition of realised area. These quantities can then be combined to calculate the sensitivity of the array which is inversely proportional to the System Equivalent Flux Density (SEFD).

For the computation of receiver noise temperature, we presented a method predicated upon an existing power wave framework (PWF) and demonstrated that this framework is suitable for calculating the receiver noise temperature of phased arrays. The PWF works by calculating the incoming and outgoing power wave accounting for all coupling paths that exists by using the knowledge of S-parameters and noise correlation matrix of the low-noise amplifier and the array in response to homogeneous isotropic sky.

We calculated the radiation efficiency using a modified version of the Pattern Overlap Integral (POI) method which required the knowledge of the array's impedance mismatch, load impedance, S-parameter and embedded element patterns (EEPs) of the array. In the case of equal load impedances, we showed that the POI simplifies to a simplistic form for quick calculation. The antenna temperature on the other hand, was calculated using the computed realised area and a priori knowledge of sky map.

We verified the derived realised area using a small phased array consisting of four half-wavelength dipoles placed above an infinite perfect electric conductor (PEC) ground plane. We set up two identical systems whereby one was in transmit mode and other in receive mode. We used the transmit case in which all the derived quantities are based on to predict the behaviour of the receiving system. We showed that we can completely predict the behaviour of the receiving system. Using the same test array, we verified the modified POI with classical definition and showed that the results are consistent between the two.

We compared the calculated receiver noise temperature using the proposed PWF against two different methods from current literature and show that all three results are in agreement. We then proceeded to characterize the Murchison Widefield Array (MWA) which is an operational radio telescope located in the Murchison Radio-astronomy Observatory. The realised area and radiation efficiency were computed solely on simulated data, whereas the receiver noise temperature was calculated using a combination of measured noise parameters and S-parameters of the LNA and simulated S-parameters of the MWA tile.

We compared our calculated values of the calculated T_{rcv} and η_{rad} of the MWA tile results obtained via observational drift scan and show agreement between predicted and measured results. As a final comparison, we computed the SEFD of the MWA tile which showed excellent agreement with our observational data.

Acknowledgements

Firstly, I would like to acknowledge my supervisors, Dr. Adrian T. Sutinjo and Dr. David B. Davidson for their constant support and guidance throughout my postgraduate studies. Their kindness, patience, encouragement and willingness to share their knowledge with me has made this thesis possible. I am truly grateful for their input and advises.

I acknowledge Dr. Marcin Sokolowski in collecting and processing data from astronomical observation for the validation of my key results. It was invaluable to have such comparison done and it has contributed to the rigorous testing standards needed to fully support my work.

A special thanks to my loving wife Joanne, my sister Elizabeth and mother Susan for their constant love, encouragement and support throughout my life and especially during my studies. To my Father in Heaven who gave me the strength to continue on despite the challenges and difficulties. He is my companion, rock and constant in times of uncertainty.

I acknowledge the contribution of an Australian Government Research Training Program Scholarship (RTP) in supporting this research. This scientific work makes use of the Murchison Radio-astronomy Observatory, operated by CSIRO. I acknowledge the Wajarri Yamatji people as the traditional owners of the Observatory site. Support for the operation of the MWA is provided by the Australian Government (NCRIS), under a contract to Curtin University administered by Astronomy Australia Limited. I acknowledge the Pawsey Supercomputing Centre which is supported by the Western Australian and Australian Governments.

List of Publications

0.1 Published

- D. Ung, A. Sutinjo, and D. Davidson, "Evaluating receiver noise temperature of a radio telescope in the presence of mutual coupling: Comparison of current methodologies," in 2019 13th European Conference on Antennas and Propagation (EuCAP), March 2019, pp. 1-3.

- D. Ung, A. Sutinjo, D. Davidson, M. Johnston-Hollitt, and S. Tingay, "Radiation efficiency calculation of the Murchison Widefield Array using a power wave based framework," in 2019 IEEE International Symposium on Antennas and Propagation and USNC-URSI Radio Science Meeting, July 2019, pp. 401–402.

0.2 Submitted

- D. Ung, M. Sokolowski, A. T. Sutinjo, and D. B. Davidson, "Noise Temperature of Phased Array Radio Telescope: The Murchison Widefield Array and the Engineering Development Array," Submitted to IEEE Transactions on Antennas and Propagation.

Contents

List of Tables

List of Figures

List of Symbols

Constants

j Imaginary number

k Boltzmann Constant

T_0 Reference temperature

η_0 Characteristic impedance of free space

μ_0 Permeability of free space

π Ratio of circumference to diameter of a circle

ϵ_0 Permittivity of free space

Symbols

Ω_s Solid beam angle

η_{rad} Radiation efficiency (including soil losses)

λ Wavelength in metres

ν Frequency

τ Ratio of delivered to available power (mismatch factor)

Chapter 1

Introduction

1.1 Radio Astronomy

In 1928, Karl Jansky was employed by Bell Telephone Laboratories to investigate electrical disturbance in the form of static hiss that interfered with radio communication [1, 2]. He published his findings in 1932 stating that the static hiss was due to local and distant thunderstorm and contribution from 'unknown origin' whereby, he separated them into three groups: static hiss from 'first, second and third group' respectively [3].

He noted that the static hiss from the third group was faint but nonetheless steady in nature and its direction of arrival gradually changes within a 24 hour period; the signal follows a north-east to north-west trajectory. In consultation with his colleague A. M. Skellet, it was concluded that this steady hiss originates from the Milky Way [1, 4].

It was not until 1941 that Grote Reber picked up Jansky's work and mapped the Milky Way with a 9.6 m diameter dish antenna [5, 6]. That event marked the growth of Radio Astronomy whose seed was planted by Jansky. Fast forward to 2019, radio astronomy has undergone rapid growth whereby the quest for high resolution mapping has led to the development and wide use of radio interferometers.

1.2 Radio Interferometer

Radio telescopes have an angular resolution (radians) that is approximated by [7, Part III]

$$\theta_r \approx \frac{\lambda}{d} \tag{1.1}$$

where λ is the wavelength of the incoming plane wave due to extragalactic object and d (meters) is the diameter of the telescope.

At 160 MHz, Reber's telescope has an angular resolution of approximately 11°. It can be seen that at frequencies in the tens to hundreds of MHz, achieving high angular resolution is increasingly difficult due to the enormous telescope required to be constructed such as the Arecibo Radio Telescope in Puerto Rico [8] and China's Five-hundred-meter Aperture Spherical Telescope (FAST) [9, 10]. This is where radio interferometers have the upper hand.

In this context, a radio interferometer consists of multiple smaller receiving elements that are positioned in a regular or pseudo-random planar configuration as shown in Fig. 1.1. The signals are correlated pairwise and time-averaged. The resolution of the interferometer is also bound by (1.1). However, the parameter d now reflects the longest available baseline. The significance of this is the fact that smaller receiving elements can be combined to form a large radio telescope [11]. A more rigorous analysis on the operation of an interferometer can be found in [12].

Unfortunately, the trade-off is that interferometers only sparsely sample the incoming radio waves which leads to difficulty with reconstructing the radio image for extended sources [11,13]. As a consequence of this, artefacts such as 'negative bowl' appears in the image which leads to a misrepresentation of the sources [14]. This is referred to as the 'short-spacing problem' (SSP). Further discussions of the SSP is beyond the scope of this thesis.

Each of the receiving elements can either be a single dish antenna as seen with the Australian Square Kilometre Array Pathfinder (ASKAP) [15] or a phased

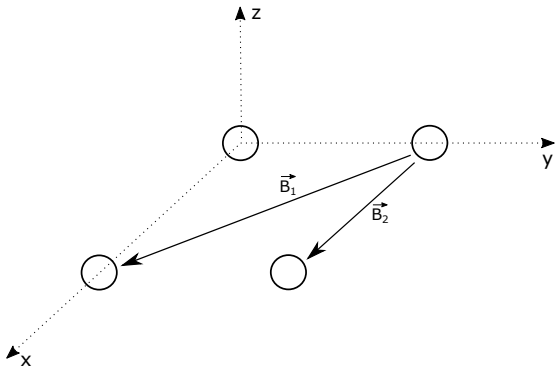

Figure 1.1: Regularly spaced 4-element planar interferometer. $\overrightarrow{B_i}$ denotes the baseline vector between two elements. Note not all possible baselines are shown.

array as seen with the Murchison Widefield Array (MWA) [16, 17]. A phased array consists of multiple antenna elements in which the output signals summed together to form a single larger element.

In this thesis, we will be developing the tools for characterizing the receiving element. As an example application, we will characterize the MWA's receiving elements.

1.3 The Murchison Widefield Array

The Murchison Widefield Array is a radio interferometry telescope that is the first operational low-frequency precursor telescope to the Square Kilometre Array Low-Frequency telescope (SKA-Low) [18] located at the Murchison Radio-astronomy Observatory (MRO) in the Shire of Murchison, Western Australia [16]. The telescope consists of 256 phased arrays [17] called 'tiles' as shown in Fig 1.2. The maximum spread of the tiles that make up the overall telescope is approximately 5.3 km. Fig. 1.3 shows the aerial view of the telescope.

Each tile contains 16 antenna elements, called MWA dipoles, placed in a 4×4 configuration spaced 1.1 m apart over a 5×5 m metallic ground mesh. Each antenna element houses a low-noise amplifier (LNA) in the central hub and the output signal travels through a phase matched coaxial cable to the analogue beamformer. The MWA's tile is equivalent to a receiving element of the interfer-

Figure 1.2: An MWA tile connected to a beamformer (white rectangular box). Each antenna element contains a low-noise amplifier (LNA) in the central hub (white cylindrical container). Photo credits: Curtin University and MWA collaboration.

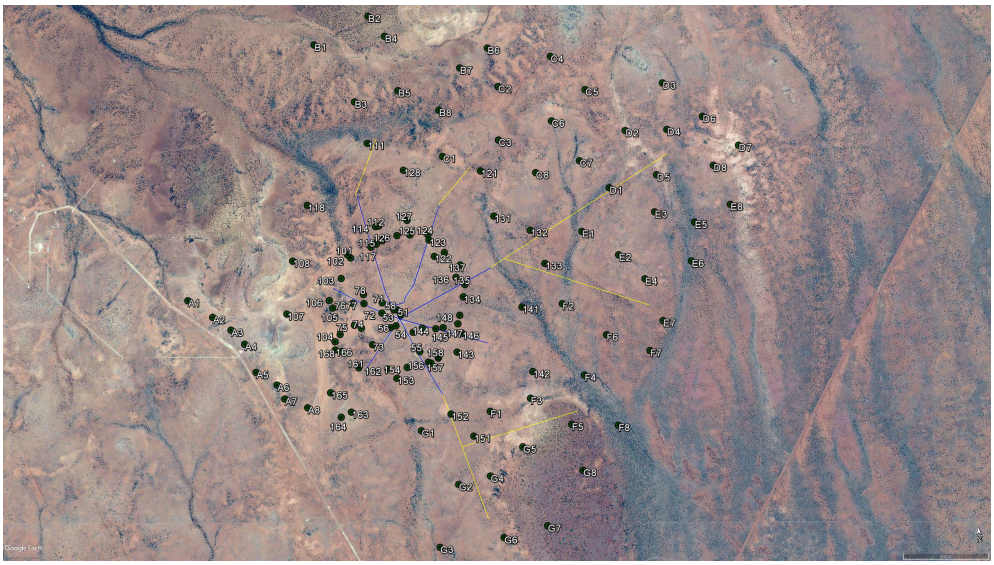

Figure 1.3: Aerial view of the MWA telescope with all 256 tiles. Photo credits: Curtin University and MWA collaboration.

ometer as discussed in the previous section.

The primary function of the analogue beamformer is to introduce an appropriate signal delay to each of the 16 input signals such that the plane wave originating from the source of interest is received in phase. This is achieved by the 5 switchable physical signal paths placed in series at the input. Due to the finite number of possible signal paths, the analogue beamformer is capable of pointing in 197 exact locations in the sky. The signals are then summed and transmitted to a node where it is digitized. This is how steering/pointing is done electronically and the advantage is that it can re-point the telescope to any direction in the sky in a matter of seconds.

1.4 Motivation

As mention in the previous section, phased arrays have the advantage of fast pointing speed over antenna dishes. However, the trade-off is that the array's far-field response (beam pattern) changes as a function of pointing angles. Furthermore, due to antenna elements being in close proximity to each other as seen with the MWA's tile, we also have mutual coupling which affects the final beam pattern and coupling of noise due to the low-noise amplifiers within the tile.

The knowledge of the beam pattern is important for calibration of the telescope and image correction of the final image [19, 20], while the knowledge of noise coupling is important for the calculation of sensitivity which is inversely proportional to the system equivalent flux density (SEFD) [21].

There are currently 21 partnering institutions that have access to the MWA telescope [22]. Hence, developing the necessary engineering tools to characterize the MWA's tile will have a wide reaching impact to the science community. Furthermore, the tools developed are not limited to the treatment of phased arrays but expandable characterize arbitrary receiving elements configuration such as the SKA-Low [18] that will be built in the future.

1.5 Aims

This research aims to develop the tools to calculate:

- Receiver noise temperature which includes the effects of mutual coupling in the array environment.
- Realised area.
- Radiation efficiency.
- System Equivalent Flux Density ($SEFD$).

1.6 Research Focus

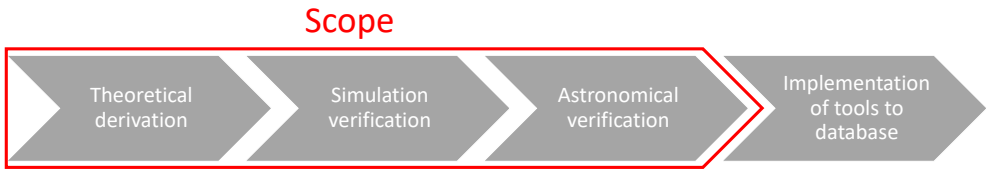

Figure 1.4: High level process flow of proposed research.

This thesis will focus on developing the theory for characterizing antenna arrays, verification of theory using simulation and verification via astronomical observation as shown in Figure 1.4. The implementation of tools to the database will be done as a follow-up to this thesis.

1.7 Thesis Outline

This thesis is organized as follows:

Chapter 2 provides the background on basic definitions used for characterizing antenna arrays and its limitation when characterizing a phased array with a summer network at the output.

Chapter 3 presents the proposed tools and theory of operation for characterizing antenna arrays.

Chapter 4 compares the theoretical derivation with the simulation results as a form of verification.

Chapter 5 presents the characterization of the MWA using the proposed tools and further verification using astronomical observations.

Chapter 6 concludes this thesis with summaries and closing remarks.

Chapter 2

Background

This chapter contains the formulation based on current literature to compute the sensitivity of a radio telescope and the constituent parameters required to complete the calculation. This chapter includes some sections from the author's previously published conference paper [23] found in Sect. 2.4 with some text and image modifications to preserve the flow and clarity of this thesis.

2.1 Sensitivity of a Radio Telescope

The sensitivity of a radio telescope is given by [24]

$$\frac{A_e}{T_{\text{sys}}} = \frac{A_e}{\eta_{\text{rad}} T_{\text{ext}} + (1 - \eta_{\text{rad}})\, T_{\text{a}} + T_{\text{rcv}}} \tag{2.1}$$

where A_{e} is the effective area for polarization matched sources, T_{sys} is the system temperature, η_{rad} is the radiation efficiency, T_{ext} is the antenna temperature due to sky, T_{a} is the ambient temperature and T_{rcv} is the receiver noise temperature.

As seen from (2.1), we require knowledge of various parameters of the telescope to compute the sensitivity. We will present methodologies found in current literature used to characterize a radio telescope in subsequent sub-sections as follows:

- Sect. 2.2 contains the current definition of effective area for phased arrays

and its limitation.

- Sect. 2.3 contains the definition of noise parameters needed for the calculation of receiver noise temperature.
- Sect. 2.4 contains current methods for calculating receiver noise temperature.
- Sect. 2.5 contains the current method for calculating radiation efficiency.

Before presenting the limitation of current definition of effective area for a phased array, let us first analyse the sensitivity of a single receiving element.

2.1.1 Sensitivity of Single Receiving Element

For a single element, the sensitivity definition presented in (2.1) is simple to compute and the reference plane at which the sensitivity is evaluated is irrelevant. However, when it comes to phased arrays the computation can be complex and the chosen reference plane matters. To show this formally, let us begin with a single element analysis. The magnitude of complex quantities such as voltage, currents and electric fields presented in the remainder of this thesis are *peak values*. The effective area of an antenna for a given direction is given by [25]

$$A_e = \frac{P_{\text{ave}}}{S_{\text{inc}}} \tag{2.2}$$

$$= \frac{|v_{oc}|^2}{8\Re\{Z_{\text{ant}}^*\}S_{\text{inc}}} \tag{2.3}$$

where P_{ave} is the available power at the antenna terminals, S_{inc} is the power flux density of the incident power that is polarization matched to the antenna, v_{oc} is the open-circuited voltage at the antenna terminals, Z_{ant} is the impedance of the antenna, $\Re\{\cdot\}$ represents the real operator and $\cdot^*$ is the complex conjugate operator.

For a single element, the effective area represents the maximum power that the antenna can deliver to a conjugately matched load for a given incident plane

wave. The open circuit voltage at the antenna terminals is related to the incident plane wave by [26]

$$v_{oc} = j\frac{4\pi}{\omega\mu_0 I_{tx}}\mathbf{E}_{tx}(\bar{r}) \cdot \mathbf{E}_{\text{inc}}(-\bar{r}) \tag{2.4}$$

$$= -\mathbf{l}_{eff}(\bar{r}) \cdot \mathbf{E}_{\text{inc}}(\bar{r}) \tag{2.5}$$

where ω is the angular frequency, μ_0 is the free space permeability, I_{tx} is the port current during transmit condition that produces the corresponding far-field pattern $\mathbf{E}_{tx}(\bar{r}) = [E_\theta, E_\phi]$, $\mathbf{E}_{\text{inc}}(-\bar{r}) = [e_\theta, e_\phi]^T$ is the incident plane wave, $\bar{r}$ is the position vector of a point in space with $-$ sign indicating radial direction towards origin, $\cdot^T$ represents the transpose operator and $\mathbf{l}_{eff}$ is the effective length which relates the incident plane wave to open circuit voltage at the antenna terminal.

Substituting (2.5) into (2.3) yields

$$A_e = \frac{|-\mathbf{l}_{eff}(\bar{r}) \cdot \mathbf{E}_{\text{inc}}(\bar{r})|^2}{8\Re\{Z^*_{\text{ant}}\}S_{\text{inc}}}. \tag{2.6}$$

We can make use of [27] to recast (2.6) for partially to fully polarised incident wave $\mathbf{E}_{\text{inc}}(-\bar{r})$ as follows

$$A_e = \left[\frac{1}{2} + p\left(\cos^2\psi - \frac{1}{2}\right)\right]\eta_0\frac{|l_{eff,\theta}|^2 + |l_{eff,\phi}|^2}{4\Re\{Z^*_{\text{ant}}\}} \tag{2.7}$$

$$p = \sqrt{1 - 4(\rho_{11}\rho_{22} - \rho_{12}\rho_{21})} \tag{2.8}$$

and

$$\rho_{11} = \frac{\langle|e_\theta|^2\rangle}{\langle|e_\theta|^2\rangle + \langle|e_\phi|^2\rangle} \tag{2.9}$$

$$\rho_{12} = \frac{\langle e^*_\theta e_\phi\rangle}{\langle|e_\theta|^2\rangle + \langle|e_\phi|^2\rangle} \tag{2.10}$$

$$\rho_{21} = \frac{\langle e_\theta e^*_\phi\rangle}{\langle|e_\theta|^2\rangle + \langle|e_\phi|^2\rangle} \tag{2.11}$$

$$\rho_{22} = \frac{\langle|e_\phi|^2\rangle}{\langle|e_\theta|^2\rangle + \langle|e_\phi|^2\rangle} \tag{2.12}$$

where θ and ϕ (X-Y plane) follows the ISO spherical coordinate convention [28], $0 \leq p \leq 1$ is the degree of polarization, $\cos^2\psi$ is the polarization mismatch factor and $\eta_0 = \sqrt{\frac{\mu_0}{\epsilon_0}}$ is the free space impedance.

For a fully polarised incident wave $\mathbf{E}_{\text{inc}}(-\bar{r}) = [e_\theta, 0]^T$ or $\mathbf{E}_{\text{inc}}(-\bar{r}) = [0, e_\phi]^T$, we obtain a degree of polarization $p = 1$. In addition, effective area is defined for polarization matched source to the antenna $\cos^2\psi = 1$ thus,

$$A_e = \frac{\eta_0}{4} \frac{|l_{eff,\theta}|^2 + |l_{eff,\phi}|^2}{\Re\{Z^*_{\text{ant}}\}}. \tag{2.13}$$

It is typical for a receiving antenna that a load is attached to the input terminals and this is typically the input impedance of the low-noise amplifier (Z_{LNA}). The element efficiency as defined in [29] will drop as it now contains mismatch losses and therefore will reduce the total received power. This is defined as the realised radiation efficiency in [25]. The realised aperture area is now given by

$$A_r = \frac{P_{\text{load}}}{S_{\text{inc}}} \tag{2.14}$$

where P_{load} is the power delivered to the load.

We can calculate the voltage drop across the load and delivered power using

$$v_{\text{load}} = \frac{Z_{\text{load}}}{Z_{\text{load}} + Z_{\text{ant}}} v_{oc} \tag{2.15}$$

$$P_{\text{load}} = \Re\left\{ \frac{|v_{\text{load}}|^2}{2Z^*_{\text{load}}} \right\}. \tag{2.16}$$

Therefore the realised area of the antenna for $p = 1$ and $\cos^2\psi = 1$ is given by

$$A_r = \left| \frac{Z_{\text{load}}}{Z_{\text{load}} + Z_{\text{ant}}} \right|^2 \eta_0 \frac{|l_{eff,\theta}|^2 + |l_{eff,\phi}|^2}{\Re\{Z^*_{\text{load}}\}}. \tag{2.17}$$

Comparing (2.13) to (2.17), we can see that

$$A_r = \tau A_e \tag{2.18}$$

$$\tau = 4\frac{\Re\{Z_{\text{load}}\}\Re\{Z_{\text{ant}}\}}{|Z_{\text{load}} + Z_{\text{ant}}|^2}. \tag{2.19}$$

The implication of (2.18) is that the normalized power pattern shape is identical to the normalized A_e and A_r. That is to say

$$\frac{|E_\theta|^2 + |E_\phi|^2}{\max\{|E_\theta|^2 + |E_\phi|^2\}} = \frac{A_e}{\max\{A_e\}} = \frac{A_r}{\max\{A_r\}}. \tag{2.20}$$

We now modify T_{sys} seen in (2.1) to include mismatches to align the reference plane with A_r. For a single element, the mismatch factor is given by

$$M_L = \frac{(1 - |\Gamma_{\text{ant}}|^2)(1 - |S_{\text{load}}|^2)}{|1 - \Gamma_{\text{ant}} S_{\text{load}}|^2} \tag{2.21}$$

$$= 4\frac{\Re\{Z_{\text{load}}\}\Re\{Z_{\text{ant}}\}}{|Z_{\text{load}} + Z_{\text{ant}}|^2} \tag{2.22}$$

where Γ_{ant} and S_{load} are the S-parameters (refer to Appendix C) of the antenna and load respectively.

Comparing (2.22) to (2.19), we observe that $M_L = \tau$. Hence, the chosen reference plane for sensitivity calculation of a single element is irrelevant as

$$\frac{\tau A_{\text{e}}}{M_L T_{\text{sys}}} = \frac{A_{\text{e}}}{T_{\text{sys}}}. \tag{2.23}$$

Meaning, we can evaluate sensitivity using available power at the input/output or delivered power to the input/output and still achieve the same result. Next, we will analyse the effective area of phased arrays.

2.2 Effective Area of Phased Arrays

The question of interest is whether (2.20) holds when the exact analysis is applied to a phased array. Firstly, let us consider the far-field pattern of the entire array for a given load impedance which can be calculated using embedded element patterns (EEPs) given by [30]

$$E_{\text{array}}(\theta,\phi) = \sum_{n=1}^{N} w_n V_{s,n} E_n(\theta,\phi) \tag{2.24}$$

where $E_{\text{array}}(\theta,\phi)$ is the electric far-field pattern of the array, w_n is the complex weight applied with amplitude scaled by the number of elements N such that $\sum_{n=1}^{N} |\mathbf{w}_n|^2 = 1$, $V_{s,n}$ is the generator voltage applied at the n^{th} element and $E_n(\theta,\phi)$ is the radiated electric far-field (EEP) of the n^{th} element excited by a generator voltage at unity with zero phase while all other generator voltages are zero and all elements are terminated with known impedances (loads).

Based on (2.24), if we know the embedded element pattern $E_n(\theta,\phi)$ of each antenna element in the array, we can obtain the electric far-field pattern of the array by summing all the individual element pattern. To steer the array's beam in a particular direction, we simply apply the appropriate complex weightings during the summation.

Using the exact assumption of a deterministic incident plane wave ($\mathbf{E}_{\text{inc}}(-\bar{r}) = [e_\theta, 0]^T$), we can still apply (2.3) to each individual embedded element but Z_{ant} is replaced with the embedded impedance Z'_{ant}. The total equivalent effective area of the phased array can be computed using a modified version of the pattern overlap integral method [31] as follows

$$A_e^{\text{array}}(\theta,\phi) = \frac{P_{av,tot}}{S_{\text{inc}}} = \mathbf{w}\mathbf{L}\mathbf{w}^\dagger \tag{2.25}$$

$$L_{mn} = \frac{\eta_0}{4} \frac{l_{eff,m}(\theta,\phi)}{\sqrt{\Re\{Z'^{*}_{\text{ant},m}\}}} \cdot \frac{l^\dagger_{eff,n}(\theta,\phi)}{\sqrt{\Re\{Z'^{*}_{\text{ant},n}\}}} \tag{2.26}$$

where $\mathbf{L}$ is the effective length overlap matrix, $\mathbf{w} = [w_1, w_2, \cdots w_n]$ is a row vector

containing the complex weighting and $\cdot^{\dagger}$ represents the Hermitian operator.

To reduce the complexity of evaluating $\mathbf{L}$, we can express the total effective area in a similar form seen in (2.24) as follows

$$A_e^{\text{array}}(\theta,\phi) = \frac{\eta_0}{4}\left|\sum_{n=1}^{N} w_n \frac{l_{eff,n}(\theta,\phi)}{\sqrt{\Re\{Z'^{*}_{\text{ant},n}\}}}\right|^2 \tag{2.27}$$

In general due to mutual coupling, we find that $Z'^{*}_{\text{ant},m} \neq Z'^{*}_{\text{ant},n}$ for $m \neq n$ which means it does not factor out of the summation in (2.27) therefore,

$$\frac{A_e^{\text{array}}}{\max\{A_e^{\text{array}}\}} \neq \frac{|E_{\text{array}}|^2}{\max\{|E_{\text{array}}|^2\}}. \tag{2.28}$$

Furthermore, the effective area can also be calculated using the following definition [24] as follows

$$A_e = \eta_{\text{rad}} \frac{\lambda^2}{2\eta_0 P_{rad}} |E_{\text{array}}(\theta,\phi)|^2 \tag{2.29}$$

where P_{rad} is the total radiated power of the array.

Effective area calculated using (2.29) also assumes fully deterministic ($p = 1$) plane wave that is polarization matched ($\cos^2\psi = 1$). From (2.28), it also implies that depending on which definition using (2.27) or (2.29) is used, we obtain a different A_e. Therefore, for a mutually coupled phased array with a summing network connected to the outputs of the low-noise amplifier network, it is not possible to define the effective area as it creates a contradiction between different definitions.

We will introduce a more appropriate definition of sensitivity for a phased array in Sect. 3.1. Before advancing to the calculation of receive noise temperature. We will introduce the concept of noise parameters and its relation to noise waves.

2.3 Noise Parameters

The noise temperature of a device under test (DUT) is a function of the attached source reflection coefficient and can be calculated provided the four noise parameters are known. The relationship between the noise parameters and noise temperature is of a DUT given by [32]

$$T_{\mathrm{DUT}}(\Gamma_s) = T_{\min} + 4T_0 N \frac{|\Gamma_s - \Gamma_{\mathrm{opt}}|^2}{(1-|\Gamma_s|^2)(1-|\Gamma_{\mathrm{opt}}|^2)} \tag{2.30}$$

where $T_0 = 290$ K is the reference temperature, Γ_s is the attached source impedance, Γ_{opt} is the optimum source impedance such that when $\Gamma_s = \Gamma_{\mathrm{opt}}$ then $T_{\mathrm{DUT}} = T_{\min}$, $T_{\min}$ is the minimum achievable noise temperature of the DUT and N is the Lange invariant noise ratio [33, 34].

We can covert the noise parameters into noise waves (per unit Hz) as follows [34, 35]

$$\langle |c_1|^2 \rangle = k\left(4T_0 N \frac{|1 - S_{11}\Gamma_{\mathrm{opt}}|^2}{1-|\Gamma_{\mathrm{opt}}|^2} - T_{\min}(1-|S_{11}|^2)\right) \tag{2.31}$$

$$\langle |c_2|^2 \rangle = k|S_{21}|^2\left(T_{\min} + 4T_0 N \frac{|\Gamma_{\mathrm{opt}}|^2}{1-|\Gamma_{\mathrm{opt}}|^2}\right) \tag{2.32}$$

$$\langle c_1 c_2^* \rangle = -4kT_0 N \frac{S_{21}^* \Gamma_{\mathrm{opt}}^*}{1-|\Gamma_{\mathrm{opt}}|^2} + \frac{S_{11}}{S_{21}}\langle |c_2|^2 \rangle \tag{2.33}$$

where S_{ij} are the S-parameters of the DUT, k is the Boltzmann constant and $\langle \cdot \rangle$ represents time-averaging.

In the next section, we will show how the reflected and coupled c_1 affects the receiver noise temperature of a phased array.

2.4 Receiver Noise Temperature

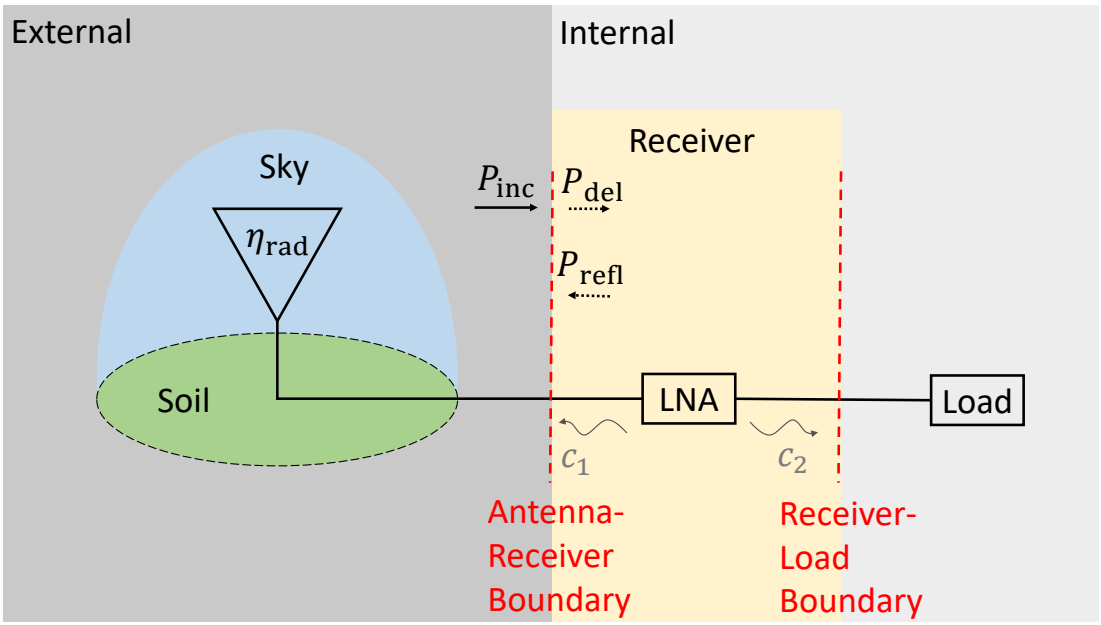

Figure 2.1: Overall system diagram of an antenna connected to an LNA. The system is made up of an external part which consists of an antenna, sky and soil while the internal part consists of the receiver and a load. The boundary indicates a region in which a mismatch of impedance could occur and hence causes incident power waves to that boundary be either partially or fully reflected. The notation P_{inc} indicates the incident power, P_{del} is the delivered power, which is the difference between the incident power and the reflected power P_{refl}. The LNA also emits noise waves at the input and output terminals labelled c_1 and c_2 respectively. The noise temperature is related to power spectral density by the relation $P \approx kT$ (refer to Appendix D) therefore, they can be used interchangeably. Noise temperatures calculated involving active devices do not correspond to a physical temperature.

Fig. 2.1 depicts different sources of noise that exist in the system. Firstly, we have external noise which consists of noise from the sky due to naturally radiating

cosmic sources, plus soil and thermal noise due to ohmic losses which form a net power flow that is incident onto the Antenna-Receiver Boundary represented by P_{inc}. Secondly, we have internal noise due to the receiver which produces noise waves indicated by c_1 and c_2 towards both boundaries [35] and noise waves emerging from the load (not shown in diagram). We can calculate receiver noise temperature T_{rcv} for a single element using [24]

$$T_{\text{rcv}} = \frac{P_{\text{del}}^{\text{rcv}}}{P_{\text{del}}^{\text{amb}}} T_0 \tag{2.34}$$

$$P_{\text{del}}^{\text{rcv}} = \langle |\chi c_1 + c_2|^2 \rangle \tag{2.35}$$

$$\chi = \frac{\Gamma S_{21}}{1 - S_{11}\Gamma} \tag{2.36}$$

where $P_{\text{del}}^{\text{rcv}}$ is the delivered receiver noise power at the output, $P_{\text{del}}^{\text{amb}}$ is the delivered ambient temperature noise power at the output given that the antenna is immersed in a isotropic environment at a temperature of T_0, Γ is the reflection coefficient of the antenna and S_{mn} are the S-parameters of the LNA.

We can see in (2.35) that for a single element, the reflected c_1 wave weighted by χ affects the resulting T_{rcv}. However, this reflected wave is simple to calculate and therefore does not pose any difficulty, but in a multi-element array such as the MWA tile, the computation is less obvious due to mutual coupling effects. In addition, c_1 waves also couples to adjacent elements which needs to be accounted for. With the aid of Fig. 2.2, we can visualize the complication introduced by coupling effects in a two-element array.

The $P_{\text{del}}^{\text{rcv}}$ seen in (2.34) under this condition is given by

$$P_{\text{del}}^{\text{rcv}} = \langle \mathbf{b}\mathbf{b}^{\dagger} \rangle = \langle \left| w_1 c_{1,net} + w_2 c'_{1,net} + w_1 c_2 + w_2 c'_2 \right|^2 \rangle \tag{2.37}$$

where $c_{1,net}$ and $c'_{1,net}$ are the net total noise wave that is incident into the summer after accounting for the self-reflected and coupled wave.

The calculation of $c_{n,net}$ for n-port network is a non-trivial operation when

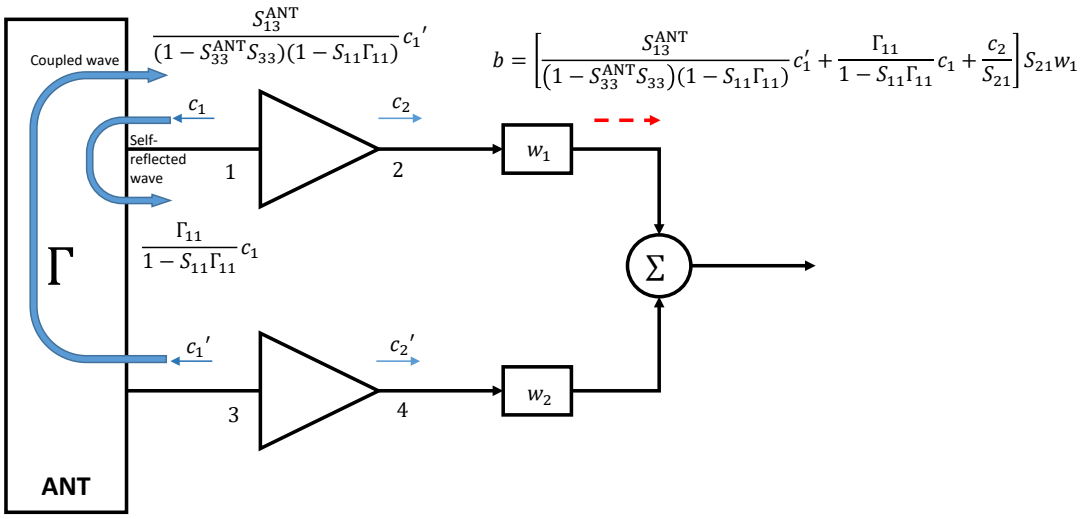

Figure 2.2: Coupling path of internal noise sources for a two-element array. The input ports are odd numbered and the output ports are even numbered. The output referred receiver noise temperature $\langle \mathbf{b}\mathbf{b}^{\dagger} \rangle$ consists of self-reflected and coupled wave from neighbouring element and noise wave (c_2) emanating from the output of the receiver. The w_n represents the complex weighting applied to the beamformer to point the telescope at the desired location in the sky. While not shown, similar coupling paths occur at the lower branch.

using (2.37), furthermore we do not have direct information of c_n of the LNA but we do know the noise correlation matrix $\langle \mathbf{c}\mathbf{c}^{\dagger} \rangle$ through the relation seen in (2.31)-(2.33). It will be shown in Sect. 3.2 that we can make use of the power wave based framework presented in [36] to tackle this calculation. Before moving on, we will present the two most recent methods for calculating the T_{rcv} of phased arrays in Sect. 2.4.1 and 2.4.2.

2.4.1 Method 1

The analysis of total coupled noise waves to the output of the array follows [37]. The total noise power at the output of the summer due to internal sources alone is given by

$$\begin{aligned} P_{\text{int}}^{\text{out}} &= |S_{21}|^2\langle|c_1|^2\rangle\mathbf{w}(\mathbf{I}-\mathbf{S}^{\text{ant}}S_{11})^{-1} \\ &\quad \mathbf{S}^{\text{ant}}\left(\mathbf{S}^{\text{ant}}\right)^{\dagger}(\mathbf{I}-\mathbf{S}^{\text{ant}}S_{11})^{-\dagger}\mathbf{w}^{\dagger} \\ &\quad + 2\Re\{S_{21}\langle c_1c_2^*\rangle\mathbf{w}(\mathbf{I}-\mathbf{S}^{\text{ant}}S_{11})^{-1}\mathbf{S}^{\text{ant}}\mathbf{w}^{\dagger}\} \\ &\quad + \langle|c_2|^2\rangle\mathbf{w}\mathbf{w}^{\dagger} \end{aligned} \tag{2.38}$$

where $\mathbf{w} = [w_1 \dots w_n]$ is the complex weighting vector, S_{mn} are the S-parameters of the LNA, $\mathbf{S}^{ant}$ is the S-parameter matrix of the antenna array, $\mathbf{I}$ is an identity matrix, $\langle|c_1|^2\rangle$, $\langle c_1c_2^*\rangle$ and $\langle|c_2|^2\rangle$ are the noise correlation terms of the LNA.

It can be shown that for a two-element array, (2.38) produces the exact output power expression seen in Fig. 2.2. The available gain of an array is given by [37]

$$G_A = \sum_{m=1}^{M}\frac{1-|\zeta\Gamma_{s,m}|^2}{|1-\Gamma_{s,m}S_{11}|^2}|S_{21}w_m|^2|1+\Gamma_{s,m}S_{11}\kappa_m|^2 \tag{2.39}$$

$$\zeta = \frac{1+\kappa_m}{1+\Gamma_{s,m}S_{11}\kappa_m} \tag{2.40}$$

$$\Gamma_{s,m} = \text{row}_m\{(\mathbf{I}-\mathbf{S}^{\text{ant}}\mathbf{S})^{-1}\mathbf{S}_n^{\text{ant}}\} \tag{2.41}$$

where $\mathbf{S}_n^{\text{ant}} = [S_{1,n}^{\text{ant}} \dots S_{M,n}^{\text{ant}}]^T$ is the S-parameter of the array, $\mathbf{S} = S_{11}(\mathbf{I}-\mathbf{J}_{n,n})$ is the S-parameter of the LNA, $\mathbf{J_{n,n}}$ represents a single-entry matrix at row n and column n, $\Gamma_{s,m}$ is the embedded reflection coefficient of the antenna element and κ_m is a ratio of the total coupled noise wave at the output of adjacent branches with respect its self-reflected $\langle c_1\rangle$ wave at the output of the m^{th} branch.

2.4.2 Method 2

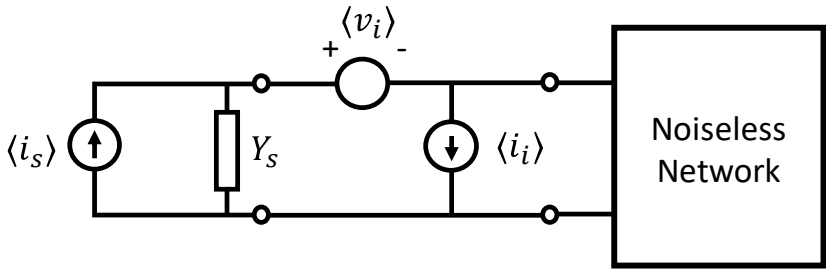

Figure 2.3: Circuit representation of input referred voltage and current noise source. The i_s and Y_s are parts of the Norton equivalent circuit of the source attached to the network.

T_{rcv} can be also determined by using equivalent voltage and current noise sources using the expression [38]

$$T_{\text{rcv}} = \frac{1}{4k} \frac{\mathbf{wQRQ}^{\dagger}\mathbf{w}^{\dagger}}{\mathbf{wQ}\Re\{\mathbf{Z}_A\}\mathbf{Q}^{\dagger}\mathbf{w}^{\dagger}} \tag{2.42}$$

$$\mathbf{Q} = Z_{11}\left(Z_{11}\mathbf{I} - \mathbf{Z}_A\right)^{-1} \tag{2.43}$$

$$\mathbf{R} = \mathbf{V}_{n,R}^2 + \mathbf{Z}_A\mathbf{Y}_c\mathbf{V}_{n,R}^2 + \mathbf{V}_{n,R}^2\mathbf{Y}_c^{\dagger}\mathbf{Z}_A^{\dagger} + \mathbf{Z}_A\mathbf{I}_{n,R}^2\mathbf{Z}_A^{\dagger} \tag{2.44}$$

where Z_{11} is the input impedance of the LNA, $\mathbf{Z}_A$ is the impedance matrix of the mutually coupled elements, $\mathbf{V}_{n,R}^2$, $\mathbf{I}_{n,R}^2$ and $\mathbf{Y}_c$ are diagonal matrices of squared noise voltage densities, squared noise current densities and correlation admittance of the LNA.

The noise parameters of the LNA can be converted into an input referred noise voltage and current sources as shown in Fig. 2.3 and the relationship between the two can be found in [39]. It will be shown in Sect. 4.2, that both methods produce identical results. Next we will introduce a commonly used method for calculating radiation efficiency.

2.5 Radiation Efficiency Calculation

The radiation efficiency of any antenna structure is defined by [24, 40]

$$\eta_{\text{rad}} = \frac{P_{\text{rad}}}{P_{\text{inj}}} \tag{2.45}$$

$$P_{\text{rad}} = \frac{1}{2\eta_0} \int_0^{2\pi} \int_0^{\pi} \left(|E_\theta|^2 + |E_\phi|^2 \right) \sin\theta d\theta d\phi \tag{2.46}$$

$$P_{\text{inj}} = \frac{1}{2} \Re\{V_{\text{ant}} I_{tx}^*\} \tag{2.47}$$

where P_{rad} is the total radiated power, P_{inj} is the total injected (delivered) power into the antenna, E_θ and E_ϕ is the θ and ϕ component of the far-field pattern of the array as a function of θ and ϕ, V_{ant} and I_{tx} are the voltage drop across the antenna and port current during transmit mode respectively.

As noted in [40], the accuracy of this computation for high efficiency arrays is limited by the numerical sampling and integration of the far-field pattern used to compute P_{rad}. Furthermore, additional data such as port currents and voltage drop across the antenna terminals are required to be saved for the computation of P_{inj}. While the numerical integration is unavoidable, we aim to reduce the amount of additional data required to be saved and reuse pre-existing data obtained during the characterization of the phased array such as embedded element pattern and S-parameter simulation. This provides the additional motivation for using the proposed modified pattern overlap integral (POI) method that will be presented in Sect. 3.3.

2.6 Chapter Summary

In this chapter, we presented the definition of sensitivity which is one of the figure of merit used during the characterization of radio telescopes. Using standard definitions found in current literature, we introduced the various formulation required to calculate sensitivity such as effective area, receiver noise temperature and radiation efficiency. We showed the limitation of standard definition of effective area when applied to phased arrays through simple derivations starting from a single receiving element. For the calculation of receiver noise temperature, we presented two most current formulation found in literature. Lastly, we provided the typical definition and method used for calculating radiation efficiency.

In the next chapter, we will introduce the proposed replacement of effective area with realised area and a modified definition for calculating sensitivity that is physically motivated. We will also introduce our proposed method for calculating receiver noise temperature and radiation efficiency.

Chapter 3

Proposed Methodology

This chapter contains the proposed tools for characterizing the performance of antenna arrays which include phased arrays. Based on the limitation of standard definition of effective area shown in the previous chapter, we proposed to define realised area which can be used to compute sensitivity later on. In addition, we will introduce a power wave based framework for the computation of receiver noise temperature. Following that, we will introduce a method of calculating radiation efficiency using the proposed definition of realised area.

This chapter includes some sections from the author's published conference paper [41] on the topic radiation efficiency calculation found in Sect. 3.1 and 3.3 with major text modification to preserve the flow and clarity of this thesis. In particular, Sect. 3.3 has been extended to include more detailed explanations and analysis of the proposed method which was omitted in [41].

Sect. 3.2, contains the major contribution of this thesis which has been submitted to IEEE Transactions on Antennas and Propagation for consideration [42]. A major revision was required and a copy of the revised journal article can be found in Appendix. A.

3.1 Realised Area of Phased Arrays

As shown in Sect. 2.1.1, the definition of realised area using (2.14) is proportional to the effective area (2.29) via the relation of τ (2.18). This relation will remain true regardless of the presence of mutual coupling under the condition that identical LNAs are used for the analysis. The general formula for calculating realised area of a single element based on derivations found in Sect. 2.1.1 is given by

$$A_r = \left[\frac{1}{2} + p\left(\cos^2\psi - \frac{1}{2}\right)\right] \left|\frac{Z_{\text{load}}}{Z_{\text{load}} + Z_{\text{ant}}}\right|^2 \Re\left\{\frac{\eta_0}{Z_{\text{load}}^*}\right\} \left(|l_{eff,\theta}|^2 + |l_{eff,\phi}|^2\right). \tag{3.1}$$

We can further simplify (3.1) by substituting $l_{eff}(\bar{r})$ with (2.4) and expanding the terms to yield

$$A_r = \left[\frac{1}{2} + p\left(\cos^2\psi - \frac{1}{2}\right)\right] 4\frac{\lambda^2}{\eta_0 V_{tx}^2} \Re\{Z_{\text{load}}\} \left[|E_{tx,\theta}(\bar{r})|^2 + |E_{tx,\phi}(\bar{r})|^2\right] \tag{3.2}$$

as

$$I_{tx} = \frac{V_{tx}}{Z_{\text{load}} + Z_{\text{ant}}}. \tag{3.3}$$

Using the results of (3.2), we can calculate the realised area of the array using the modified version of the pattern overlap integral method [31] as follows

$$A_r^{\text{array}} = \mathbf{w}\mathbf{A}\mathbf{w}^\dagger \tag{3.4}$$

$$= \left[\frac{1}{2} + p\left(\cos^2\psi - \frac{1}{2}\right)\right] 4\frac{\lambda^2}{\eta_0} \Re\{Z_{\text{load}}\} \left[\left|\sum_{n=1}^{N} w_n E_{n,\theta}\right|^2 + \left|\sum_{n=1}^{N} w_n E_{n,\phi}\right|^2\right] \tag{3.5}$$

and

$$A_{mn} = \left[\frac{1}{2} + p\left(\cos^2\psi - \frac{1}{2}\right)\right] 4\frac{\lambda^2}{\eta_0} \Re\{Z_{\text{load}}\} \left[E_{m,\theta} E_{n,\theta}^* + E_{m,\phi} E_{n,\phi}^*\right] \tag{3.6}$$

where $V_{tx} = 1 \angle 0^\circ$ is the peak voltage applied during the embedded element pattern simulation which produces the corresponding $E_{tx,m}(\bar{r}) = E_m$.

As we have assumed identical input impedances (Z_{load}), we were able to factor that out of the summation in (3.5). Therefore it obvious that

$$\frac{A_r^{\text{array}}}{\max\{A_r^{\text{array}}\}} = \frac{|E_{\text{array}}|^2}{\max\{|E_{\text{array}}|^2\}}. \tag{3.7}$$

We can restate (2.18) and apply this definition to the array as follows

$$A_r^{\text{array}} = \tau \left[\frac{1}{2} + p\left(\cos^2\psi - \frac{1}{2}\right)\right] \eta_{\text{rad}} \frac{\lambda^2}{2\eta_0 P_{rad}} \left[|E_{\text{array},\theta}(\theta,\phi)|^2 + |E_{\text{array},\phi}(\theta,\phi)|^2\right] \tag{3.8}$$

where τ is the total mismatch (derived in Sect. 3.2) of the array given by [41]

$$\tau = \frac{\mathbf{w}\left[\mathbf{P}^{\text{inc}} - \mathbf{P}^{\text{refl}}\right]_{mn=1,3,\cdots,2N-1}\mathbf{w}^\dagger}{kT_0} \tag{3.9}$$

$$\mathbf{P}^{\text{refl}} = \mathbf{M}\mathbf{S}_{\text{LNA}}\langle\mathbf{e}\mathbf{e}^\dagger\rangle(\mathbf{S}_{\text{LNA}})^\dagger\mathbf{M}^\dagger \tag{3.10}$$

$$\mathbf{P}^{\text{inc}} = \mathbf{M}'\langle\mathbf{e}\mathbf{e}^\dagger\rangle\mathbf{M}'^\dagger \tag{3.11}$$

$$\mathbf{M} = [\mathbf{I} - \mathbf{S}_{\text{LNA}}\mathbf{S}_{\text{ant}}]^{-1} \tag{3.12}$$

$$\mathbf{M}' = [\mathbf{I} - \mathbf{S}_{\text{ant}}\mathbf{S}_{\text{LNA}}]^{-1} \tag{3.13}$$

$$\langle\mathbf{e}\mathbf{e}^\dagger\rangle = kT_0\left(\mathbf{I} - \mathbf{S}_{\text{ant}}\mathbf{S}_{\text{ant}}^\dagger\right) \tag{3.14}$$

where $\mathbf{P}^{\text{inc}}$ and $\mathbf{P}^{\text{refl}}$ are the incident and reflected power to(from) the LNA respectively, $[\mathbf{A}]_{mn=1,3,\ldots,2N-1}$ represents a submatrix containing odd numbered rows and columns of matrix $\mathbf{A}$, $\mathbf{I}$ is an identity matrix, $\mathbf{S}_{\text{LNA}}$ and $\mathbf{S}_{\text{ant}}$ are the S-parameter of the LNA and array respectively and $\mathbf{M}$ and $\mathbf{M}'$ accounts for the mismatches in impedance between the LNA and array respectively.

It should be pointed out here that A_r^{array}/τ for $p = 1$ and $\cos^2\psi = 1$ does not yield the array effective's area as seen in with the single element analysis in Sect. 2.1.1. This is because the array beam pattern is dependant on the load and even

though the mismatch has been accounted for via the introduction of τ, it does not represent the maximum area achievable by the array.

For example, the EEP will change depending on the load attached in a mutually coupled environment and therefore will change the resulting array beam pattern calculated using (2.24). Therefore, the 'effective area' obtained using A_r^{array}/τ changes with changing loading conditions. This is a violation of the definition of effective area which is invariant to changing loading condition. Hence, the proposed realised area is more physically motivated because it represents the power delivered to the array for given attached identical loads (LNA input impedance) in response to an incident plane wave.

Let us now consider unpolarised sources typically encountered by astronomers whereby

$$\langle \mathbf{E}_{\text{inc}}(-\bar{r}) \cdot \mathbf{E}_{\text{inc}}(-\bar{r})^{\dagger} \rangle = \begin{bmatrix} \langle |e_\theta|^2 \rangle & 0 \\ 0 & \langle |e_\phi|^2 \rangle \end{bmatrix} \tag{3.15}$$

where $\langle e_\theta e_\phi^* \rangle = \langle e_\theta^* e_\phi \rangle = 0$ and $\langle |e_\theta|^2 \rangle = \langle |e_\phi|^2 \rangle$.

The degree of polarization of (3.15) calculated using (2.8) yields $p = 0$. Therefore, the realised area of a phased array under this condition using (2.17) becomes

$$A_r = 2\frac{\lambda^2}{\eta_0} \Re\{Z_{\text{load}}\} \left[\left| \sum_{n=1}^{N} w_n E_{n,\theta} \right|^2 + \left| \sum_{n=1}^{N} w_n E_{n,\phi} \right|^2 \right]. \tag{3.16}$$

It is worth noting that the polarization mismatch factor $\cos^2 \psi$ is irrelevant at this point as noted in [27]. We will re-iterate that (3.16) is valid in the case of identical loading attached to the receiving elements. In the case of unequal LNA input impedances, we are still left with

$$\frac{A_r^{\text{array}}}{\max\{A_r^{\text{array}}\}} \neq \frac{|E_{\text{array}}|^2}{\max\{|E_{\text{array}}|^2\}} \tag{3.17}$$

as the LNA impedances will not factor out of the summation in (3.5).

The inequality of (3.17) raises a question as to which normalized pattern should be used to evaluate T_{ext} in (2.1). From [43, Ch. 17, pg. 779], the antenna temperature can be calculated using

$$T_{\text{ext}} = \frac{1}{\Omega_s} \int_{\phi=0}^{2\pi} \int_{\theta=0}^{\pi} P_n(\theta, \phi) T(\theta, \phi) \sin\theta \; d\theta d\phi \tag{3.18}$$

$$\Omega_s = \int_{\phi=0}^{2\pi} \int_{\theta=0}^{\pi} P_n(\theta, \phi) \sin\theta \; d\theta d\phi \tag{3.19}$$

where P_n is the normalized power pattern of the array, T is the temperature distribution surrounding the array (sky temperature distribution) and Ω_s is the solid beam angle.

Equation (3.18) is typically used by astronomers when evaluating T_{ext} while η_{rad} is obtained separately or assumed to be unity. The normalized power pattern as calculated by astronomers makes use of

$$P_n(\theta, \phi) = \frac{|E_{\text{array}}|^2}{\max\{|E_{\text{array}}|^2\}}. \tag{3.20}$$

As discussed previously, depending on the definition used and loading conditions we can run into contradictions and it should be noted that the simpler form in (3.8) is no longer valid. For unpolarised sources, we can resolve this by showing that (refer to Appendix E)

$$\tau \eta_{\text{rad}} T_{\text{ext}} = \frac{2}{\lambda^2} \int_{\phi=0}^{2\pi} \int_{\theta=0}^{\pi} A_r^{\text{array}}(\theta, \phi) T(\theta, \phi) \sin\theta \; d\theta d\phi \tag{3.21}$$

and

$$A_r^{\text{array}} = 2\frac{\lambda^2}{\eta_0} \left[\left| \sum_{n=1}^{N} w_n \sqrt{\Re\{Z_{n,\text{load}}\}} E_{n,\theta} \right|^2 + \left| \sum_{n=1}^{N} w_n \sqrt{\Re\{Z_{n,\text{load}}\}} E_{n,\phi} \right|^2 \right] \tag{3.22}$$

where $Z_{n,\text{load}}$ is the load impedance attached to the n^{th} port.

From (3.21), it becomes apparent that the quantity A_r^{array} is the fundamental quantity that should be used. Therefore, the correct normalized power pattern

that should be used in the case of unequal LNA impedances is

$$P_n(\theta, \phi) = \frac{A_r^{\text{array}}}{\max\{A_r^{\text{array}}\}}. \tag{3.23}$$

Next, we will introduce the proposed method for calculating receiver noise temperature using a power wave based framework (PWF).

3.2 Receiver Noise Calculation Using A Power Wave Based Framework

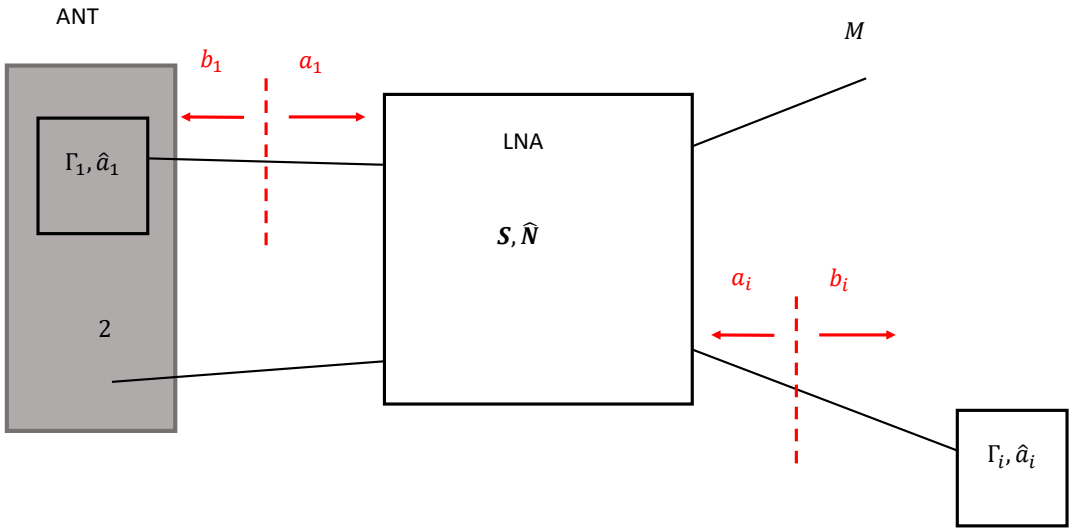

Figure 3.1: Example of a multiport connection between an array of antennas represented by 'ANT' and loads to the LNA network with known S-parameter $\mathbf{S}$ and noise correlation matrix $\hat{\mathbf{N}}$. We have omitted the summing network at the output of the network (i^{th} to the M^{th} port) to keep the analysis general. However, we will show that a summing network can be easily added later on. The convention of incident a_n and reflected waves b_n represented by the red arrows are also shown are referenced to the LNA network.

For the computation of receiver noise, we will make use of the power wave based framework introduced in [36] with modification accounting for the summing network at the output of the phase array. We begin by defining the array architecture and convention that will be used as shown in Fig. 3.1.

Following the definition of S-parameters (refer to (C.7) in Appendix. C), we define the following quantities

$$\mathbf{b} = \mathbf{S}_{\text{LNA}}\mathbf{a} + \mathbf{n} \tag{3.24}$$

$$\mathbf{a} = \mathbf{S}_{\text{load}}\mathbf{b} + \mathbf{e} \tag{3.25}$$

where $\mathbf{b}$ is a vector containing the outgoing waves from the input and output ports of multiport amplifier network, $\mathbf{n} = [c_1, c_2, \cdots c_n]^T$ is a column vector containing the noise waves of the LNA, $\mathbf{a}$ is the vector containing the incoming waves to the input and output ports of the multiport amplifier network, $\mathbf{e} = [e_1, e_2, \cdots e_n]^T$ is a column vector containing the noise waves of the attached loads, $\mathbf{S}_{\text{LNA}}$ and $\mathbf{S}_{\text{load}}$ are the S-parameters of the network and loads (includes the antenna elements) respectively.

We can simultaneously solve for the outgoing wave by substituting (3.25) into (3.24) and solving for $\mathbf{b}$ to obtain the following

$$\mathbf{b} = \left[\mathbf{I} - \mathbf{S}_{\text{LNA}}\mathbf{S}_{\text{load}}\right]^{-1}\left(\mathbf{S}_{\text{LNA}}\mathbf{e} + \mathbf{n}\right) \tag{3.26}$$

$$\mathbf{b} = \mathbf{M}\left(\mathbf{S}_{\text{LNA}}\mathbf{e} + \mathbf{n}\right). \tag{3.27}$$

The outgoing power from the LNA network is then given by

$$\mathbf{A}_{\text{out}} = \langle \mathbf{b}\mathbf{b}^{\dagger} \rangle \tag{3.28}$$

$$= \mathbf{M}\langle \hat{\mathbf{N}} \rangle \mathbf{M}^{\dagger} + \mathbf{M}\mathbf{S}_{\text{LNA}}\langle \hat{\mathbf{E}} \rangle \mathbf{S}_{\text{LNA}}^{\dagger}\mathbf{M}^{\dagger} \tag{3.29}$$

where $\langle \mathbf{n}\mathbf{n}^{\dagger} \rangle = \langle \hat{\mathbf{N}} \rangle$ and $\langle \mathbf{e}\mathbf{e}^{\dagger} \rangle = \langle \hat{\mathbf{E}} \rangle$ are the noise correlation matrix of the LNA network and loads (includes noise correlation matrix of the antenna elements)

respectively and $\langle \mathbf{n}\mathbf{e}^{\dagger} \rangle = \langle \mathbf{n}^{\dagger}\mathbf{e} \rangle = 0$.

We can repeat this analysis to solve for the incoming wave. By substituting (3.24) into (3.25) and solving for $\mathbf{a}$, we obtain

$$\mathbf{a} = \left[\mathbf{I} - \mathbf{S}_{\text{load}}\mathbf{S}_{\text{LNA}}\right]^{-1} \left(\mathbf{S}_{\text{load}}\mathbf{n} + \mathbf{e}\right) \tag{3.30}$$

$$\mathbf{a} = \mathbf{M}' \left(\mathbf{S}_{\text{load}}\mathbf{n} + \mathbf{e}\right). \tag{3.31}$$

The incoming power to the LNA network is then given by

$$\mathbf{A}_{\text{in}} = \langle \mathbf{a}\mathbf{a}^{\dagger} \rangle \tag{3.32}$$

$$= \mathbf{M}' \langle \hat{\mathbf{E}} \rangle \mathbf{M}'^{\dagger} + \mathbf{M}' \mathbf{S}_{\text{load}} \langle \hat{\mathbf{N}} \rangle \mathbf{S}_{\text{load}}^{\dagger} \mathbf{M}'^{\dagger}. \tag{3.33}$$

With the aid of Fig. 3.2, we can draw out the physical interpretation of (3.29) and (3.33). We see a superposition of noise due to the LNA network (internal noise) represented by $\langle \hat{\mathbf{N}} \rangle$ and noise due to the antenna elements (external noise) represented by $\langle \hat{\mathbf{E}} \rangle$ in both equations. Equation (3.29) computes the total outgoing power due to all noise sources present in the system, while (3.33) computes the total incoming power (reflected power from the loads). The total power delivered to the loads of arbitrary impedances at the input and output of the LNA network can be calculated by taking the diagonal of

$$\mathbf{P}_{\text{del}}^{\text{loads}} = \left[\mathbf{A}_{\text{out}} - \mathbf{A}_{\text{in}}\right]. \tag{3.34}$$

Whereas, the non-diagonal entries contains the correlated power between attached loads.

For example, if an ideal noiseless power spectrum analyser with an input impedance of Z_0[1] is placed at port any output ports m prior to the summing

[1]Same impedance as the reference impedance used for the evaluation of S-parameters.

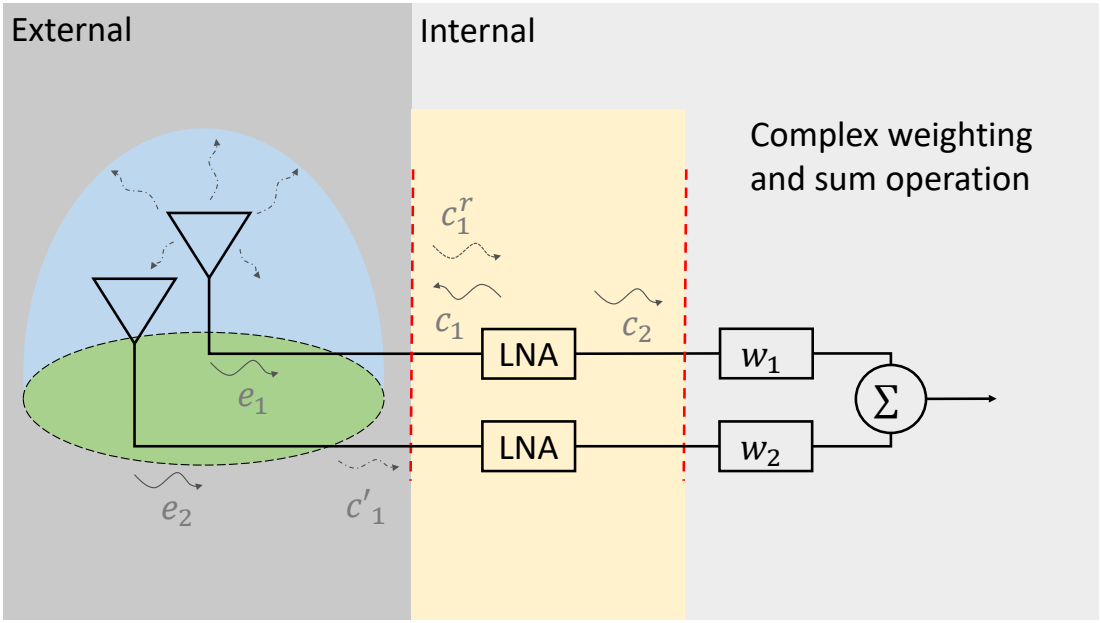

Figure 3.2: Coupling path of internal noise sources alone for a two-element array. The load as seen in Fig. 2.1 is now replaced with a complex weight and sum operator; however, the assumption of matched condition still remains. The output referred receiver noise temperature consists of reflected wave c_1^r, coupled wave to neighbouring element c_1' and noise wave c_2 emanating from the output of the receiver. While not shown, similar coupling paths occur at the lower branch. The outgoing noise wave from the antennas due to assumption of isotropic environment are represented by e_1 and e_2.

network, then the measured power will be as calculated by

$$P_{\text{meas}} = [\mathbf{A}_{\text{out}}]_{mm} \tag{3.35}$$

where $[\mathbf{A}]_{mm}$ represents an entry at row m column m of matrix $\mathbf{A}$ as

$$[\mathbf{A}_{\text{in}}]_{mm} = 0. \tag{3.36}$$

If an ideal power summer was placed between output port m and port n then, the measured output power from the summer is given by

$$P_{\text{meas}} = \frac{1}{2}\big([\mathbf{A}_{\text{out}}]_{mm} + 2\Re\{[\mathbf{A}_{\text{out}}]_{mn}\} + [\mathbf{A}_{\text{out}}]_{nn} \big). \tag{3.37}$$

With knowledge of (3.29) and (3.33), we can easily compute various quantities using superposition theory such as

1. available gain, transducer gain and power gain of the LNA network,

2. embedded and active impedances of the antenna elements,

3. delivered power to the loads, inputs and outputs of the LNA network.

As an example, we can calculate the total impedance mismatch τ by calculating the ratio between the delivered power to the input and the available power due to external noise. If we set $\langle\hat{\mathbf{N}}\rangle = 0$ then the total delivered power to the input of the LNA network due to $\langle\hat{\mathbf{E}}\rangle$ alone is given by

$$P_{del} = \mathbf{w}\left[\mathbf{A}_{\text{in}} - \mathbf{A}_{\text{out}}\right]_{mn=1,3,\cdots,2N-1}\mathbf{w}^{\dagger} \tag{3.38}$$

$$\left[\mathbf{A}_{\text{in}} - \mathbf{A}_{\text{out}}\right] = \mathbf{M}'\langle\hat{\mathbf{E}}\rangle\mathbf{M}'^{\dagger} - \mathbf{M}\mathbf{S}_{\text{LNA}}\langle\hat{\mathbf{E}}\rangle\mathbf{S}_{\text{LNA}}^{\dagger}\mathbf{M}^{\dagger} \tag{3.39}$$

and

$$\tau = \frac{\mathbf{w}\left[\mathbf{A}_{\text{in}} - \mathbf{A}_{\text{out}}\right]_{mn=1,3,\cdots,2N-1}\mathbf{w}^{\dagger}}{kT_0} \tag{3.40}$$

$$= \frac{\mathbf{w}\left[\mathbf{M}'\langle\hat{\mathbf{E}}\rangle\mathbf{M}'^{\dagger} - \mathbf{M}\mathbf{S}_{\text{LNA}}\langle\hat{\mathbf{E}}\rangle\mathbf{S}_{\text{LNA}}^{\dagger}\mathbf{M}^{\dagger}\right]_{mn=1,3,\cdots,2N-1}\mathbf{w}^{\dagger}}{kT_0}. \tag{3.41}$$

Before proceeding further with the remaining calculations, we must first ensure that $\mathbf{S}_{\text{LNA}}$, $\langle\hat{\mathbf{N}}\rangle$ and $\mathbf{S}_{\text{load}}$ have a consistent port numbering convention. Based on the port numbering convention shown in Fig. 3.3, if we assume that

1. the multiport amplifier is constructed from identical isolated 2-port element LNAs[2],

2. odd numbered ports are inputs and even number ports are output of the multiport amplifier network,

[2]Non-identical LNAs can also be used by modifying the entries in (3.42) and (3.43) to include the measured or simulated parameters of the non-identical LNA multiport network.

3. a reflectionless load (reference impedance matched Z_0) is attached to the outputs of the LNAs then,

$$\mathbf{S}_{\text{LNA}} = \begin{bmatrix} S_{11} & S_{12} & 0 & 0 & \dots \\ S_{21} & S_{22} & 0 & 0 & \dots \\ 0 & 0 & S_{11} & S_{12} & \dots \\ 0 & 0 & S_{21} & S_{22} & \dots \\ \vdots & \vdots & \vdots & \vdots & \ddots \\ 0 & 0 & 0 & 0 & \dots \\ 0 & 0 & 0 & 0 & \dots \end{bmatrix} \tag{3.42}$$

$$\hat{\mathbf{N}} = \begin{bmatrix} \langle |c_1|^2 \rangle & \langle c_1 c_2^* \rangle & 0 & 0 & \dots \\ \langle c_1^* c_2 \rangle & \langle |c_2|^2 \rangle & 0 & 0 & \dots \\ 0 & 0 & \langle |c_1|^2 \rangle & \langle c_1 c_2^* \rangle & \dots \\ 0 & 0 & \langle c_1^* c_2 \rangle & \langle |c_2|^2 \rangle & \dots \\ \vdots & \vdots & \vdots & \vdots & \ddots \\ 0 & 0 & 0 & 0 & \dots \\ 0 & 0 & 0 & 0 & \dots \end{bmatrix} \tag{3.43}$$

$$\mathbf{S}^{\text{load}} = \begin{bmatrix} S_{11}^{\text{ant}} & 0 & S_{12}^{\text{ant}} & \dots & S_{1,n}^{\text{ant}} & 0 \\ 0 & 0 & 0 & 0 & 0 & 0 \\ S_{21}^{\text{ant}} & 0 & S_{22}^{\text{ant}} & \dots & S_{2,n}^{\text{ant}} & 0 \\ \vdots & 0 & \vdots & \ddots & \vdots & 0 \\ S_{m,1}^{\text{ant}} & 0 & S_{m,2}^{\text{ant}} & \dots & S_{mm}^{\text{ant}} & 0 \\ 0 & 0 & 0 & 0 & 0 & 0 \end{bmatrix}. \tag{3.44}$$

The receiver noise temperature that we are interested in can be calculated using the following definition [24]

$$T_{\text{rcv}} = \frac{P_{\text{out}}^{\text{net}}|_{\langle \hat{\mathbf{N}} \rangle}}{P_{\text{out}}^{\text{net}}|_{\langle \hat{\mathbf{E}} \rangle}} T_0 \tag{3.45}$$

where $P_{\text{out}}^{\text{net}}|_{\langle \hat{\mathbf{N}} \rangle}$ and $P_{\text{out}}^{\text{net}}|_{\langle \hat{\mathbf{E}} \rangle}$ represents the total outgoing power from the LNA

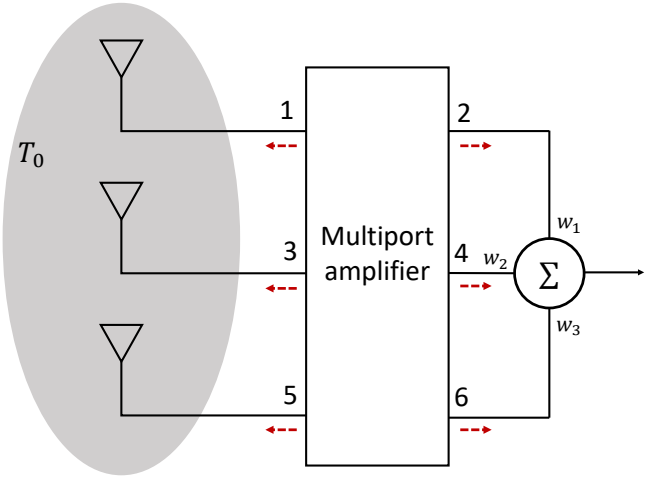

Figure 3.3: Block diagram representation of a three element phased array with the port numbering. The odd numbered ports are the input ports of the multiport amplifier connected to antennas while the even numbered ports are the output ports. Noise waves emerging at the output ports undergo a weight (w_i) and sum operation.

network due to $\langle\hat{\mathbf{N}}\rangle$ and $\langle\hat{\mathbf{E}}\rangle$ respectively.

To evaluate (3.45), we are interested in the outgoing noise power at the output side of the LNA network. Hence, the quantity of interest is a subset of (3.29). Since we have arranged the input ports to be odd numbered, we can remove all the odd rows and columns to form a submatrix $[\mathbf{A}_{\text{out}}]_{mn=2,4,\ldots,2N}$. This submatrix is the correlation matrix that can be used for characterizing the amount of noise coupling that exists in correlating arrays. To get the total coupled noise power after the summer at the output of a phased array, we simply multiply this submatrix by the summer weights as follows

$$P_{\text{out}}^{\text{net}}|_{\langle\hat{\mathbf{N}}\rangle} = \mathbf{w}\left[\mathbf{M}\langle\hat{\mathbf{N}}\rangle\mathbf{M}^{\dagger}\right]_{mn=2,4,\ldots,2N}\mathbf{w}^{\dagger} \tag{3.46}$$

$$P_{\text{out}}^{\text{net}}|_{\langle\hat{\mathbf{E}}\rangle} = \mathbf{w}\left[\mathbf{M}\mathbf{S}_{\text{LNA}}\langle\hat{\mathbf{E}}\rangle\mathbf{S}_{\text{LNA}}^{\dagger}\mathbf{M}^{\dagger}\right]_{mn=2,4,\ldots,2N}\mathbf{w}^{\dagger} \tag{3.47}$$

where $\mathbf{w}$ is a row vector containing the applied summer complex weights and $[\mathbf{A}]_{mn=2,4,\ldots,2N}$ represents a submatrix containing even numbered rows and columns of matrix $\mathbf{A}$. To ensure correct scaling in the calculated output power, the am-

plitude of $\mathbf{w}$ is scaled by the number of elements N such that $\sum_{i=1}^{N} |\mathbf{w}_i|^2 = 1$.

Substituting (3.46) and (3.47) into (3.45) gives

$$T_{\text{rcv}} = \frac{\mathbf{w}\left[\mathbf{M}\langle\hat{\mathbf{N}}\rangle\mathbf{M}^{\dagger}\right]_{mn=2,4,\ldots,2N}\mathbf{w}^{\dagger}}{\mathbf{w}\left[\mathbf{M}\mathbf{S}_{\text{LNA}}\langle\hat{\mathbf{E}}\rangle\mathbf{S}_{\text{LNA}}^{\dagger}\mathbf{M}^{\dagger}\right]_{mn=2,4,\ldots,2N}\mathbf{w}^{\dagger}} T_0. \tag{3.48}$$

The noise correlation matrix $\langle\hat{\mathbf{E}}\rangle$ for antenna arrays was not discussed in [36]. However, because the antenna array and load network are passive network, we can make use of Bosma's theorem [44] to calculate the noise correlation matrix which states that, for a given passive network at thermal equilibrium at a physical temperature of T_0

$$\langle\hat{\mathbf{E}}\rangle = kT_0\left[\mathbf{I} - \mathbf{S}_{\text{load}}(\mathbf{S}_{\text{load}})^{\dagger}\right]. \tag{3.49}$$

In addition, noise calculation often assumes noiseless loads at the output. We can easily apply this assumption by replacing $\mathbf{I}$ in (3.49) by

$$\mathbf{I}' = \begin{bmatrix} 1 & 0 & 0 & \ldots & 0 & 0 \\ 0 & 0 & 0 & \ldots & 0 & 0 \\ 0 & 0 & 1 & \ldots & 0 & 0 \\ \vdots & 0 & 0 & \ddots & 0 & \vdots \\ 0 & 0 & 0 & \ldots & 1 & 0 \\ 0 & 0 & 0 & \ldots & 0 & 0 \end{bmatrix}. \tag{3.50}$$

The advantage of the proposed PWF over Method 1 and 2 presented in Sect. 2.4.1 and 2.4.2 are as follows:

- Provides a standard framework that computes the incident and reflected power that can be used to calculate other quantities. This includes the calculation of embedded/active reflection coefficient and available/transducer/power gain. We demonstrated this by calculating τ using (3.40).

- Can be easily modified to include non-identical LNA by replacing the entries

in (3.42) and (3.43) with the appropriate values.

In the next section, we proposed a method for calculating radiation efficiency using the proposed definition of realised area.

3.3 Radiation Efficiency Using Modified POI

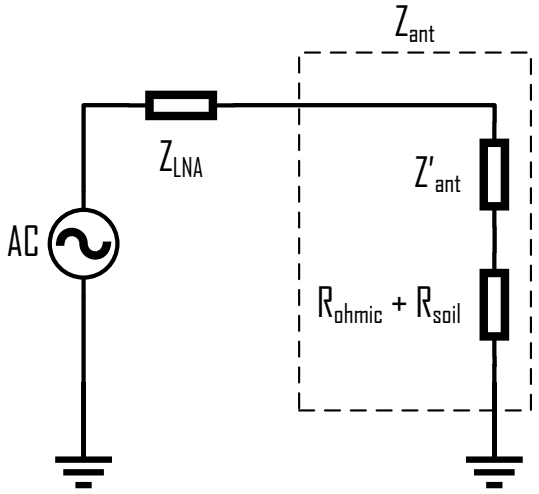

Figure 3.4: Simplified equivalent circuit of a lossy antenna loaded with LNA impedance in transmit mode. The Z_{ant} is the antenna impedance as obtained by S-parameter simulation/measurement or can be obtained via the port currents from simulation as both the excitation voltage and LNA impedance are known. The ohmic and soil losses are modelled as a resistor but in practice, these losses have a more complex form.

A different approach to compute η_{rad} is to use the pattern overlap integral (POI) method found in [24], which eliminates the need to know the injected power by reversing the problem from a transmit to receive antenna. The EEPs required for the POI method are based on open circuit condition of all neighbouring elements whereas, EEPs generated in [45] are based on loaded condition (LNA input impedance) of all elements. To reuse our pre-existing EEPs generated in [45], we will need to modify the POI formulation.

Fig. 3.4 shows an equivalent circuit of a transmit antenna. The total radiated power captured in the far-field pattern is due to the power dissipated by Z'_{ant}. This means that the far-field EEP does not directly contain the knowledge of any losses. The knowledge of losses are only apparent when compared to a relative value. By reversing the problem to receive mode, we can determine the noise power delivered to Z_{LNA} by Z'_{ant} at a nominal physical temperature T_a for a given EEP generated in transmit mode. If we assume identical LNA, then the total noise power delivered to the LNA given that the antenna sees an homogeneous sky at T_0 (refer to Appendix E) is given by

$$P'_{\text{LNA}} = \eta_{\text{rad}} k T_0 \mathbf{w} \mathbf{A}^{\text{sky}} \mathbf{w}^H \tag{3.51}$$

$$A^{\text{sky}}_{mn} = \Re\left\{ \frac{1}{Z_{\text{LNA}}} \right\} \frac{\eta_0}{\lambda^2} \int_0^{2\pi} \int_0^{\pi} \mathbf{l}_{\text{r},m} \cdot \mathbf{l}^{\dagger}_{\text{r},n} \sin\theta d\theta d\phi \tag{3.52}$$

and we define the realised length $\mathbf{l}_{\text{r}}$ which makes use of (2.15) as follows

$$\mathbf{l}_{\text{r},n} = \frac{Z_{\text{LNA}}}{Z_{\text{LNA}} + Z'_{\text{ant},n}} \mathbf{l}_{eff,n} \tag{3.53}$$

where $\mathbf{A}^{\text{sky}}$ is the noise correlation matrix due to homogeneous sky that is based on the POI formulation and $\mathbf{l}_{\text{p},n}$ relates the incident electromagnetic wave to the voltage seen at the load of the n^{th} element as a function of θ and ϕ.

Making use of the earlier derived result in (3.21), we can also re-write (3.51) as

$$P'_{\text{LNA}} = \tau \eta_{\text{rad}} k T_0 = 2 \frac{k T_0}{\lambda^2} \int_{\phi=0}^{2\pi} \int_{\theta=0}^{\pi} A_r^{\text{array}}(\theta, \phi) \sin\theta \; d\theta d\phi. \tag{3.54}$$

To obtain η_{rad}, we need a suitable reference value as mentioned before. We obtain this reference value by calculating the total noise power delivered to Z_{LNA} by Z_{ant} at physical temperature of T_a by using Bosma's theorem [44] or Twiss's theorem [24]. For our purposes, Bosma's theorem is a more convenient choice as it uses S-parameter natively. We can modify (3.34) to calculate the total delivered

external noise power at the input of the LNAs as follows

$$P_{\text{LNA}} = \tau k T_0 = \mathbf{w} \left[\mathbf{A}_{\text{in}}|_{\langle \hat{\mathbf{E}} \rangle} - \mathbf{A}_{\text{out}}|_{\langle \hat{\mathbf{E}} \rangle} \right]_{mn=1,3,\ldots,2N-1} \mathbf{w}^{\dagger}. \tag{3.55}$$

The radiation efficiency is then given by

$$\eta_{\text{rad}} = \frac{P'_{\text{LNA}}}{P_{\text{LNA}}}. \tag{3.56}$$

This is effectively how the POI method works. For verification, it was shown in [41] that the radiation efficiency calculated using (3.56) and (2.45) produced identical results within numerical error.

In the next section, we will consolidate all of the work presented thus far in this chapter to compute sensitivity of phased arrays.

3.4 Sensitivity Calculation Using A_r^{array}

As the realised area now relates incident plane wave to power delivered to the load, we now have to push the reference point of the remaining quantities in (2.1) to the load. We do this by multiplying the denominator with τ. The sensitivity of the array can now be calculated using

$$\frac{A_r^{\text{array}}}{\tau T_{\text{sys}}} = \frac{A_r^{\text{array}}}{\tau \eta_{\text{rad}} T_{\text{ext}} + \tau(1 - \eta_{\text{rad}}) T_a + \tau T_{\text{rcv}}} \tag{3.57}$$

where $\tau \eta_{\text{rad}} T_{\text{ext}}$ can be calculated directly using (3.21).

3.5 Chapter Summary

In this chapter, we proposed a physically motivated definition of realised area which is to be used in place of effective area when characterizing phased arrays. The formulation for realised area takes into account the degree of polarization (p) of the source and polarization mismatch factor ($\cos^2 \psi$). Additionally, we introduced a general and versatile method for computing receiver noise temperature of antenna arrays that can be extended to include phased arrays. Next, we showed that radiation efficiency can also be calculated from the proposed realised area and finally, we consolidated all of the proposed theory to derive the sensitivity formulation of phased arrays.

In the next chapter, we will begin verifying the proposed theory via electromagnetic (EM) simulation using FEKO.

Chapter 4

Verification of Method via EM Simulation

This chapter serves as a verification of theory proposed in the previous chapter before applying it to characterize an MWA tile. The verification of realised area and radiation efficiency will be done purely using EM simulation. Whereas, for the verification of receiver noise temperature, we will be using a combination of EM simulation of the MWA tile and measured data from previously characterized MWA LNA.

This chapter contains previously published results from the author's conference paper [23] in Sec. 4.2. The verification of radiation efficiency calculation found in Sect. 4.3 follows similar narrative to the author's published conference paper [41]. However, the results in [41] were based on a single element whereas, Sect. 4.3 was expanded to a four element example as presented in Sect. 4.1.

4.1 Verification of Realised Area of Phased Arrays

As part of the verification exercise, we aim to characterize a simple phased array. Fig. 4.1 shows a test array consisting of four elements that will be used

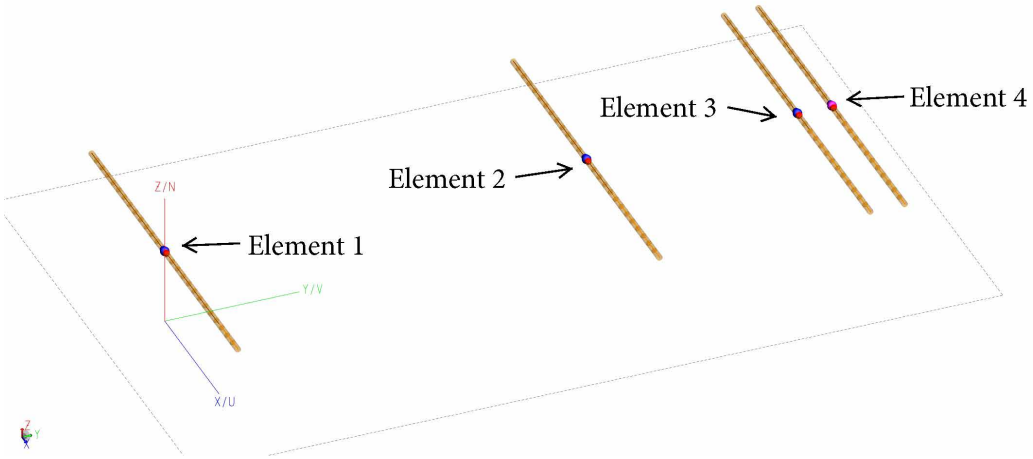

Figure 4.1: An array of antennas consisting of four 95 cm long dipole antenna that is aligned to the X-axis made of perfect electric conductor (PEC) material with a wire diameter of 1.5 cm. The elements were placed in parallel to each other along the positive Y-axis 20 cm above an infinite PEC ground plane. Element 1 was placed at the origin, element 2 was placed 1.1 m from origin, element 3 was placed 1.65 m away from origin and element 4 was placed 1.74 m away from origin. All elements were terminated with identical loads of 100 Ω.

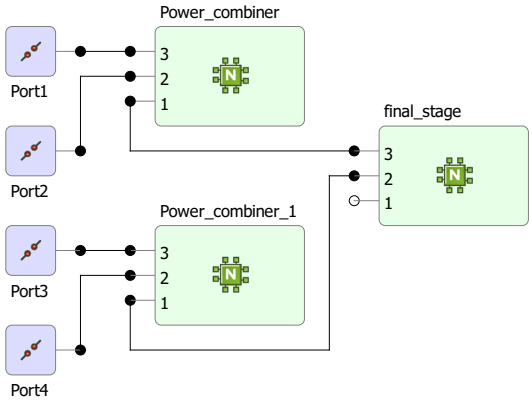

Figure 4.2: Network connection used in FEKO to combine the power from four elements into power delivered to a reference impedance matched load at port 1 (output port) of the final stage combiner.

throughout this verification process (excluding receiver noise temperature calculation verification).

An embedded electric far-field simulation was performed on each element and the corresponding electric far-field and port currents including coupled currents on adjacent elements were saved. Each element was excited with $V_{tx} = 1\angle 0^\circ$ V and a total of 218 frequency points were requested ranging from 49.92 MHz to 327.68 MHz in steps of 1.28 MHz. To verify (3.1) independently, we simulated the exact array in receive mode with a two-stage ideal Wilkinson power combiner attached at the ports of the elements to combine the power into a single port as shown in Fig. 4.2. The implemented combiner has the following S-parameter

$$S_{\text{comb}} = \frac{-j}{\sqrt{2}} \begin{bmatrix} 0 & 1 & 1 \\ 1 & 0 & 0 \\ 1 & 0 & 0 \end{bmatrix}. \tag{4.1}$$

As FEKO is unable to simulate an unpolarised source for the receiving array, we used a fully correlated polarization matched incident plane wave $\mathbf{E}_{\text{inc}}(-\bar{r}) = [e_\theta, 0]^T$ whereby

$$\langle \mathbf{E}_{\text{inc}}(-\bar{r}) \cdot \mathbf{E}_{\text{inc}}(-\bar{r})^\dagger \rangle = \begin{bmatrix} \langle |e_\theta|^2 \rangle & 0 \\ 0 & 0 \end{bmatrix}. \tag{4.2}$$

Under this condition of $p = 1$ and $\cos^2 \psi = 1$, (3.5) becomes

$$A_r^{\text{array}} = 4\frac{\lambda^2}{\eta_0} \Re\{Z_{\text{LNA}}\} \left[\left| \sum_{n=1}^{N} w_n E_{n,\theta} \right|^2 + \left| \sum_{n=1}^{N} w_n E_{n,\phi} \right|^2 \right] \tag{4.3}$$

Using the electric far-field results obtained from the embedded element pattern simulation, we can calculate the realised area of the array using (4.3) and thus, predict the power delivered to the load via the relation $P_{\text{load}} = A_r^{\text{array}} S_{\text{inc}}$.

Fig. 4.3 shows the comparison of delivered power based on the transmit and receive case. The various curves represents the predicted power delivered to

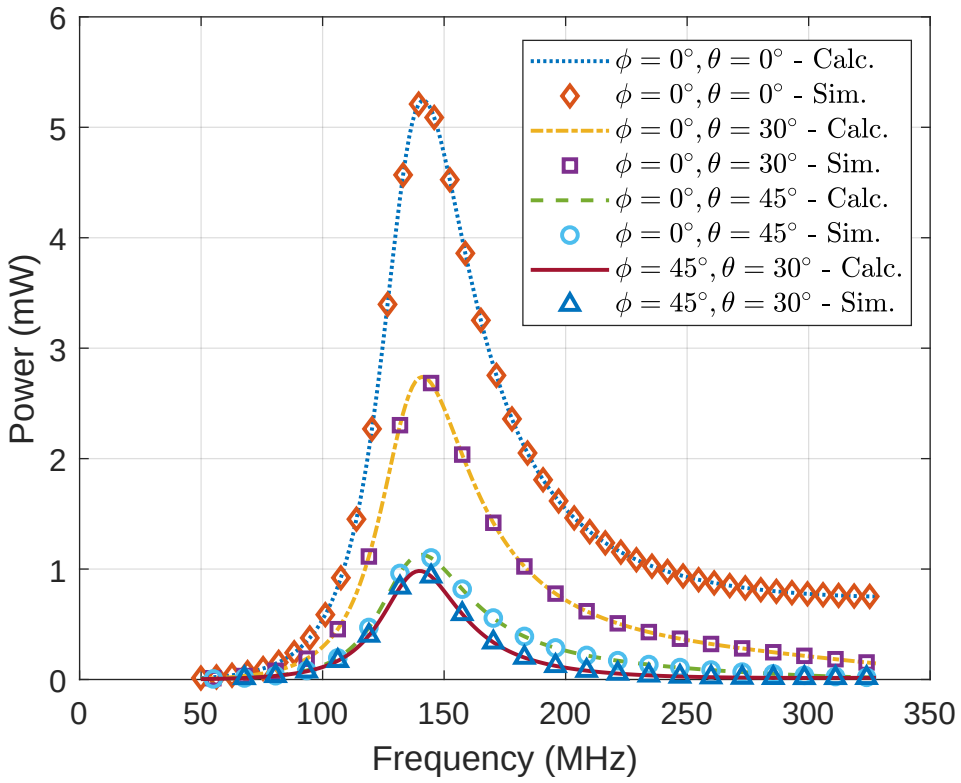

Figure 4.3: Comparison of power delivered to a reference impedance matched load at various incident angle. The 'Calc.' curves represents the calculated delivered power using (4.3) and the 'Sim.' points represents the delivered power to a reference impedance matched load as a receiving array with a 2-stage power combiner attached with an incident plane wave $\mathbf{E}_{\text{inc}}(-\bar{r}) = [e_\theta, 0]^T$.

the load based on the EEP simulation whereas, the data points are the power delivered to the load by the receiving array for a given plane wave at various incident angle. The results shows complete agreement between the predicted delivered power to values obtained from the simulated receiving array with a maximum absolute difference $< 0.013\%$. These results are significant because it implies that the derived expression (3.1) is valid.

Alternatively, we can directly compare the calculated realised area from the transmit case to the realised area of from the receive case via the relation (2.14). We also included additional incident angles for further verification. The results are presented in Fig. 4.4.

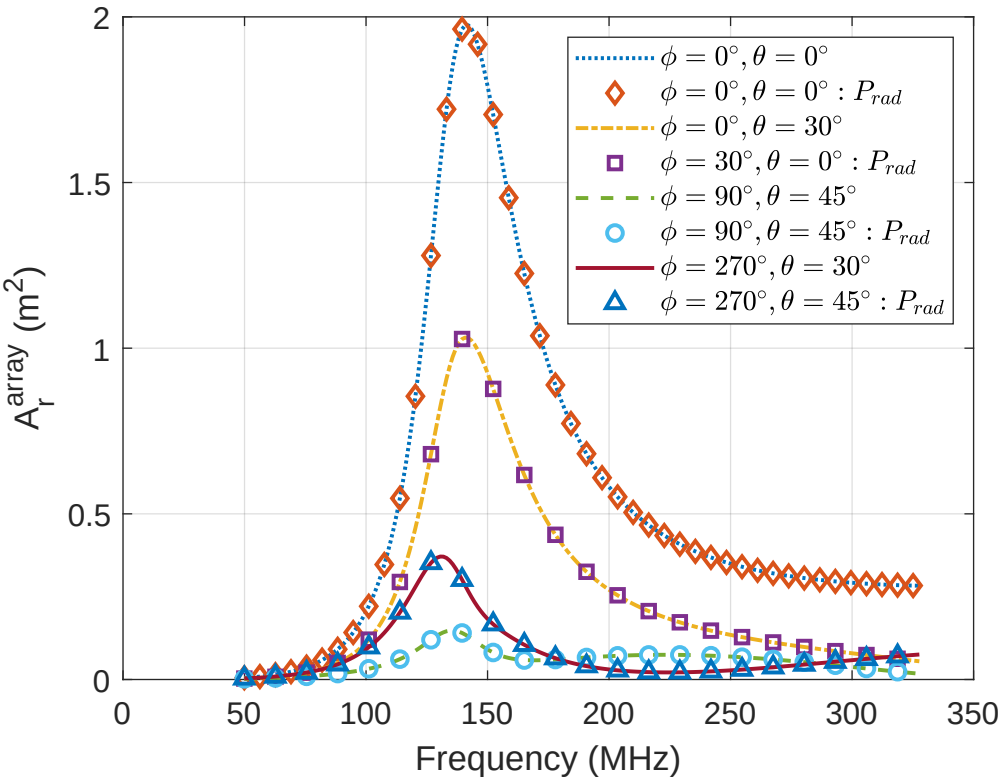

Figure 4.4: Comparison of realised area for an unpolarised source using the derived definition found in (3.5) and the classical definition found in (3.8). The curves represents the calculated realised area of the array using the derived (3.5) and the 'P_{rad}' data points represents the classical definition with $\eta_{\text{rad}} = 1$ (PEC material) and using τ as calculated using (3.9).

Again, we are seeing excellent agreement between the transmit and receive case. This concludes the verification of the realised area formulation for phased arrays. Moving on, we will verify the receiver noise temperature formulation.

4.2 Verification of Receiver Noise Temperature Calculation

Verification of the proposed method was performed in [23] but for completeness, it will be reproduced here. We have chosen to skipped ahead and calculated the

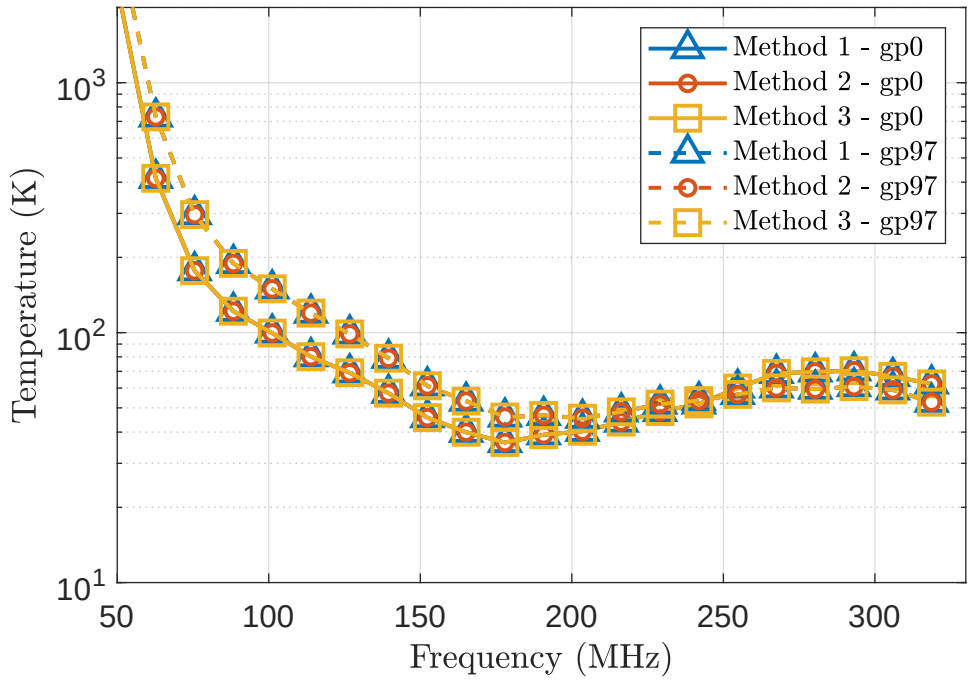

Figure 4.5: Comparison of MWA receiver noise temperatures computed using various methods over two separate pointings. The legend 'gp0' and 'gp97' represents a pointing direction of $\phi = 90°$, $\theta = 0°$ and $\phi = 45°$, $\theta = 42°$ respectively. Method 3 uses the power wave framework presented in Sect. 3.2.

receiver noise temperature of an MWA tile. As we are comparing our proposed method with two current methods mentioned in Chapter 2, the choice of array used is irrelevant. The S-parameters of the MWA tile was obtained via simulation which will be presented in Chapter 5, while the S-parameters and noise parameters of the MWA LNA were obtained from previous measurements done in [46]. We then apply the various T_{rcv} formulations presented in Sect. 2.4.1, 2.4.2 and 3.2.

Fig. 4.5 shows the comparison of between the three methods. We noted that all three different methods presented shows excellent agreement with each other at two pointing directions with the maximum reported absolute difference $< 0.007\%$. This validates the proposed formulation for the calculation of receiver noise temperature of phased arrays. Next, we will verify the formulation for

radiation efficiency.

4.3 Verification of Radiation Efficiency Calculation

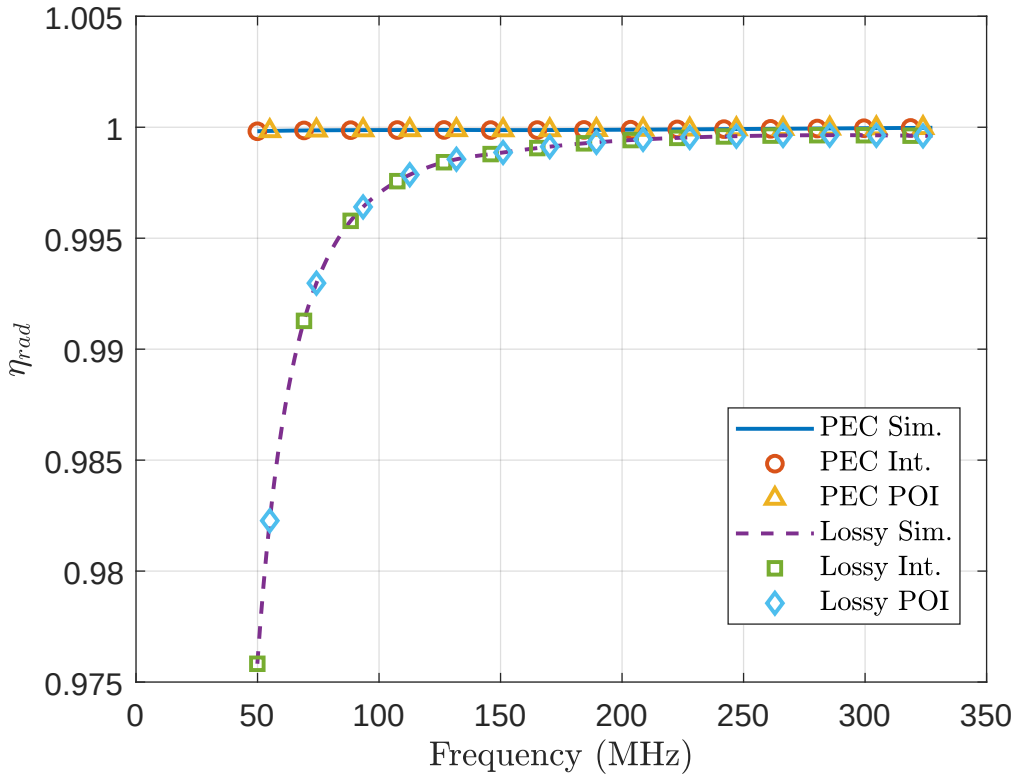

Figure 4.6: Efficiency calculation verification using the four element (Zenith pointed) example antenna array. The simulation was repeated with lossy antenna elements but keeping the PEC ground. The lossy material used was aluminium with a conductivity of 38.16×10^6 S m^{-1}. The 'Sim.' curves were generated by exciting all four elements simultaneously and obtaining the radiation efficiency directly from FEKO. The 'Int.' data points indicates that the radiation efficiency was calculated using the results of (3.54) while, 'POI' data points indicates it was calculated using the Pattern Overlap Integral as derived in (3.51).

Using the results from the simulated antenna array as shown in Fig. 4.1, we calculated the radiation efficiency using the formulation presented in Sect. 3.3.

We repeated the simulation and calculation with lossy antenna elements with conductivity of 38.16×10^6 S m^{-1} but leaving the infinite ground as PEC. We then compute τ using (3.9) and $\tau\eta_{\text{rad}}$ using both (3.51) or (3.54) for validation. For the lossless case (PEC), we expect that $\tau\eta_{\text{rad}} = \tau$ as $\eta_{\text{rad}} = 1$. Fig. 4.6 shows the efficiency comparison between the direct output from FEKO and the calculated efficiency for the lossless and lossy case. The maximum absolute difference between the 'POI' method and 'Int' method are within numerical error ($< 1 \times 10^{-13}\%$), while the absolute difference between the 'Int' method and 'Sim' are $< 2 \times 10^{-4}\%$. The results validates the derived formulation presented in Sect. 3.3.

4.4 Chapter Summary

In this chapter, we verified the formulations presented in Chapter 3 using an example phased array consisting of four elements. For the verification of the realised area, we simulated the four element array in transmit and receive mode. We found excellent agreement in the derived realised area obtained from the transmit case to the realised area obtained from the receive case. Using the same example array, we verified the proposed radiation efficiency formulation to the standard formulation found in Sect. 2.5 for both lossy and lossless elements.

We verified the proposed receiver noise temperature calculation formulation with two current methods found in current literature using the MWA tile and LNA. In the next chapter, we will characterize an MWA tile.

Chapter 5

Verification of Method via Astronomical Observations

This chapter contains the characterization of an MWA tile and additional verification using astronomical observation. We begin by outlining the details of the embedded element simulation performed on the MWA tile which is the key result required in the formulations presented in Chapter 3.

We then present the realised area of an MWA tile for the Zenith pointed case and two additional pointing angles. As we do not have observational results for direct comparison of both realised area and radiation efficiency, we have opted to calculate the inverse of the sensitivity which is equivalent to the System Equivalent Flux Density ($SEFD$) in which observational data are available.

For the comparison of receiver noise temperature, a drift scan observation was performed to obtain the receiver noise temperature of the MWA tiles. This was then compared to the predicted value using the proposed method in Sect. 3.2.

5.1 Characterization of an MWA tile

Following the successful verification of method using a four element phased array, we now proceed to characterize an MWA tile. This process starts with the

embedded element simulation of an MWA tile using an electromagnetic (EM) simulator FEKO licensed by Altair Engineering. Once the EEP simulation was completed, we proceeded with the calculation of the realised area of an MWA tile.

Before looking at the results for the realised area, it is worth discussing the simulation set-up. The details of the set-up are broken down into several sub-sections as follows:

- Sect. 5.1.1 contains the MWA dipole model used during the EM simulation. Each dipole is the antenna element that constitutes an MWA tile.

- Sect. 5.1.2 contains the modelling of the input impedance of the MWA LNA used for each dipole.

- Sect. 5.1.3 contains the modelling details of the MWA tile's metallic ground-screen.

- Sect. 5.1.4 contains the soil modelling of the Murchison Radio-astronomy Observatory.

- Sect. 5.1.5 contains the flow diagram and details of the embedded element pattern simulation workflow that was implemented in FEKO.

5.1.1 MWA Dipole

When it comes to simulating an antenna, we can reconstruct the 'as manufactured' antenna geometry in the simulation package and perform the simulation run. However, the drawback is that the structure can be complex and therefore more computationally expensive and slower to run. Furthermore, not every fine detail in the geometry contributes towards the final simulated electric far-field pattern. For this reason, a simplified wire model was used [47] to model the MWA antenna elements. Fig. 5.1 shows the constructed model that was meshed

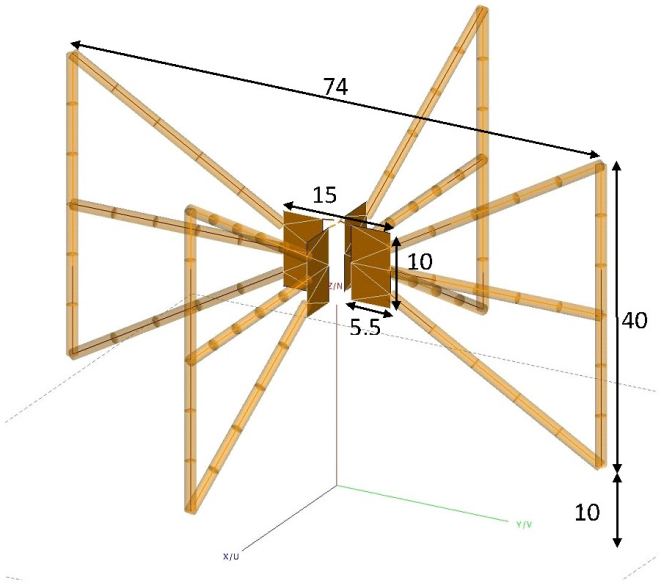

Figure 5.1: MWA dipole model used in the simulation. Units are in cm.

in CADFEKO[1].

While the actual MWA dipoles are constructed using aluminium, it was assumed to be a perfect electric conductor (PEC) in the simulation. This was done because the ohmic losses of aluminium (see Fig. 4.6) is negligible when compared to soil losses furthermore, using PEC material quickens the simulation runtime.

5.1.2 MWA Dipole LNA Loading

The input impedance of the LNA presents a complex load to the MWA dipole and therefore will affect the array's electric far-field pattern as previously discussed. Hence, the input impedance of the LNA was modelled using a RLC lumped circuit and was included in the simulation by attaching it to all of the ports. The RLC parameters used are as shown in Table 5.1 [48]. Fig. 5.2 shows the comparison between the measured value and the modelled RLC lumped circuit of the LNA. The typical absolute difference is within $\approx 10\%$ which is within the bounds of component-to-component variation.

[1]CADFEKO is part of the simulation environment in FEKO.

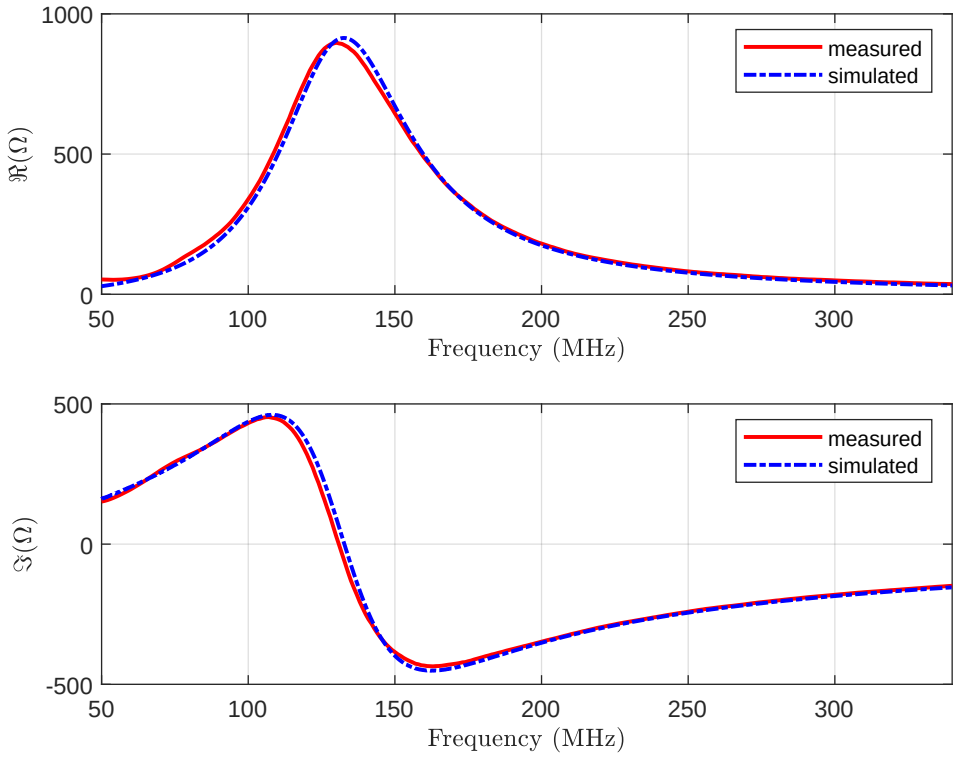

Figure 5.2: Comparison between measured LNA impedance and simulated lumped circuit model that was implemented in FEKO using the LS and LP card. The top and bottom graph, shows the comparison of the real and imaginary part respectively.

5.1.3 MWA Tile Groundscreen

The MWA tile includes the use of a metal gridded mesh that is 500 × 500 × 2 × 2 cm. The metal mesh doubles as a ground plane and mechanical means of securing the dipoles onto the ground. The MWA is capable of performing observations up to 300 MHz which equates to a wavelength of ≈ 1 m. Since the size of the grid is 2 cm × 2 cm, relative to the highest observable wavelength it is 50 times smaller and hence as a first order approximation the gridded mesh can be simulated using a solid square of PEC material which speeds up the simulation time.

Parameter designator	Value
L_s	2 nH
R_p	914 Ω
L_p	450 nH
C_p	3.2 pF

Table 5.1: MWA LNA lumped circuit parameters. Where L_s represents a series inductor, R_p, L_p and C_p are the parallel resistor, inductor and capacitor respectively.

5.1.4 MRO Soil Modelling

Based on soil samples taken from the MRO, a microwave characterization was performed to determine its typical permittivity and conductivity at 2% moisture content by weight [49]. These parameters were used to create a dielectric material in FEKO which defines a planar multilayer substrate as the soil. The green coloured plane in Fig. 5.3 represents the modelled MRO soil. Table 5.2 contains the relative permittivity and conductivity for a given frequency point [50].

Frequency (MHz)	Relative permittivity (ϵ_r)	Conductivity ($\times 10^{-3}$ S m^{-1})
48	6.440	11.428
57	6.222	12.117
66	6.049	12.769
75	5.907	13.381
98	5.641	14.806
121	5.454	16.106
144	5.317	17.324
167	5.215	18.503
189	5.133	19.692
247	4.987	22.69
304	4.890	25.845
361	4.829	28.789

Table 5.2: MRO soil permittivity and conductivity at 2% moisture used during simulation.

5.1.5 Tile Excitation, Feed Points, Frequency Range and Requests

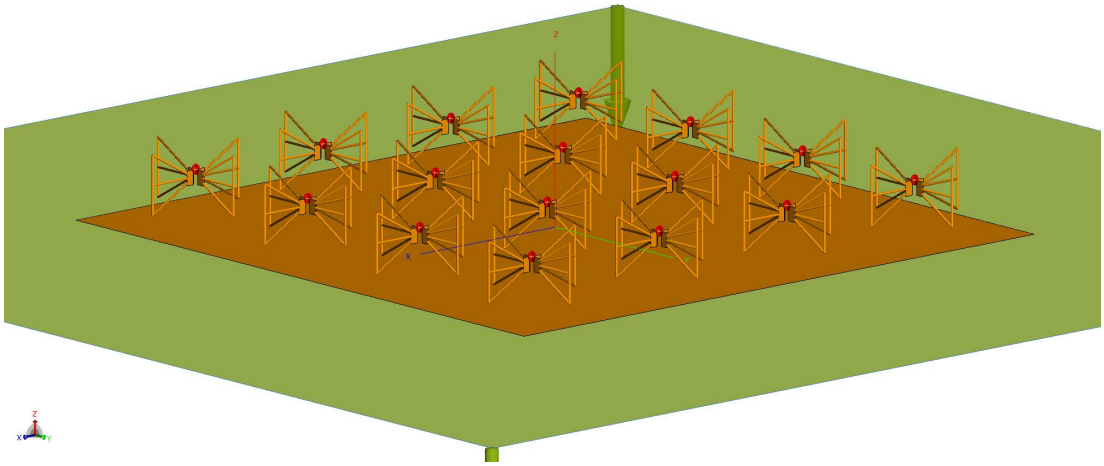

Figure 5.3: MWA FEKO model set-up. The X-axis points towards East and the Y-axis points North.

Fig. 5.3 shows the constructed MWA tile using a combination of CADFEKO and EDITFEKO. The full embedded element simulation requires that only one dipole for a given polarization be excited sequentially all elements terminated by a known load. Therefore, the total number of simulation runs is 32 runs (16 dipoles $\times$ 2 polarization) per frequency point. The frequency range of interest are 49.92 MHz to 327.68 MHz at 1.28 MHz increment; in total there are 218 frequency points. The feedwires were created in EDITFEKO[2] and each was assigned a unique name. This enabled selective excitation of the feedwire and thus allowing the full embedded pattern simulation to be executed in one continuous run via loops created in EDITFEKO as shown in Fig. 5.4.

[2]EDITFEKO is part of the simulation environment in FEKO.

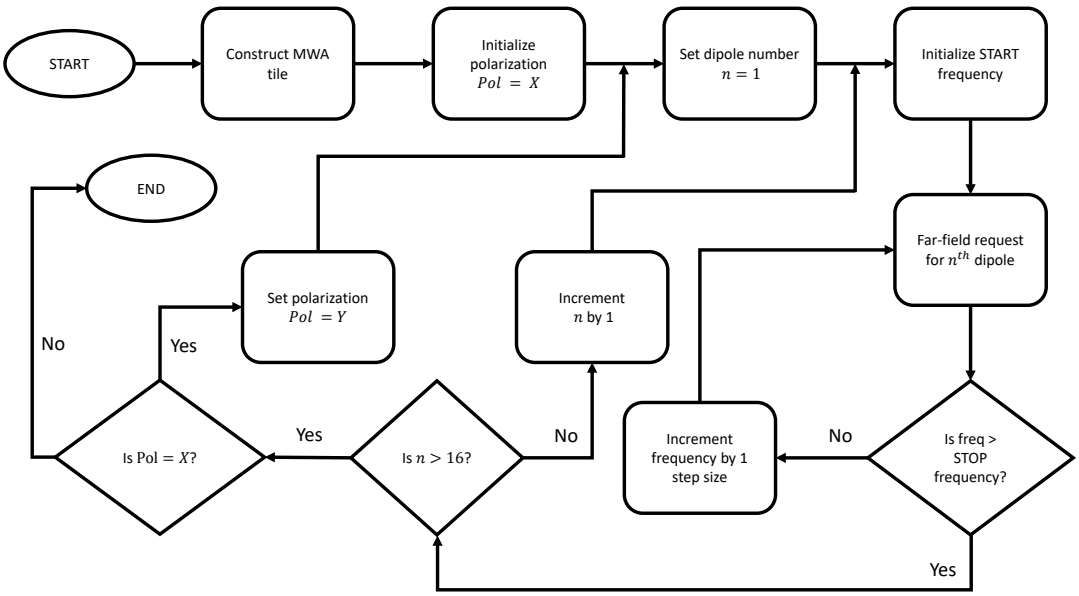

Figure 5.4: Process flow implemented in EDITFEKO for full embedded element pattern simulation for MWA. A single MWA dipole without the central hub was first constructed in CADFEKO with the dimensions shown in Figure 5.1.The 16 elements, ground mesh plane, soil and simulation requests was then set-up in EDITFEKO.

5.2 Realised Area of MWA

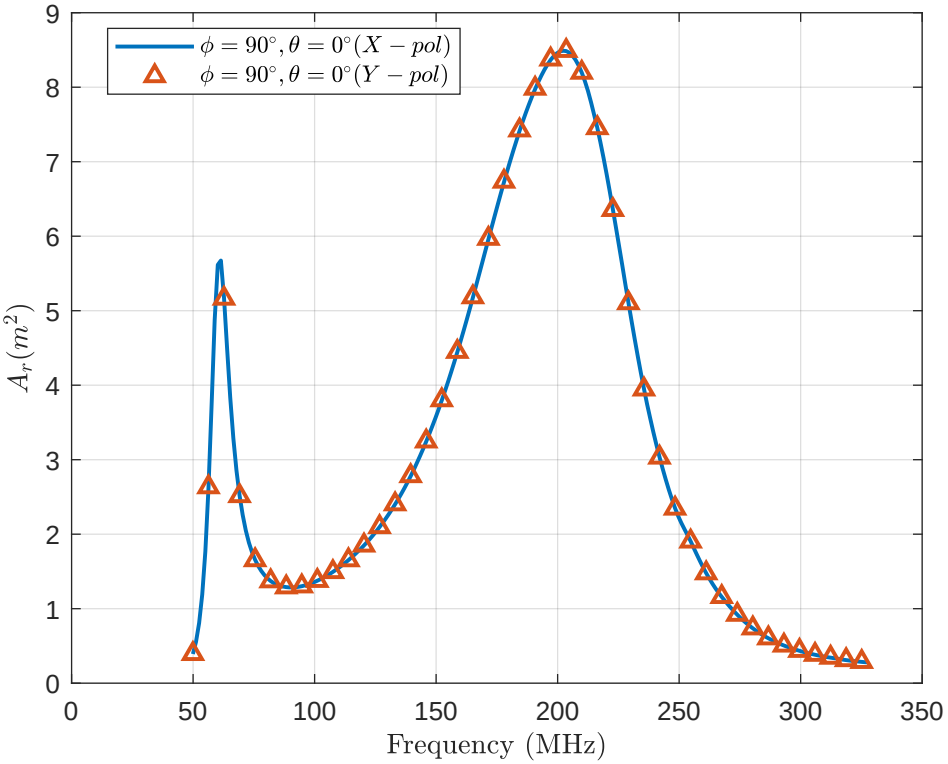

Figure 5.5: Realised area of the MWA tile at pointing angle of $\phi = 90°, \theta = 0°$.

Following the completion of the embedded element pattern simulation of an MWA tile, we calculated the realised area of the tile using (3.16) for $p = 0$. Fig. 5.5 shows the calculated realised area of an MWA tile when pointed at Zenith ($\phi = 90°, \theta = 0°$), while Fig. 5.6 shows the calculated realised area of the MWA tile at two different pointing angles.

When the tile is set to point at Zenith, both the realised area of X-polarization and Y-polarization are identical due to the symmetry of the MWA tile. However, at different pointing angles there are slight variations in realised area. This behaviour is expected as the $\mathbf{E}_{tx}$ of the X and Y-polarization are not identical. Next, we present the radiation efficiency of an MWA tile.

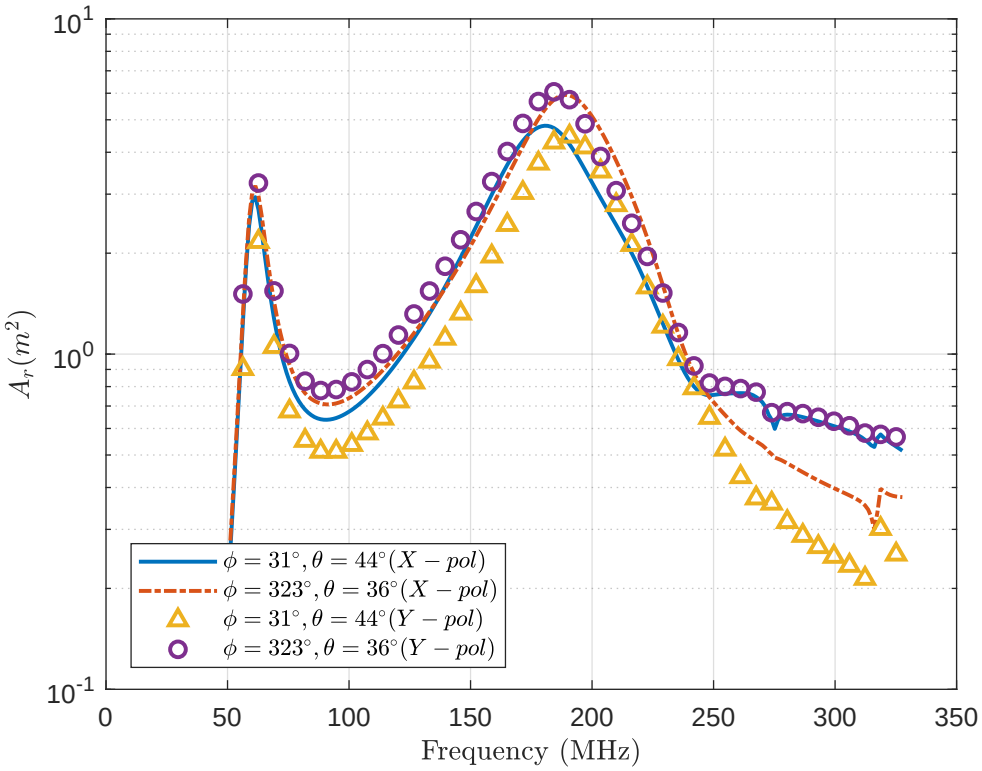

Figure 5.6: Realised area of the MWA tile at pointing angle of $\phi = 31°, \theta = 44°$ and $\phi = 323°, \theta = 36°$.

5.3 Radiation Efficiency of MWA

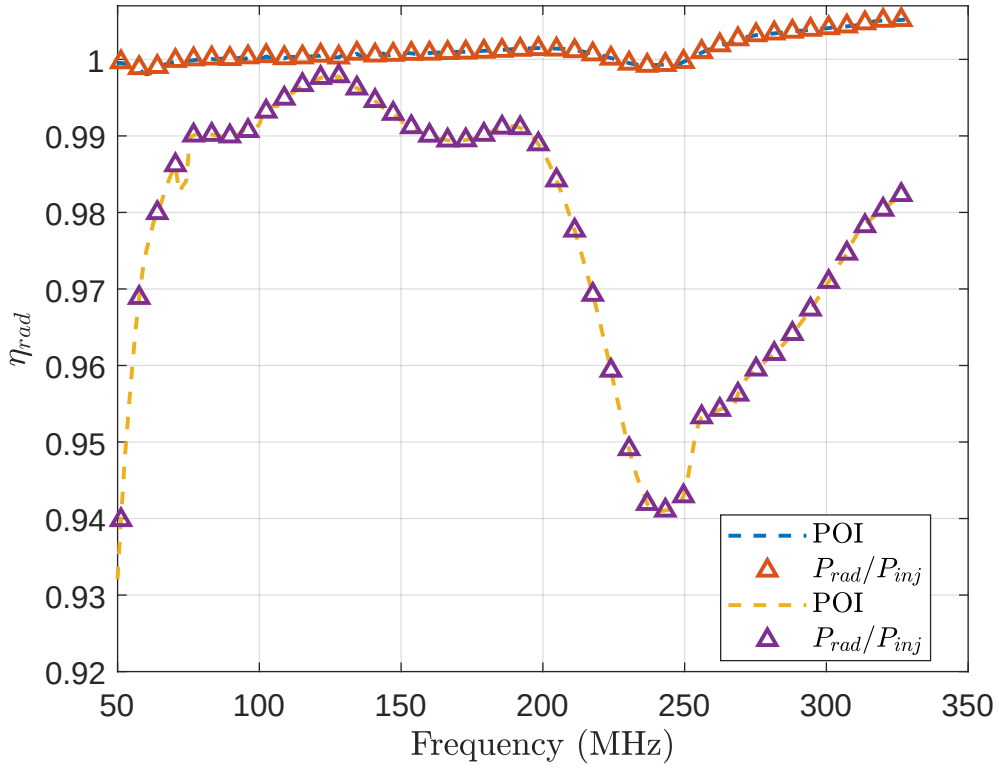

Figure 5.7: Calculated efficiency of the MWA at zenith. The PWF and $P_{\text{rad}}/P_{\text{inj}}$ curve represents the efficiency calculated using the power wave framework and 'standard framework' respectively. The EEPs used to compute both results are based on prior simulation presented in [45], whereby the radiation efficiency is solely due to soil losses as all the metallic elements used during simulation was perfect electric conductors (PEC).

Using the results from Sect. 5.2, we calculated the delivered power to the LNA given under homogeneous isotropic condition using (3.54) at a resolution of 0.2° in θ and ϕ. To calculate (3.55), we extracted the S-parameter of the array using the results from Sect. 5.1. Following that, we calculated the radiation efficiency of an MWA tile using (3.56).

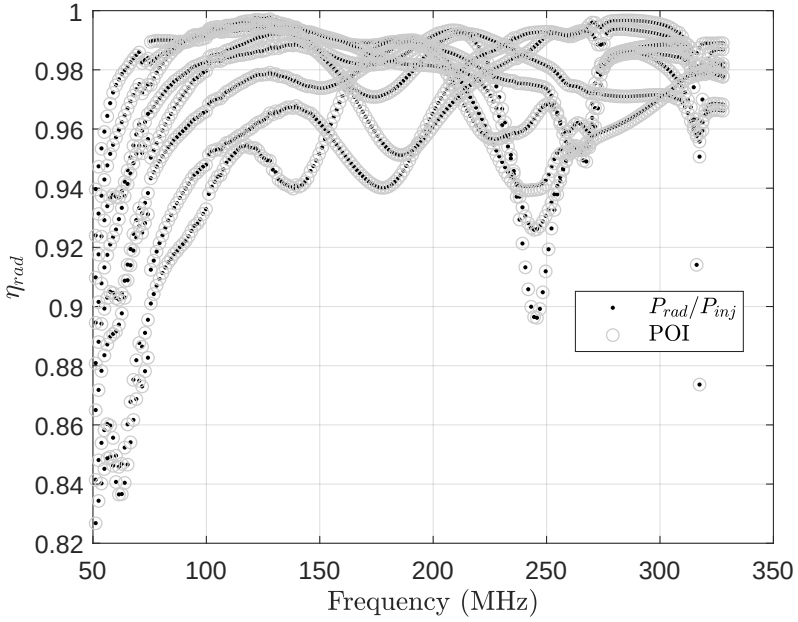

Figure 5.8: Comparison of radiation efficiency calculation at different 8 pointing angles. The 'POI' data points were calculated using (3.56), while the 'P_{rad}/P_{inj}' data points were calculated using (2.45).

As an additional verification, we re-simulated the MWA tile using infinite PEC ground to ensure that the formulation would return a sensible value of $\eta_{\text{rad}} = 1$. Furthermore, we also calculated η_{rad} using (2.45) by making use of knowledge of port currents I_{tx} for the computation of P_{inj}. The calculated radiation efficiency of a Zenith pointed MWA tile using two methods are shown in Fig. 5.7.

We note that for the PEC case, the efficiency reported was as high as 100.5% which is due to the limitations of the simulation package. As demonstrated in [40], the efficiency obtained using Method-of-Moments (MoM) based solver such as FEKO for PEC materials ranges from 100% to 100.7%.

Next, we compared the radiation efficiency at 8 different pointing angles as shown in Table 5.3 for further verification using two different methods. The results are shown in Fig. 5.8. The difference in results using the two methods over 197 pointing angles are shown in Fig. 5.9 whereby the largest absolute difference (Δ) is no larger than 2×10^{-3} which indicate excellent agreement.

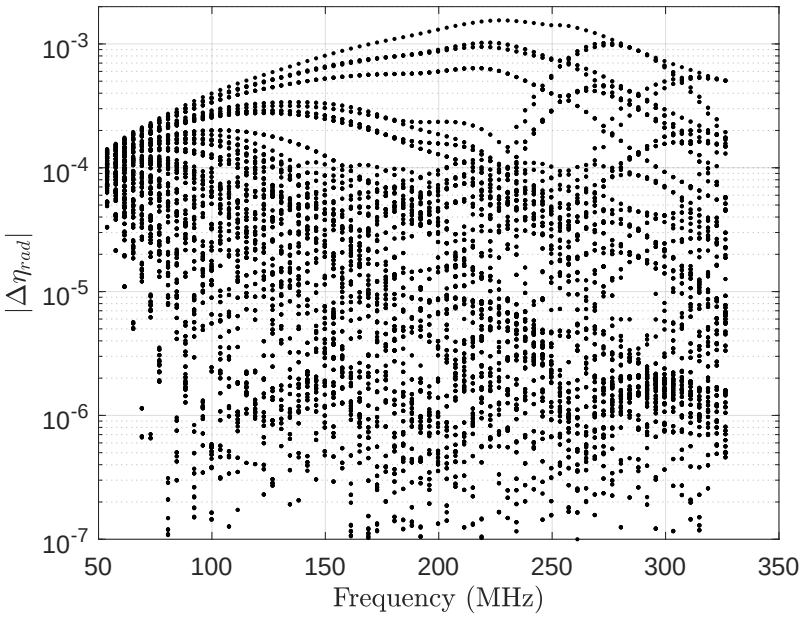

Figure 5.9: Absolute difference in calculated radiation efficiency using POI method and standard P_{rad}/P_{inj} formulation. The differences were calculated over all 197 pointing angles.

Table 5.3: Gridpoints selected for radiation efficiency calculation.

Gridpoint number	ϕ	θ
0	90°	0°
25	90°	20.8°
50	14°	29.3°
75	270°	32°
100	135°	42.1°
125	251.6°	56.1°
150	45°	57°
175	164.1°	59.7°

In the next section, we will present the verification of the receiver noise temperature of an MWA tile using astronomical observation.

5.4 Receiver Noise Temperature of MWA

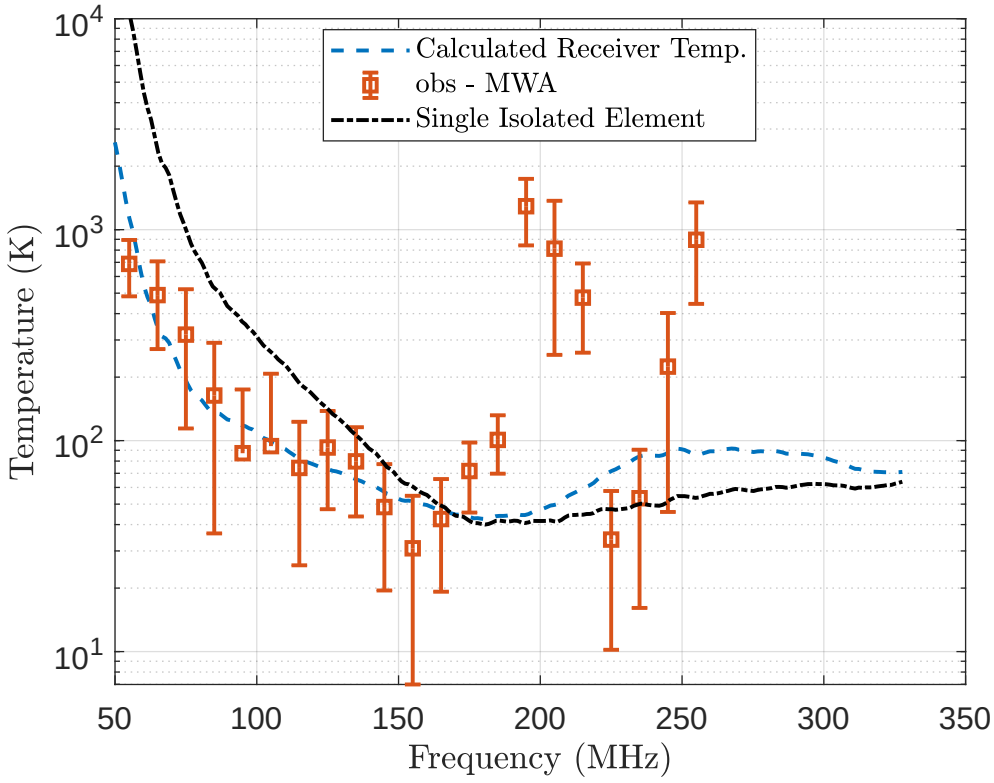

Figure 5.10: Comparison between the calculated (dash curve) and observed receiver noise temperature of an MWA tile. The mean and standard deviation of the observed receiver noise temperature represented by the data points was calculated over 128 tiles. A single isolated element result represented by the dot-dash curve is presented as a comparison.

To further verify our comparison done in Sect. 4.2, we obtained the receiver noise temperature of the MWA tiles using astronomical drift scan method as seen in [51–53]. The observation was performed on the 9th June 2014 by setting all the MWA beamformers to point at Zenith and allowing astronomical sources to drift through the MWA beam. The expected power detected as a function of

frequency ν by a phased array is given by

$$P(\nu) = g(\nu)k\left[\eta_{\text{rad}}T_{\text{ant}}(\nu) + T'_{\text{rcv}}(\nu)\right] \tag{5.1}$$

$$T'_{\text{rcv}}(\nu) = T_{\text{rcv}}(\nu) + \left[1 - \eta_{\text{rad}}(\nu)\right]T_a \tag{5.2}$$

where $g(\nu)$ is the power gain of the array signal chain and T_{ant} is the antenna temperature due to sky noise.

The receiver noise temperature ($T'_{\text{rcv}}(\nu)$) obtained using this method includes noise temperature due to losses because the drift scan method is unable to differentiate T_{rcv} from $\left[1 - \eta_{\text{rad}}(\nu)\right]T_a$. We obtained $T'_{\text{rcv}}(\nu)$ by modelling the predicted power as

$$P'(\nu) = g(\nu)k\left[\eta_{\text{rad}}T^{\text{model}}_{\text{ant}}(\nu) + T'_{\text{rcv}}(\nu)\right] \tag{5.3}$$

and $T^{\text{model}}_{\text{ant}}$ is estimated as

$$T^{\text{model}}_{\text{ant}}(\nu) = \frac{\int_\Omega B(\nu,\theta,\phi)T(\nu,\theta,\phi)d\Omega}{\int_\Omega B(\nu,\theta,\phi)d\Omega} \tag{5.4}$$

where $T(\nu,\theta,\phi)$ is the sky brightness temperature obtained from "Haslam Map" [54] at frequency ν, which has been scaled down from the original 408 MHz to lower frequencies by multiplying by a factor $(\nu/408\,\text{MHz})^{-2.55}$ [55] and $B(\nu,\theta,\phi) = E(\nu,\theta,\phi)_{\text{ff}} \cdot E(\nu,\theta,\phi)^\dagger_{\text{ff}}$ is the simulated far-field power pattern as a function of θ and ϕ. An example image of the power pattern is provided in Fig. 5.11.

Least square optimization was then performed on the predicted $P'(\nu)$ with the observed $P(\nu)$ to solve for $g(\nu)$ and $T'_{\text{rcv}}(\nu)$ respectively. Based on (5.3), the power received by every tile is expected to be proportional to $T^{\text{model}}_{\text{ant}} + T'_{\text{rcv}}(\nu)$, assuming that the sky model used in (5.4) is a good representation of the true sky (accuracy of sky model is of order $\approx 10\%$). We have identified that this relation holds best for the 12 to 14 hours range of the Local Sidereal Time (LST) [3] (see

[3]LST is an hour angle between vernal equinox and local meridian

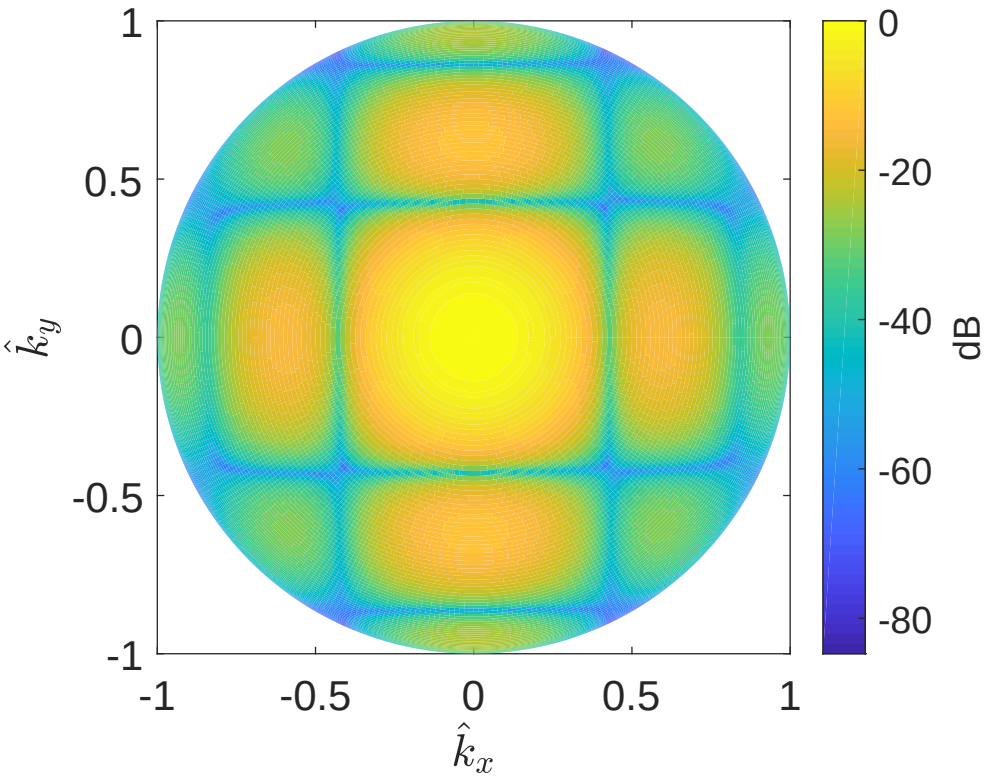

Figure 5.11: The normalized far-field power response $B(\nu, \theta, \phi)$ of a zenith pointed MWA tile at 160 MHz.

also [52] for a more detailed justification of LST range selection procedure). Once we have the calculated values, we fitted this model to measured data using least squares to solve for $g(\nu)$ and $T'_{\text{rcv}}(\nu)$.

Using the measured noise and S-parameters of the LNA obtained in [46], we calculated the expected noise receiver temperature and radiation efficiency of the MWA tile and use the results to compute (5.2). Fig. 5.10 shows the comparison between the calculated and observed receiver noise temperature of the MWA. A single isolated T_{rcv} is also included for comparison.

The frequency ranges of 170 MHz to 220 MHz and 240 MHz and above show radio frequency interference (RFI) which causes the observed receiver noise temperature to increase dramatically. The error bars generated are based on the standard deviation of receiver noise temperature calculated over 128 MWA tiles

used during observation. The computed receiver noise temperature follows (5.2) which includes the radiation efficiency of the array.

The most interesting result that emerged from this calculation is the reduction of receiver noise temperature over the single isolated element at lower frequencies. There are two possible explanation for this result by recalling (3.48). First, there was a reduction in the net noise power at the output due to internal noise as described by the numerator. Secondly, there was an increase in the net noise power at the output due to external noise as described by the denominator.

For the second possible explanation given, it can be intuitively visualized by expressing the denominator of (3.48) in the form of transducer gain. The definition of transducer gain is the ratio of delivered power at the output of the network to the available power at the input of the network [56]. Given this definition, we can easily compute the transducer gain of an MWA tile using

$$G_T = \frac{P_{\text{out}}^{\text{net}}|_{\langle\hat{\mathbf{E}}\rangle}}{kT_0} \tag{5.5}$$

$$= \frac{\mathbf{w}\left[\mathbf{M}\mathbf{S}_{\text{LNA}}\langle\hat{\mathbf{E}}\rangle\mathbf{S}_{\text{LNA}}^{\dagger}\mathbf{M}^{\dagger}\right]_{mn=2,4,\ldots,2N}\mathbf{w}^{\dagger}}{kT_0}. \tag{5.6}$$

Substituting (5.5), into (3.48) gives

$$T_{\text{rcv}} = \frac{\mathbf{w}\left[\mathbf{M}\langle\hat{\mathbf{N}}\rangle\mathbf{M}^{\dagger}\right]_{mn=2,4,\ldots,2N}\mathbf{w}^{\dagger}}{G_T}T_0. \tag{5.7}$$

Using the relation derived in (5.7), the decrease in T_{rcv} could now be viewed as the increase in transducer gain.

We can investigate which of the two possible explanation is more accurate by firstly plotting the total power delivered (numerator) to the output due to internal noise alone over 197 different pointing angles as seen in Fig. 5.12. Firstly, the mean value shows us that the internal noise contribution of a single tile is approximately equal to that of a single isolated element. However, we are seeing $\approx 48\%$ to 900% decrease in T_{rcv} in the 50 to 140 MHz region. Secondly, using the

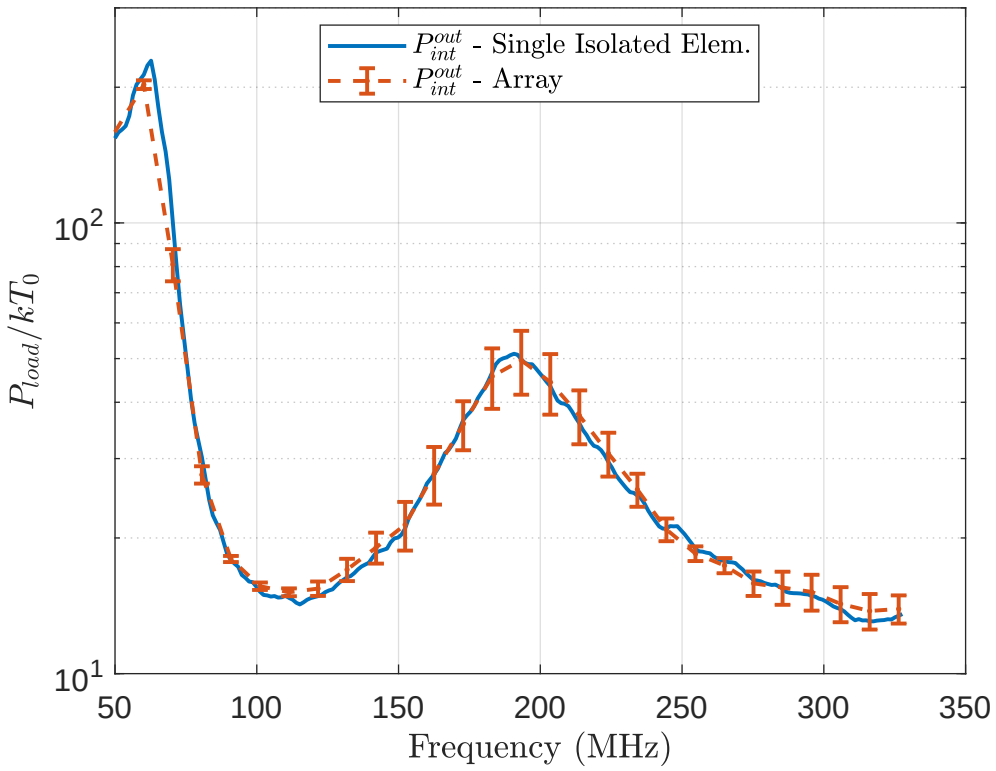

Figure 5.12: Delivered noise power to a Z_0 matched load due to internal sources alone normalized to kT_0. The solid line represents the delivered noise power by a single isolated MWA element whereas the dashed line represents the mean and standard deviation of power delivered by the MWA array over 197 optimal MWA pointing angles.

calculated standard deviation values in Fig. 5.12, the level of change in $P_{\text{out}}^{\text{net}}|_{\langle\hat{\mathbf{N}}\rangle}$ in the 50 to 140 MHz region is less than 8.2%. Therefore, we conclude that the dominant mechanism for the reduction in T_{rcv} seen at this frequency range was due to increasing G_T at all 197 pointing angles.

5.4.1 Transducer Gain

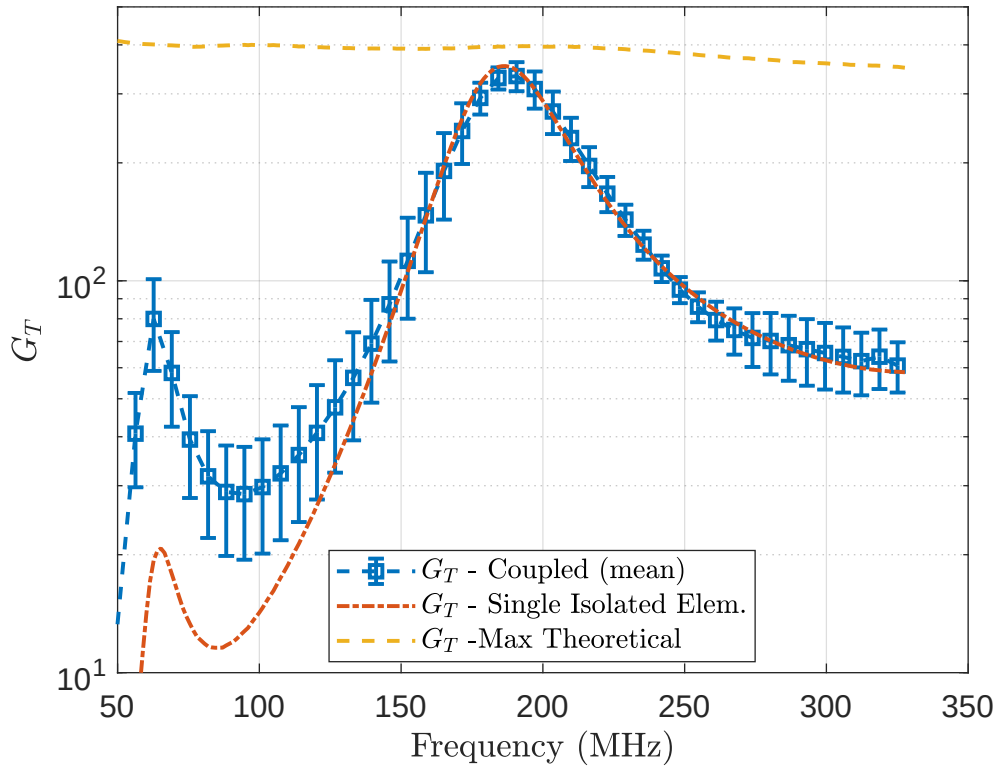

Figure 5.13: Comparison of the transducer gain achievable by the MWA LNA. The theoretical maximum transducer gain (dash curve) of a single element was obtained by placing conjugately matched load at all frequencies at the input of the LNA. The data points represent the mean and standard deviation of the tile's G_T obtained over all 197 optimal pointing angles. For comparison, G_T of a single isolated element (dot-dash curve) is shown.

The increase in G_T is rather unexpected as intuitively we would have expected internal noise coupling to be the dominant factor in changing T_{rcv}. To verify that the results presented remain physically valid, we recalculated G_T for a single isolated element given that the antenna was conjugately matched at all frequencies to the LNA's input impedance. This calculation sets the absolute upper

limit which the G_T of the array must not exceed as it would imply the source is delivering more power than the available source power (kT_0).

We compared this maximum value to the mean and standard deviation of the array's G_T over all 197 pointing angles. Fig. 5.13 shows the results of this comparison and validates that indeed our G_T for a single tile remains physically valid. Furthermore, we observe on average a $\approx 19\%$ to $\approx 600\%$ increase of the tile's G_T over the single isolated element in the 50 to 140 MHz region. Therefore, both the results shown in Fig. 5.12 and 5.13 confirms that indeed the dominant mechanism which causes the reduction in T_{rcv} seen in Fig. 5.10 was due to increasing G_T.

The increase in G_T could be caused by changes in the embedded impedances of the MWA dipoles due mutual coupling in the array environment and/or correlated power due to external noise power being coupled through adjacent elements. We can investigate the dominant mechanism of increasing G_T by splitting the matrix $\left[\mathbf{M}\langle\hat{\mathbf{N}}\rangle\mathbf{M}^{\dagger}\right]_{mn=2,4,\ldots,2N}$ in (3.46) into diagonal terms and cross terms. This would allow us to determine the net contribution of these terms separately that make up the calculated $P_{\text{out}}^{\text{net}}|_{\langle\hat{\mathbf{E}}\rangle}$.

As shown in Fig. 5.14, the power delivered due to the diagonal terms alone are almost equal to that of a single isolate element. This means that the change in G_T due to changing embedded impedance was not the dominant mechanism. The increase in G_T is mainly caused by correlated power in the 50 to 140 MHz region.

We can gain more insight from Fig. 5.14, by observing that the diagonal entries of $\left[\mathbf{M}\langle\hat{\mathbf{N}}\rangle\mathbf{M}^{\dagger}\right]_{mn=2,4,\ldots,2N}$ are not affected by phase changes in the complex weights. Therefore, the delivered power due to the diagonal terms alone will not change as a function of pointing angles. Whereas, the cross terms are affected by phase changes and could either correlate to produce a net positive delivered power or anti-correlate and produce a net negative delivered power. This implies that G_T arrays with high mutual coupling (large cross terms) will change with

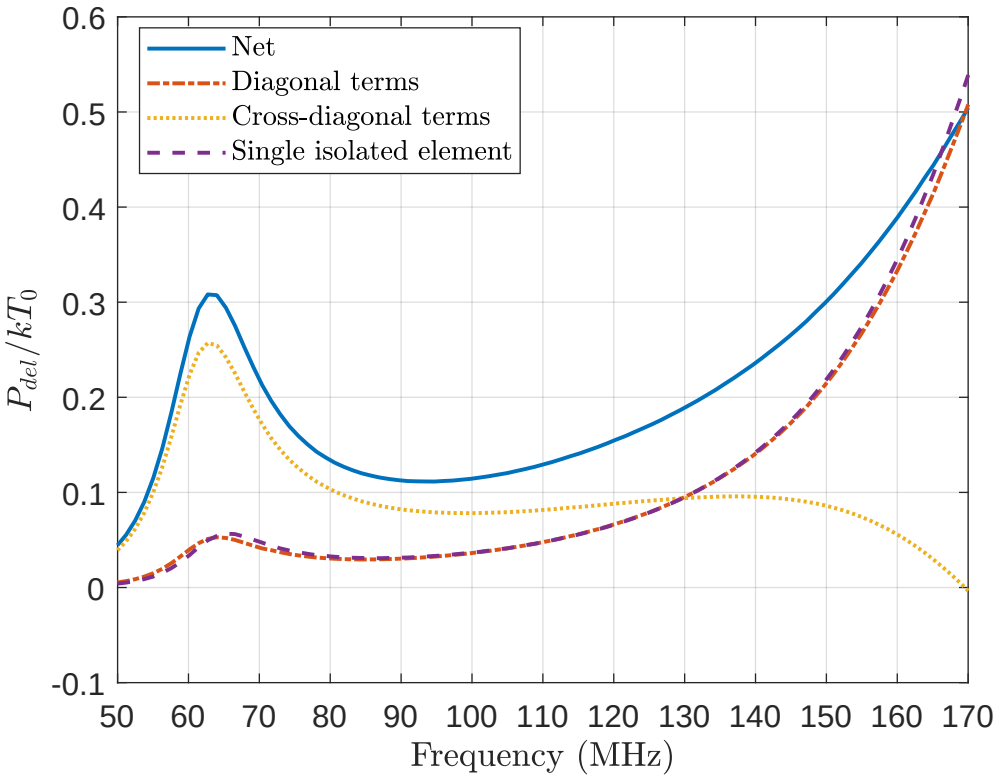

Figure 5.14: External noise power delivered to the output of a Zenith pointed MWA tile due to homogeneous sky normalized to kT_0. The dashed curve represents the total delivered power due to external sources for a single isolated element, the dotted curve represents the additional delivered power to the MWA tile due to mutual coupling (cross terms of (3.47)) while the dot-dash curve represents external noise power that is directly delivered to the array (diagonal terms of (3.47)). The solid curve is the net sum of both the additional and direct power delivered to the MWA tile. The negative value represents power loss due to destructive interference of the noise wave due to mutual coupling.

changing pointing angles as seen in Fig. 5.13 and this causes a change in T_{rcv}.

Combining all the results resented thus far, we then computed the sensitivity of an MWA tile in the next section.

5.5 Sensitivity of MWA

Tying all the results presented in the previous sections together, we calculated the sensitivity of the MWA tile. To make comparison with observed sensitivity, we have chosen to present the sensitivity in the form of System Equivalent Flux Density (SEFD) as commonly measured by astronomers from real data. SEFD is defined as the condition in which the signal-to-noise ratio (SNR) is equivalent to unity [21] and it is inversely proportional to sensitivity. Based on our definition of sensitivity, the SEFD can be calculated using

$$SEFD = k\frac{\tau\eta_{\text{rad}}T_{\text{ext}} + (1-\eta_{\text{rad}})\tau T_a + \tau T_{\text{rcv}}}{A_r^{\text{array}}} \tag{5.8}$$

where setting $k = 1.38$ will yield $SEFD$ in units of kJy[4].

The $SEFD$ was evaluated for an observed astronomical source 3C444 observed on the 7^{th} December 2016 at 10:24:39 to 10:31:35 UTC. The observation time and date is identical to that used during the characterization of the Engineering Development Array (EDA) [52]. Fig. 5.15 and 5.16 shows the comparison of the calculated and observed average $SEFD$ of ≈ 56 tiles for the X-polarization and Y-polarization respectively. We see good agreement between the calculated and observed $SEFD$. This indirectly validates all previous results obtained in Sect. 5.2-5.4 that was used to calculate the $SEFD$ of an MWA tile.

[4]where $1Jy = 10^{-26}$ W/m^2/Hz.

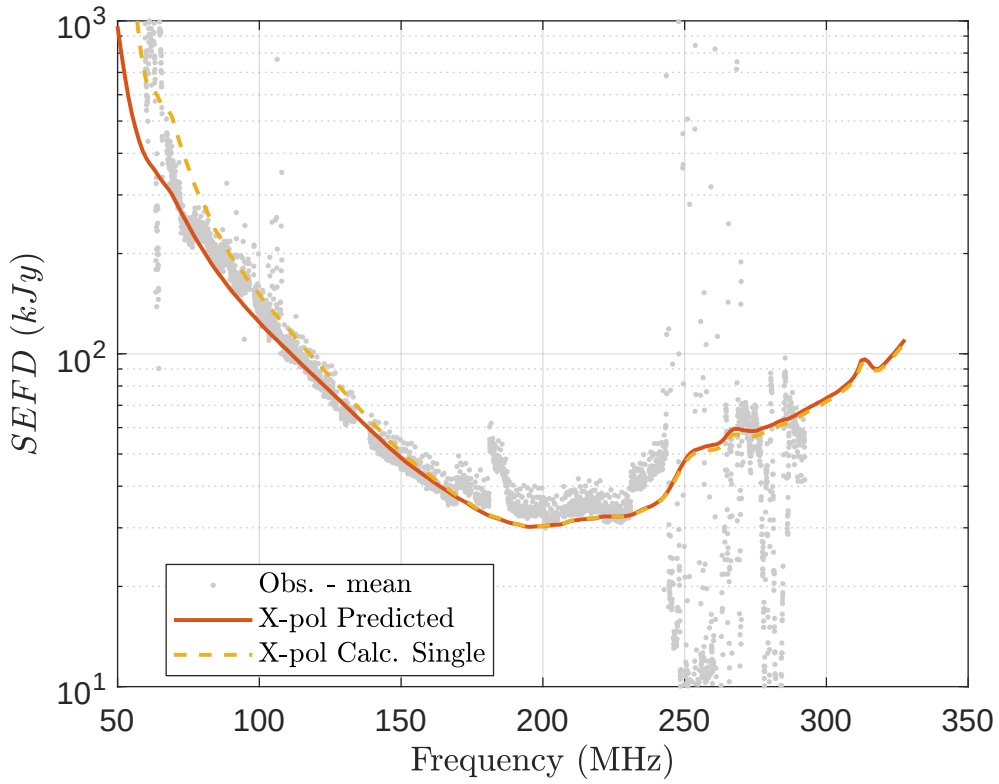

Figure 5.15: Comparison of calculated $SEFD$ to the average $SEFD$ of MWA tile (X-polarization) at a pointing angle of $(\phi = 153.43°, \theta = 15.37°)$ obtained from astronomical observation. The observation was taken on the 7^{th} December 2016 at 10:24:39 to 10:31:35 UTC. The observed source was 3C444 and on average the source was located at $(\phi = 151.46°, \theta = 18.3°)$ during the entire observational period in which A_r^{array} was evaluated at. The observed data points displayed are from an average of ≈ 56 different MWA tiles. The dashed curve represents the $SEFD$ of the MWA tile given that the T_{rcv} was substituted with the results from the single isolated element. The missing data points around 137 MHz are due to strong interference from Orbcomm satellite [57] and were removed before processing. At ≈ 242 to 270 MHz and ≈ 280 to 288 MHz the data shows signs of radio frequency interference (RFI). The RFI in the $242 - 272$ MHz band is due to military satellite and this was documented in [57] however, the source RFI interference in the $275 - 285$ MHz was not identified.

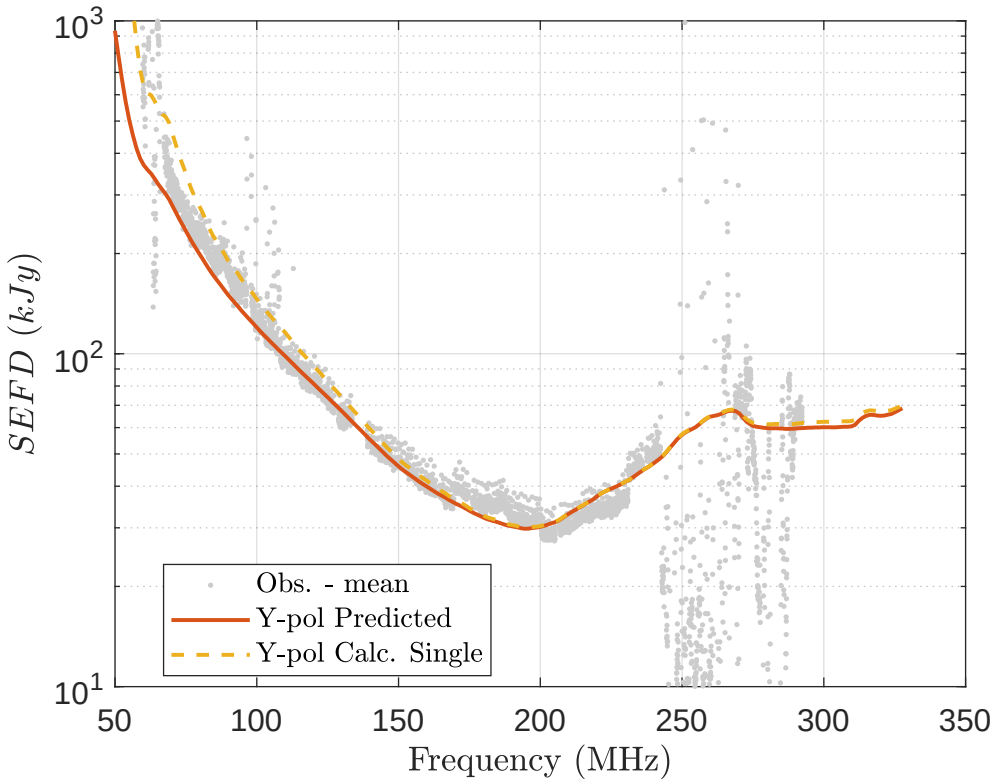

Figure 5.16: $SEFD$ of MWA tile (Y-polarization) at a pointing angle of ($\phi = 153.43°, \theta = 15.37°$). The observational details are identical to the X-polarization.

As a first order approximation, $SEFD$ is typically evaluated using T_{rcv} of a single isolated element represented by the dashed curve in Fig. 5.15 and 5.16. We observe a slight overestimation of $SEFD$ when comparing the two curves. However, this first order approximation does give a good estimation as the T_{sys} used in the $SEFD$ calculation which is dominated by the antenna temperature due to sky. This is generally true for low-frequency observations in the region of 50 to $\approx$ 100 MHz as the average sky temperature is in excess of $>$ 1000 K.

This results implies that for a quick analysis, the first order approximation can be used. However, more observational data at different pointing angles are required to further validate this hypothesis which is beyond the scope of this thesis.

5.6 Chapter Summary

In this chapter, we presented the characterization of an MWA tile. We showed that the realised area of an MWA tile varies with pointing angles and across polarization which was expected for phased arrays. Following that we, computed the radiation efficiency of an MWA tile and verified it using standard formulation found in Sect. 2.5. Next, we compared the calculated receiver noise temperature using our proposed method to results obtained from observational drift scan. We showed that on average, the observed receiver noise temperature is in agreement with the calculated values which further validates the proposed method.

We note that the receiver noise temperature of an MWA tile is lower when compared the single isolated element counterpart. We demonstrated that this was due to increasing transducer gain caused by mutual coupling. While the reduced T_{rcv} is a positive consequence of this, we note that T_{rcv} varies as a function of pointing angles due to changing transducer gain. Finally, we combined the all results obtained to compute the $SEFD$ of an MWA tile which is inversely proportional to sensitivity. Based on the average observed $SEFD$ taken over ≈ 56 tiles, we see excellent agreement with the predicted $SEFD$.

Chapter 6

Conclusion

We have developed the tools required to characterize antenna arrays that is extendable phased arrays taking into account mutual coupling. Using these tools, we can calculate the realised area of receiving elements, radiation efficiency, noise coupling, receiver noise temperature and sensitivity/SEFD.

Through the development of the tools, we showed the limitation of standard definitions when it comes to calculating effective area of phased arrays and presented a consistent and correct definition in the form of realised area. We also demonstrated that an older power wave framework used to compute noise figure of multiport amplifier networks can be recast to compute receiver noise temperature of phased arrays.

Using the proposed definition of realised area, we demonstrated that we can calculate the radiation efficiency of the phased array using the knowledge of the array mismatch factor which can be computed with the aid of the power wave framework (PWF). We verified the formulation by using an elementary phased array consisting of four antenna elements as an example. The agreement with the calculated and simulated data gave confidence that the proposed formulation is valid. We then used the developed tools to characterize an operational radio telescope which is the Murchison Widefield Array.

We calculated the receiver noise temperature of an MWA tile using measured

noise parameters and S-parameter of the low-noise amplifier while the radiation efficiency was calculated from simulated data. To verify our results, we performed a drift scan observation and extracted the receiver noise temperature of the MWA's tile. We showed that our calculated T_{rcv} matches the observational data and therefore further validates our formulation. We noted the unexpected decrease in receiver noise temperature of the array when compared to a single isolated element. Using the PWF, we gave insight into the decrease of the array's T_{rcv} which was caused by the mutual coupling which allowed external noise to increase at the output. This resulted in an increase in transducer gain of the MWA tile and therefore reducing the receiver noise temperature.

As we are unable to directly obtain the realised area and radiation efficiency of the MWA's tile via observational data, we have opted to calculate the System Equivalent Flux Density of the MWA tile in which measured results are available. We found excellent agreement between the calculated and observed SEFD which indirectly validates the computed realised area, radiation efficiency, receiver noise temperature and mismatch factor of the array. We also noted that the tools developed in this thesis are sufficiently general and can be extended to arrays with different configurations e.g. correlating elements in an array.

In summary, we presented appropriate tools of characterizing receiving elements that has been rigorously tested and validated with both simulation and observational data. Looking forward, we plan to use these tools for characterizing the next generation of low-frequency radio telescope such as the SKA-low [58]. At the conclusion of this thesis, we have identified potential future work as an extension which is discussed in detailed in subsequent sub-sections.

6.1 Implementation of tools in database

As mention in Sect. 1.6, the implementation of the developed tools to a database can be done as a follow-up to this thesis. The uploaded tools will need to be accompanied by another publication to further consolidate and all the work presented here and to include more observational $SEFD$ results at multiple pointing angles and beam pattern verification using drift scan as seen in [52]. The publication will also serve as a comprehensive manual of the tools developed here.

6.2 Direct measurement of noise correlation

Thus far, the verification of noise coupling has been done indirectly. To further exercise the formulation presented in (3.29), a direct measurement is required. This involves building a two-element interferometer located inside an anechoic chamber. The outputs of the receiving elements will be directly attached to a correlator thus allowing us to probe the full matrix entries of (3.29) for direct comparison.

6.3 Tool extension

The computation of receiver noise temperature using (3.48) in its current form is an analysis tool. While it can analyse arbitrary arrays, it is unable to contribute towards the design phase of minimizing receiver noise. An interesting research topic is to further extend the formulation to allow insight during the array design stage.

Appendix A

Submitted Paper

Noise Temperature of Phased Array Radio Telescope: The Murchison Widefield Array and the Engineering Development Array

Daniel Ung, Marcin Sokolowski, Adrian Sutinjo, David B. Davidson

***Abstract*—This paper presents a framework to compute the receiver noise temperature (T_{rcv}) of two low-frequency radio telescopes, the Murchison Widefield Array (MWA) and the Engineering Development Array (EDA). The MWA was selected because it is the only operational low-frequency Square Kilometre Array (SKA) precursor at the Murchison Radio-astronomy Observatory, while the EDA was selected because it mimics the proposed SKA-Low station size and configuration. It will demonstrated that the use of an existing power wave based framework for noise characterization of multiport amplifiers is sufficiently general to evaluate T_{rcv} of phased arrays. The calculation of T_{rcv} was done using a combination of measured noise parameters of the low noise amplifier (LNA) and simulated S-parameters of the arrays. The calculated values were compared to measured results obtained via astronomical observation and both results are found to be in agreement. Such verification is lacking in current literature. It was shown that the receiver noise temperatures of both arrays are lower when compared to a single isolated element. This is caused by the increase in mutual coupling within the array which is discussed in depth in this paper.**

***Index Terms*—Aperture arrays, Mutual coupling, Noise receiver temperature, Radio Telescope, Radio astronomy**

I. Introduction

The computation of receiver noise temperature (T_{rcv}) and radiation efficiency (η_{rad}) of a phased array can be complex in nature due to the presence of mutual coupling. However, there are many frameworks for computing it. For example, the computation of receiver noise temperature using a voltage framework was demonstrated in [1], while other power based methods are covered in [2] and [3] which involves the calculation of available gain of the phased array. For radiation efficiency calculation, power based frameworks was demonstrated in [4]–[6].

The two main motivations for being able to calculate T_{rcv} prior to building the telescope are, the cost effectiveness of characterizing the telescope and insight into the noise coupling mechanism. Both of these abilities are useful when designing and characterizing next generation radio telescopes such as the Square Kilometre Array (SKA) [7].

The first contribution of this paper is to calculate the T_{rcv} of the Murchison Widefield Array (MWA) [8], [9] and the Engineering Development Array (EDA) [10]. The calculated T_{rcv} will be validated against measured results obtained via astronomical observations using similar methods seen in [10]–[12]. The measured T_{rcv} using astronomical observations also includes the effects of mutual coupling. Such comparisons are not found elsewhere in literature, which forms the major contribution of this paper.

The authors are with the International Centre for Radio Astronomy Research/Curtin Institute of Radio Astronomy, Curtin University, Bentley, WA 6102, Australia (e-mail: daniel.ung@icrar.org).

Draft 1, January 10, 2020

Figure 1. An MWA tile connected to a beamformer (white rectangular box). Each antenna element contains an LNA in the central hub (white cylindrical container). Photo credits: Curtin University and MWA Collaboration.

Figure 2. The Engineering Development Array. Photo credits: Curtin University and MWA Collaboration.

The MWA is the first operational precursor telescope to the SKA-Low located at the Murchison Radio-astronomy Observatory (MRO) in the Shire of Murchison, Western Australia. The telescope consists of 256 phased arrays [9] called 'tiles' as shown in Fig 1. Each tile contains 16 antenna elements, called MWA dipoles, placed in a 4×4 configuration spaced 1.1 m apart over a 5×5 m metallic ground mesh. Each element houses a low noise amplifier (LNA) in the central hub and the output signal travels through a phase matched coaxial cable to the beamformer. The maximum spread of the tiles that make up the overall telescope is approximately 5.3 km. The computation of T_{rcv} at the tile level is of interest as

it is required for determining the sensitivity of the MWA tile [8].

The EDA uses the same dipole elements as the MWA but houses a modified LNA[(1)]. The EDA consists of 256 elements placed in a pseudo random configuration spanning 35 m diameter over a metallic ground mesh [10] as shown in Fig 2. It was designed to mimic the proposed SKA-Low station configuration and therefore making it a perfect test bed as it shares nearly identical elements to the MWA. The comparison of EDA's T_{rcv} to MWA gives insight of the impact of mutual coupling on T_{rcv} which will be presented later.

The receiver noise temperature can also be measured using the Y-factor method as seen in [13], [14], which uses a sufficiently large absorber as the hot source which covers the main beam and the sky as the cold source. At around the $\approx 50-100$MHz region, the opposite takes place as the average sky temperature is in the thousands of Kelvin. The sky is the hot source while the absorber is the cold source. However, the sky temperature exponentially decays with increasing frequency with a transition frequency at ≈ 150 MHz. At the transition frequency, $T_{hot} = T_{cold}$ and thus the Y-factor method will fail. In addition, large absorber structure is required to be built which limits the practicality of the Y-factor method to smaller arrays making unsuitable for the MWA tile and EDA.

The second contribution of this paper is to demonstrate that a power wave based framework (PWF) found in [15] can be recast to compute T_{rcv} of a phased array. The fundamental concept of this framework is the computation of incident and reflected power. This method was selected because it is based in the S-parameters domain which is more closely connected with the authors previous work in this area [16].

Additionally, the formulation can be easily modified to compute various quantities such as active/embedded reflection coefficient, transducer/available gain, and incident/reflected power of given source(s) that includes all coupling paths. An example of this will be shown by re-using this framework to calculate delivered power to the array for radiation efficiency calculation in subsequent section.

The receiver noise temperature of an array can be calculated using [4]

$$T_{\text{rcv}} = \frac{P_{\text{av}}^{\text{rcv}}}{P_{\text{av}}^{\text{amb}}} T_0 \tag{1}$$

$$= \frac{P_{\text{av}}^{\text{rcv}}}{kG_A} \tag{2}$$

where $P_{\text{av}}^{\text{rcv}}$ is the available receiver noise power at the output, $P_{\text{av}}^{\text{amb}}$ is the available ambient temperature noise power at the output due to isotropic sky at T_0 and G_A is the available gain of the low-noise amplifier for a single element but for an array, it represents the available receiver gain.

Effectively, both the previously mentioned voltage and power framework works by computing a similar ratio described by (1). The proposed framework for calculating T_{rcv} using [15] was shown to be consistent with current methods in [17] when compared to the voltage and power framework found in [1], [3].

[(1)]The LNA was slightly modified to have a larger bandwidth (50-300 MHz). Apart from this slight change, the LNA is identical to that used in the MWA (70-300 MHz).

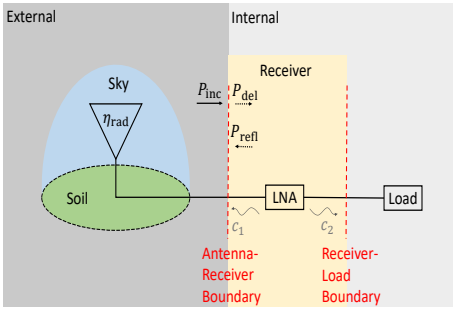

Figure 3. Overall system diagram of an antenna connected to an LNA. The system is made up of an external part which consists of an antenna, sky and soil while the internal part consists of the receiver (LNA) and a load. The boundary indicates a region in which a mismatch of impedance could occur and hence causes incident power waves to that boundary be either partially or fully reflected. The notation P_{inc} indicates the incident power, P_{del} is the delivered power, which is the difference between the incident power and the reflected power P_{refl}. The LNA also emits noise waves at the input and output terminals labelled c_1 and c_2 respectively. The noise temperature is related to power spectral density by the relation $P = kT$ where k is Boltzmann's constant and therefore they can be used interchangeably. Noise temperatures calculated involving active devices do not correspond to a physical temperature.

The active reflection coefficient (Γ_{actv}) alongside the input referred single element formulation given by (3) can be used as an alternative.

$$T = T_{\text{min}} + 4NT_0 \frac{|\Gamma_{\text{actv}} - \Gamma_{\text{opt}}|^2}{(1-|\Gamma_{\text{actv}}|^2)(1-|\Gamma_{\text{opt}}|^2)} \tag{3}$$

where the four noise parameters are represented by T_{min}, N and Γ_{opt}.

However, the simple insight given by (3) breaks down when $|\Gamma_{\text{actv}}| > 1$. This over unity condition was achieved by the MWA and EDA at several pointing directions in the $50-60$ MHz region due to the embedded reflection coefficient of the dipoles being close to unity and thus, the active reflection concept will not be discussed further in this paper aside from its links to the proposed framework found in Sect. II-C.

The remainder of this paper is organized as follows. Sect. II introduces the power wave based framework for computing receiver noise temperature and radiation efficiency, followed by results presented in Sect. III. Finally, concluding remarks are presented in Sect. IV.

II. Receiver and External Noise Calculation

With the aid of Fig. 3, let us consider the sources of noise that exist in the system. Firstly, there is the external noise which consists of noise from the sky due to naturally radiating cosmic sources, plus soil and thermal noise due to ohmic losses which form a net power flow that is incident onto the Antenna-Receiver Boundary represented by P_{inc}. Secondly, there is the internal noise due to the receiver which produces noise waves indicated by c_1 and c_2 towards both boundaries [18] and noise waves emerging from the load (not shown in diagram).

For subsequent analysis, it is implied that the properties of the boundary are as follows:

1) it only exists in the absence of a conjugately matched impedance with respect to the left and right hand side of the boundary,
2) the larger the mismatch, the more impenetrable the boundary is to the incident power wave,
3) it is temperature invariant. That is to say, the impedance on either side of the boundary are not affected by changes in physical temperature.

The available internal noise power ($P_{\text{av}}^{\text{rcv}}$) in (1) is calculated under the condition that no external noise is present. Conceptually, it implies that the antenna and load is immersed and kept at thermal equilibrium in a 0 K isotropic environment. For convenience, internal noise power delivered to a noiseless reference impedance (Z_0) matched load was computed rather than available power at the output.

Similar treatment is applied for the available external noise power ($P_{\text{av}}^{\text{amb}}$). The delivered external noise power under the condition that no internal noise is present was calculated. Here, it was assumed that the receiver and load is immersed and kept at 0 K while the antennas are kept at thermal equilibrium in an isotropic environment at T_0. Using the relation from (1), it can be shown that

$$T_{\text{rcv}} = \frac{P_{\text{int}}^{\text{out}}}{kG_T} \tag{4}$$

$$G_T = \frac{P_{\text{ext}}^{\text{out}}}{kT_0} \tag{5}$$

where $P_{\text{int}}^{\text{out}}$ is the noise power delivered to a noiseless matched load due to internal sources alone, $P_{\text{ext}}^{\text{out}}$ is the noise power delivered to a noiseless matched load due to external sources alone and G_T is the receiver transducer gain. The transducer gain is defined as the ratio of the delivered power by the network to the available power from the source (kT_0) [19].

This analysis is simple for a single isolated element as the quantity $P_{\text{int}}^{\text{out}}$ and $P_{\text{ext}}^{\text{out}}$ are easily computed. However, for an array of closely spaced antennas this is no longer the case. In this scenario, the antennas mutually couple and causes $P_{\text{int}}^{\text{out}}$ to deviate away from a single element case. The mechanisms that cause this overall effect are

1) changing of embedded antenna impedance,
2) coupling of outbound internal noise to neighbouring elements.

Furthermore, the computation of $P_{\text{ext}}^{\text{out}}$ and subsequently G_T for an array is not apparent at first glance due to the complex coupling paths.

A. Contribution of Internal Noise

Fig. 4 shows an example of noise paths that each noise wave will undergo for a two-element array. All these various paths can be accounted for using matrices to compute the outgoing receiver noise power at the boundaries as follows

$$\mathbf{A}_{\text{int}}^{\text{out}} = \mathbf{M}\hat{\mathbf{N}}\mathbf{M}^{H} \tag{6}$$

$$\mathbf{M} = \left[\mathbf{I} - \mathbf{S}^{\text{LNA}}\mathbf{S}^{\text{load}}\right]^{-1} \tag{7}$$

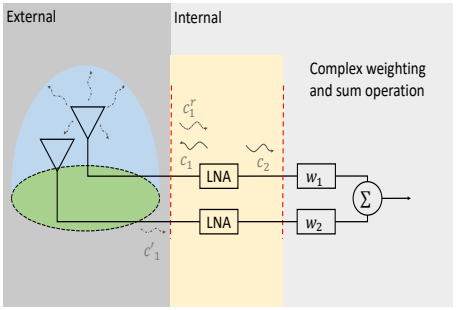

Figure 4. Coupling path of internal noise sources alone for a two-element array. The load as seen in Fig. 3 is now replaced with a complex weight and sum operator; however, the assumption of matched condition still remains. The output referred receiver noise temperature consists of reflected wave c_1^r, coupled wave to neighbouring element c_1' and noise wave c_2 emanating from the output of the receiver. While not shown, similar coupling paths occur at the lower branch.

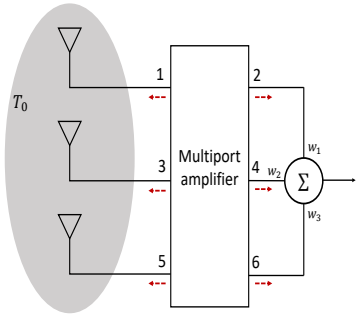

Figure 5. Example port numbering convention for a three element phased array. The odd numbered ports are the input ports of the multiport amplifier connected to antennas while the even numbered ports are the output ports. The noise waves due to internal sources alone emerging from the multiport network are described by (6) and are represented by dashed arrows. Noise waves emerging at the output ports undergo a weight (w_i) and sum operation.

where $\mathbf{A}_{\text{int}}^{\text{out}}$ is a $n \times n$ noise correlation Hermitian matrix of the outgoing noise power from each port (inputs and outputs) for an n-port network, $\hat{\mathbf{N}}$ is the noise correlation matrix of the multiport amplifier due to internal sources alone, $\mathbf{M}$ accounts for the mismatches in impedance, $\cdot^H$ is the Hermitian operator, $\mathbf{S}^{\text{LNA}}$ and $\mathbf{S}^{\text{load}}$ are the S-parameters of the multiport amplifier and the combined source (antenna) and load network attached to the multiport amplifier respectively. For completeness, the derivation of $\mathbf{M}$ can be found in Appendix A.

The noise power wave quantities computed by (6) can be visualized with the aid of Fig. 5. Each entry of the matrix contains information of outbound noise power waves (dashed arrows) due to internal sources alone after all coupling paths have been accounted for. The main diagonal contains the total noise power emerging from the network ports due to all c_1 and c_2 sources, while the cross terms contain the total amount of correlated power between port m and n.

To compute (6) correctly, $\mathbf{S}^{\text{LNA}}$, $\hat{\mathbf{N}}$ and $\mathbf{S}^{\text{load}}$ must have

a consistent port numbering convention. Based on the port numbering convention shown in Fig. 5, assuming that

1) the multiport amplifier is constructed from identical isolated 2-port element LNAs[2],
2) odd numbered ports are inputs and even number ports are outputs of the multiport amplifier network,
3) a reflectionless load (Z_0) is attached to the outputs of the LNAs then,

$$\mathbf{S}^{\mathrm{LNA}} = \begin{bmatrix} S_{11} & S_{12} & 0 & 0 & \dots \\ S_{21} & S_{22} & 0 & 0 & \dots \\ 0 & 0 & S_{11} & S_{12} & \dots \\ 0 & 0 & S_{21} & S_{22} & \dots \\ \vdots & \vdots & \vdots & \vdots & \ddots \\ 0 & 0 & 0 & 0 & \dots \\ 0 & 0 & 0 & 0 & \dots \end{bmatrix} \tag{8}$$

$$\hat{\mathbf{N}} = \begin{bmatrix} \langle |c_1|^2 \rangle & \langle c_1 c_2^* \rangle & 0 & 0 & \dots \\ \langle c_1^* c_2 \rangle & \langle |c_2|^2 \rangle & 0 & 0 & \dots \\ 0 & 0 & \langle |c_1|^2 \rangle & \langle c_1 c_2^* \rangle & \dots \\ 0 & 0 & \langle c_1^* c_2 \rangle & \langle |c_2|^2 \rangle & \dots \\ \vdots & \vdots & \vdots & \vdots & \ddots \\ 0 & 0 & 0 & 0 & \dots \\ 0 & 0 & 0 & 0 & \dots \end{bmatrix} \tag{9}$$

$$\mathbf{S}^{\mathrm{load}} = \begin{bmatrix} S_{11}^{\mathrm{ant}} & 0 & S_{12}^{\mathrm{ant}} & \dots & S_{1,n}^{\mathrm{ant}} & 0 \\ 0 & 0 & 0 & 0 & 0 & 0 \\ S_{21}^{\mathrm{ant}} & 0 & S_{22}^{\mathrm{ant}} & \dots & S_{2,n}^{\mathrm{ant}} & 0 \\ \vdots & 0 & \vdots & \ddots & \vdots & 0 \\ S_{m,1}^{\mathrm{ant}} & 0 & S_{m,2}^{\mathrm{ant}} & \dots & S_{mm}^{\mathrm{ant}} & 0 \\ 0 & 0 & 0 & 0 & 0 & 0 \end{bmatrix}. \tag{10}$$

For the computation of T_{rcv} seen in (4), the delivered noise power to loads at the output of the network are contained in the subset of matrix (6). As the input ports to be odd numbered, all the odd rows and columns to form a submatrix $[\mathbf{P}_{\mathrm{int}}^{\mathrm{out}}]_{m,n=2,4,\dots,m}$ can be removed. This submatrix is the correlation matrix that can be used for characterizing the amount of noise coupling that exists in correlating arrays. To get the total coupled noise power after the summer at the output of a phased array, this submatrix is multiplied by the beamformer weights as follow

$$P_{\mathrm{int}}^{\mathrm{out}} = \mathbf{w} \left[\mathbf{A}_{\mathrm{int}}^{\mathrm{out}}\right]_{m,n=2,4,\dots,m} \mathbf{w}^H \tag{11}$$

where $\mathbf{w}$ is a row vector containing the applied beamformer complex weights and $\{\mathbf{A}_{\mathrm{int}}^{\mathrm{out}}\}_{m,n=2,4,\dots,m}$ a submatrix containing even numbered rows and columns of (6). To ensure correct scaling in the calculated output power, the amplitude of $\mathbf{w}$ is scaled by the number of elements N such that $\sum_{i=1}^{N} |\mathbf{w}_i|^2 = 1$.

While the port convention in (8)-(10) is not unique, this convention was chosen as it is easier to construct/modify the required matrices. The focus now shifts to the computation of transducer gain for a phased array.

[2]Non-identical LNAs can also be used by modifying the entries in (8) and (9) to include the measured or simulated parameters of the non-identical LNA multiport network.

B. Contribution of External Noise

The outgoing power wave at the input and output of the multiport network due to power incident at the input ports is given by

$$\mathbf{A}_{\mathrm{ext}}^{\mathrm{out}} = \mathbf{M}\mathbf{S}^{\mathrm{LNA}}\hat{\mathbf{a}}\hat{\mathbf{a}}^H(\mathbf{S}^{\mathrm{LNA}})^H\mathbf{M}^H \tag{12}$$

where $\hat{\mathbf{a}}\hat{\mathbf{a}}^H$ contains the noise correlation matrix of the attached loads at the input and output of the LNA.

From the perspective of a matched load at the output ports of the multiport network, (12) describes the incident power from the network at the Receiver-Load Boundary. On the other hand, from the perspective of the source at the input ports, (12) describes the reflected power at the Antenna-Receiver Boundary (see Fig. 5).

For passive loads at thermal equilibrium with T_0 the noise correlation matrix $\hat{\mathbf{a}}\hat{\mathbf{a}}^H$ can be determined by Bosma's theorem [20] which states that

$$\hat{\mathbf{a}}\hat{\mathbf{a}}^H = kT_0 \left[\mathbf{I} - \mathbf{S}^{\mathrm{load}}(\mathbf{S}^{\mathrm{load}})^H\right]. \tag{13}$$

To simulate noiseless loads being attached at the output of the LNA, $\mathbf{I}$ in (13) must be replaced by

$$\mathbf{I}' = \begin{bmatrix} 1 & 0 & 0 & \dots & 0 & 0 \\ 0 & 0 & 0 & \dots & 0 & 0 \\ 0 & 0 & 1 & \dots & 0 & 0 \\ \vdots & 0 & 0 & \ddots & 0 & \vdots \\ 0 & 0 & 0 & \dots & 1 & 0 \\ 0 & 0 & 0 & \dots & 0 & 0 \end{bmatrix}. \tag{14}$$

The assumption of noiseless loads being attached to the output stage does not introduce a measurable change as a well-designed receiver chain should be dominated by LNA noise. The total delivered power from the network to Z_0 load is given by

$$P_{\mathrm{ext}}^{\mathrm{out}} = \mathbf{w} \left[\mathbf{A}_{\mathrm{ext}}^{\mathrm{out}}\right]_{m,n=2,4,\dots,m} \mathbf{w}^H \tag{15}$$

While not shown, (11) and (5) produces identical results to formulations found in [3] for the computation of incident noise power and transducer gain[3].

C. Links to Active Reflection Coefficient Concept

Before proceeding further, it is worth discussing links to theory presented in Sect. II-A and II-B to the commonly used active reflection formulation.

The output referred noise temperature calculated using the active reflection coefficient (3) relates to (11) via

$$\mathbf{w} \left[\mathbf{A}_{\mathrm{int}}^{\mathrm{out}}\right]_{m,n=2,4,\dots,m} \mathbf{w}^H = k\frac{1}{M}\sum_{i=1}^{M} T_i G_{T,i} \tag{16}$$

$$G_{T,i} = \frac{1 - |\Gamma_{\mathrm{actv},i}|^2}{|1 - S_{11}\Gamma_{\mathrm{actv},i}|^2}|S_{21}|^2 \tag{17}$$

where M is the number of elements in the array, T_i and $G_{T,i}$ are the input referred noise temperature and the transducer gain of the i^{th} element calculated using (3) and (17) respectively.

[3]In [3], the transducer gain is called effective available gain.

In addition, (15) can be calculated from (17) using

$$\mathbf{w}\left[\mathbf{A}_{\text{ext}}^{\text{out}}\right]_{m,n=2,4,\ldots,m}\mathbf{w}^H = \frac{1}{M}\sum_{i=1}^{M} G_{T,i}. \tag{18}$$

Substituting (16) and (18) into (4) and simplifying yields

$$T_{\text{rcv}} = \frac{\sum_{i=1}^{M} T_i G_{T,i}}{\sum_{i=1}^{M} G_{T,i}}. \tag{19}$$

The T_{rcv} calculated using (19) is exact. This calculation becomes an approximation when attempting to solely use (3) to infer the array noise temperature for cases when $G_{T,m} \neq G_{T,n} \cdots \neq G_{T,z}$ and/or $|\Gamma_{\text{actv}}|$ is greater than unity. Under this condition the average input referred noise temperature diverges away from the array noise temperature and therefore, it is more general to discuss the behaviour of the array's output referred noise temperature and the transducer gain separately.

D. Radiation Efficiency Calculation

Radiation efficiency (η_{rad}) of any antenna structure is defined by [4], [5]

$$\eta_{\text{rad}} = \frac{P_{\text{rad}}}{P_{\text{inj}}} \tag{20}$$

$$P_{\text{rad}} = \frac{1}{2Z_f}\int_0^{2\pi}\int_0^{\pi} \mathbf{E}_{\text{ff}} \cdot \mathbf{E}_{\text{ff}}^H \sin\theta d\theta d\phi \tag{21}$$

$$P_{\text{inj}} = \frac{1}{2}\mathbb{R}\{V_{\text{ant}} I^*\} \tag{22}$$

where P_{rad} is the total radiated power and P_{inj} is the total injected power into the antenna, Z_f is the free space impedance and $\mathbf{E}_{\text{ff}}$ is the far-field embedded element pattern (EEP) of the antenna as a function of θ and ϕ, V_{ant} is the voltage drop across the antenna, I is port current, $\{\cdot\}$ and $\{^*\}$ represents the element by element multiplication and complex conjugate operator respectively.

As noted in [5], the accuracy of this computation for high efficiency arrays is limited by the numerical sampling and integration of the far-field pattern used to compute P_{rad}. Furthermore, additional data such as port currents and voltage drop across the antenna terminals are required to be saved for the computation of P_{inj}. While the numerical integration is unavoidable, the aim is to reduce the amount of additional data required to be saved and reuse pre-existing data obtained during the characterization of the phased array such as embedded element pattern and S-parameter simulation. This provides the additional motivation for this section.

A different approach to compute η_{rad} is to use the pattern overlap integral (POI) method found in [4], which eliminates the need to know the injected power by reversing the problem from a transmit to receive antenna. The EEPs required for the POI method are based on open circuit condition of all neighbouring elements whereas, EEPs generated in [21] are based on loaded condition (LNA input impedance) of all elements. To reuse pre-existing EEPs generated in [21], POI formulation requires modification.

Fig. 6 shows an equivalent circuit of a transmit antenna. The total radiated power captured in the far-field pattern is due to the power dissipated by Z'_{ant}. This means that the far-field

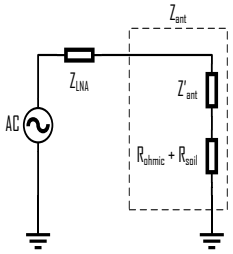

Figure 6. Simplified equivalent circuit of a lossy antenna loaded with LNA impedance in transmit mode. The Z_{ant} is the antenna impedance as obtained by S-parameter simulation/measurement or can be obtained via the port currents from simulation as both the excitation voltage and LNA impedance are known. The ohmic and soil losses are modelled as a resistor but in practice, these losses have a more complex form.

EEP does not directly contain the knowledge of any losses. By reversing the problem to receive mode, the noise power delivered to Z_{LNA} by Z'_{ant} at a nominal physical temperature T_0 can be determined for a given EEP generated in transmit mode. The total noise power delivered to the array terminated with identical LNA impedances given that the antenna sees an homogeneous sky at T_0 is given by

$$P'_{\text{LNA}} = kT_0 \mathbf{w}\mathbf{L}^{sky}\mathbf{w}^H \tag{23}$$

$$L^{sky}_{m,n} = \mathbb{R}\{\frac{Z_f}{Z_{\text{LNA}}\lambda^2}\}\int_0^{2\pi}\int_0^{\pi} \mathbf{l}_{\text{p},m} \cdot \mathbf{l}^H_{\text{p},n} \sin\theta d\theta d\phi \tag{24}$$

where $\mathbf{L}^{sky}$ is the noise correlation matrix due to homogeneous sky that is based on the POI formulation, Z_f is the free space impedance, λ is the wavelength in meters, and $\mathbf{l}_{\text{p},i}$ relates the incident electromagnetic wave to the voltage seen at the load of the i^{th} element as a function of θ and ϕ. The derivation of $\mathbf{l}_{\text{p}}$ can be found in Appendix B.

The total noise power delivered to Z_{LNA} by Z_{ant} at physical temperature of T_0 can be calculated using Bosma's theorem [20] or Twiss's theorem [4]. For our purposes, Bosma's theorem is a more convenient choice as it uses S-parameter natively. This is where the versatility of [15] comes into play. The formulation can easily be modified to calculate the total delivered external noise power at the input of the LNAs using

$$P_{\text{LNA}} = \mathbf{w}\{\mathbf{A}^{\text{inc}}_{\text{ext}} - \mathbf{A}^{\text{out}}_{\text{ext}}\}_{m,n=1,3,\ldots,m}\mathbf{w}^H \tag{25}$$

$$\mathbf{A}^{\text{inc}}_{\text{ext}} = \mathbf{M}'\hat{\mathbf{a}}\hat{\mathbf{a}}^H\mathbf{M}'^H \tag{26}$$

$$\mathbf{M}' = \left[\mathbf{I} - \mathbf{S}^{\text{load}}\mathbf{S}^{\text{LNA}}\right]^{-1} \tag{27}$$

where $\mathbf{A}^{\text{inc}}_{\text{ext}}$ is the incident noise power to the LNA due to external sources alone, $\mathbf{A}^{\text{out}}_{\text{ext}}$ and $\hat{\mathbf{a}}\hat{\mathbf{a}}^H$ were previously computed in (12) and (13).

The radiation efficiency is then given by

$$\eta_{\text{rad}} = \frac{P'_{\text{LNA}}}{P_{\text{LNA}}} \tag{28}$$

This is effectively how the POI method works. For verification, it was shown in [22] that the radiation efficiency calculated using (28) and (20) produced identical results within

numerical error. The result is reproduced here with additional verification using perfect electric conductor (PEC) materials.

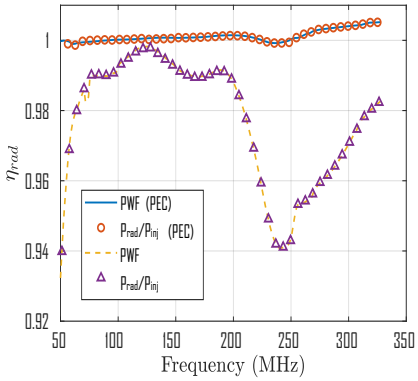

Figure 7. Calculated efficiency of the MWA at zenith. The PWF and $P_{\rm rad}/P_{\rm inj}$ curve represents the efficiency calculated using the power wave framework and (20) respectively. The EEPs used to compute both results are based on prior simulation presented in [21], whereby the radiation efficiency is solely due to soil losses as all the metallic elements used during simulation were perfect electric conductors (PEC). For further validation, the MWA was re-simulated with PEC infinite ground to ensure that $\eta_{\rm rad} = 1$ is obtained with the PWF and (20).

The efficiency of the MWA as seen in Fig. 7 was calculated using (28). For result verification, these values were compared against those obtained using (20). The numerical integration on the radiation pattern was performed at a resolution of 0.2° for both methods. Additionally, previous raw simulation data was reprocessed to obtain the port currents required for the computation of $P_{\rm inj}$.

For the PEC case, the efficiency reported was as high as 100.5% which is due to the limitations of the simulation package. As demonstrated in [5], the efficiency obtained using Method-of-Moments (MoM) based solver such as FEKO for PEC materials ranges from 100% to 100.7%. Efficiency calculation was not done for the EDA as the array was simulated using perfect electric conductor (PEC) material over infinite ground and due to lengthy simulation time, it was not repeated with lossy materials.

III. Results

A. Receiver Temperature

The MWA tile and EDA were simulated using an electromagnetic simulator FEKO to obtain the S-parameter of the arrays. The expected $T_{\rm rcv}$ and $\eta_{\rm rad}$ was calculated for the two arrays using (30) and the measured noise and S-parameters of the LNA obtained in [16]. The calculated receiver noise temperature was then compared to values obtained via astronomical drift scan method as seen in [10]–[12].

Fig. 8 shows the comparison between the calculated and observed receiver noise temperature of the MWA. The observations were performed on the 9th June 2014 by setting all the MWA beamformes to point overhead (at zenith) and allowing astronomical sources to drift through the MWA's beam. The

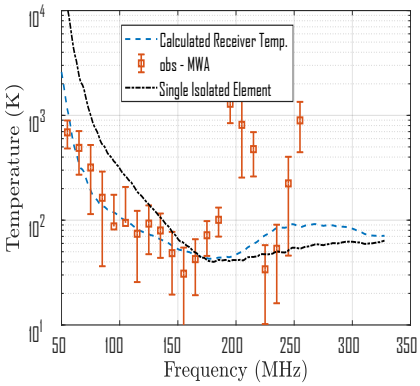

Figure 8. Comparison between the calculated (dashed curve) and observed receiver noise temperature of MWA. The mean and standard deviation of the observed receiver noise temperature represented by the data points was calculated over 128 tiles. A single isolated element result represented by the dot-dash curve is presented for comparison.

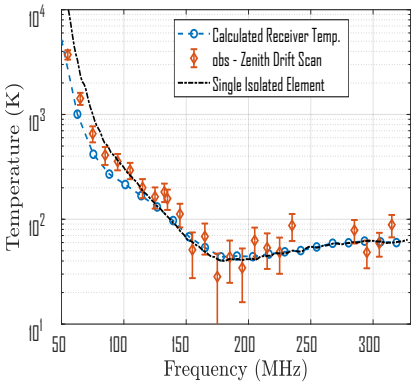

Figure 9. Comparison between the calculated and observed receiver noise temperature of the EDA. The calculated result represented by the dashed curve is based on a fully perfect electric conductor (PEC) array and therefore the efficiency calculation was not performed nor included. A single isolated element result represented by the dot-dash curve is also presented for comparison. The observed receiver noise temperature represented by the data points shows the mean and standard deviation of the receiver noise temperature taken over a 1 MHz bin size.

expected power detected as a function of frequency (ν) by a phased array is given by

$$P(\nu) = g(\nu)k\left[\eta_{\rm rad}T_{\rm ant}(\nu) + T'_{\rm rcv}(\nu)\right] \quad (29)$$

$$T'_{\rm rcv}(\nu) = T_{\rm rcv}(\nu) + \left[1 - \eta_{\rm rad}(\nu)\right]T_a \quad (30)$$

where $g(\nu)$ is the overall power gain of the array signal chain which includes the transducer gain, cable losses, secondary amplication stage etc, $T_{\rm ant}$ is the antenna temperature due to sky noise and T_a is the ambient temperature.

The quantity $T'_{\rm rcv}(\nu)$ can be obtained by first modelling the

predicted power as

$$P'(\nu) = g(\nu)k\left[\eta_{\rm rad}T_{\rm ant}^{\rm model}(\nu) + T'_{\rm rcv}(\nu)\right] \quad (31)$$

and $T_{\rm ant}^{\rm model}$ is estimated as

$$T_{\rm ant}^{\rm model}(\nu) = \frac{\int_\Omega B(\nu,\theta,\phi)T(\nu,\theta,\phi)d\Omega}{\int_\Omega B(\nu,\theta,\phi)d\Omega} \quad (32)$$

where $B(\nu,\theta,\phi) = E(\nu,\theta,\phi)_{\rm ff}\cdot E(\nu,\theta,\phi)_{\rm ff}^H$ is the simulated far-field power pattern as a function of θ and ϕ, $T(\nu,\theta,\phi)$ is the sky brightness temperature obtained from "Haslam Map" [23] at frequency ν, which has been scaled down from the original 408 MHz to lower frequencies by multiplying by a factor $(\nu/408\ \text{MHz})^{-2.55}$.

Least square optimization is then performed on the predicted $P'(\nu)$ with the observed $P(\nu)$ to solve for $g(\nu)$ and $T'_{\rm rcv}(\nu)$ respectively. Based on (31) the power received by every tile is expected to be proportional to $T_{\rm ant}^{\rm model} + T'_{\rm rcv}(\nu)$, assuming that the sky model used in (32) is a good representation of the true sky (accuracy of sky model is of order $\approx 10\%$). This relation has been identified to hold best for the 12 to 14 hours range of the Local Sidereal Time (LST) [4] (see also [10] for a more detailed justification of LST range selection procedure). Once the calculated values had been obtained, this model is fitted to measured data using least squares to solve for $g(\nu)$ and $T'_{\rm rcv}(\nu)$.

The frequency ranges of 170 MHz to 220 MHz and 240 MHz and above show radio frequency interference (RFI) which causes the observed $T'_{\rm rcv}$ to increase dramatically. The error bars generated are based on the standard deviation of $T'_{\rm rcv}$ calculated over 128 MWA tiles used during observation.

Fig 9 shows the comparison between the calculated and observed $T'_{\rm rcv}(\nu)$ of the EDA. Detailed receiver noise temperature calculation from astronomical observation can be found in [10].

B. Transducer Gain

The most interesting result that emerged from this calculation is the reduction of $T'_{\rm rcv}(\nu)$ over the single element at lower frequencies. Firstly, to verify that the results presented remain physically valid, G_T was recalculated for a single isolated element given that the antenna was conjugately matched at all frequencies to the LNA's input impedance. This calculation sets the absolute upper limit which the G_T of the array must not exceed as it would imply the source is delivering more power than the available source power (kT_0). This maximum value was compared to the mean and standard deviation of the array's G_T over all 197 pointing angles in Fig. 11 and showed that the calculated array G_T remains physically valid.

Similar effects have been observed in the EDA results seen in Fig. 9. However, the reduction of $T'_{\rm rcv}(\nu)$ when compared to a single element was not as drastic as the transducer gain did not increase as much as the MWA tile. Standard deviations in Fig. 12 clearly show that in general MWA has a higher transducer gain when compared to the EDA, however the G_T of an MWA tile varies over pointing angles more than the EDA.

[4] LST is an hour angle between vernal equinox and local meridian

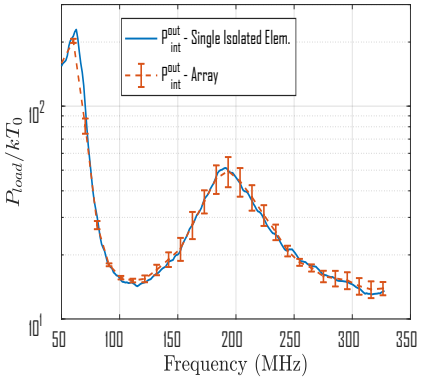

Figure 10. Delivered noise power to a Z_0 matched load due to internal sources alone normalized to kT_0. The solid line represents the delivered noise power by a single isolated MWA element whereas the dashed line represents the mean and standard deviation of power delivered by the MWA array over 197 optimal MWA pointings.

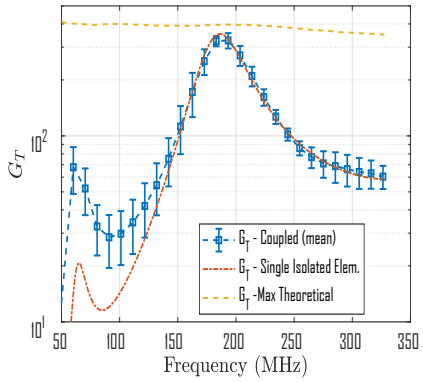

Figure 11. Comparison of the transducer gain achievable by the MWA LNA. The theoretical maximum transducer gain (dashed curve) of a single element was obtained by placing conjugately matched load at all frequencies at the input of the LNA. The data points represent the mean and standard deviation of the tile's G_T obtained over all 197 optimal pointing angles. For comparison, G_T of a single isolated element (dot-dash curve) is shown.

The mechanism causing the increasing of G_T can be investigated by plotting the delivered power to the array due to external sources alone as shown in Fig. 13 and 14. It can be observed that additional power is delivered to the array due to mutual coupling at 50 to 170 MHz. It can be clearly seen that for the MWA, the reduction in $T_{\rm rcv}$ is due to more external noise power (signal of interest) being delivered to the array. In contrast, the EDA has less coupling, hence less additional power is delivered to the array which leads to less reduction in $T_{\rm rcv}$.

The higher levels of power delivered due to mutual coupling (cross terms) makes the array sensitive to complex weightings applied by the beamformer at the output. This result

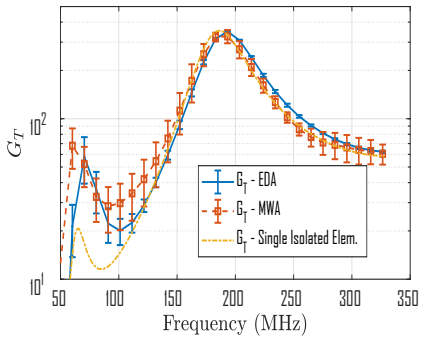

Figure 12. Comparison of mean and standard deviation of calculated transducer gain of the MWA and EDA over 197 optimal MWA pointings. The G_T of a single isolated element is represented by the dashed curve for reference.

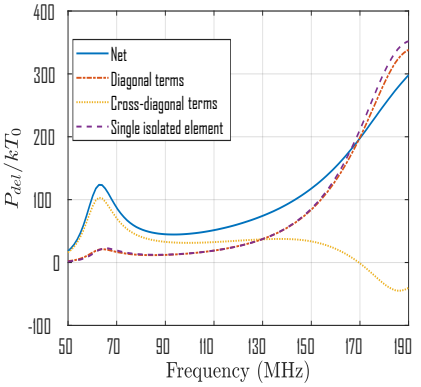

Figure 13. External noise power due to homogeneous sky delivered to the Z_0 matched load at the output of MWA tile normalized to kT_0. The dashed curve represents the total delivered power due to external sources for a single isolated element, the dotted curve represents the additional delivered power to the MWA tile due to mutual coupling (cross terms of (12)) while the dot-dash curve represents external noise power that is directly delivered to the array (diagonal terms of (12)). The solid curve is the net sum of both the additional and direct power delivered to the MWA tile. The negative value represents power loss due to destructive interference of the noise wave due to mutual coupling.

is consistent with the trend observed in Fig. 12 whereby, the MWA experiences larger changes to G_T with changing pointing angles. Such high level of coupling can be explained by the physical layout of the elements. The element spacing within an MWA tile is 1.1 m from centre to centre whereas for the EDA, the average element spacing is ≈ 1.5 m.

Based on these results, it can be reasoned that the reduction of T_{rcv} is possible by optimizing the element layout (increased coupling) without having to optimize the LNA over the entire frequency band. Meaning, the LNA could be optimized to cover the mid to high frequency band whereas, the array layout could be optimized to take advantage of the effects of mutual coupling to improve the T_{rcv} at lower frequencies (50 - 140 MHz).

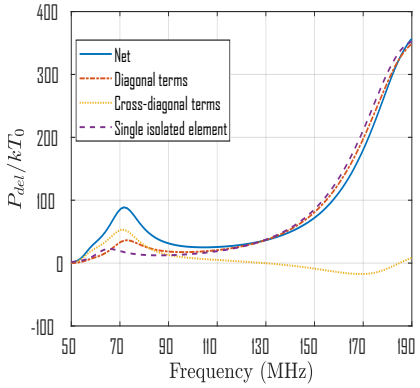

Figure 14. External noise power due to homogeneous sky delivered to the Z_0 matched load at the output of the EDA normalized to kT_0. The dashed curve represents the total delivered power due to external sources for a single isolated element, the dotted curve represents the additional delivered power to the EDA due to mutual coupling (cross terms of (12)) while the dot-dash curve represents external noise power that is directly delivered to the array (diagonal terms of (12)). The solid curve is the net sum of both the additional and direct power delivered to the EDA. The negative value represents power loss due to destructive interference of the noise wave due to mutual coupling.

Layout optimization only works if the dominant contribution is due to external noise. That is to say, the if the internal noise is not fluctuating much as a function of complex weightings (see Fig. 10), then increasing the amount of external noise through mutual coupling is beneficial for lowering T_{rcv}. In the domain where internal noise dominates, increased mutual coupling is not desirable as this will lead to an increase in T_{rcv}. The only way to decrease T_{rcv} in this case without changing the antenna design is to optimize the LNA. This reasoning comes with a caveat that it only applies to the MWA dipole design. Other antenna designs were not analyzed which could potentially lead to a different conclusion found here.

IV. Conclusion

This paper presents a power wave based framework for analyzing the receiver noise temperature of an aperture array which includes the effects of mutual coupling. Using a combination of measured noise parameters and simulated S-parameters of the MWA tile and the EDA to calculate the receiver noise temperature. The calculated T_{rcv} obtained using the proposed PWF was compared with measured T_{rcv} obtained via astronomical observations and was found to be in good agreement between the two for both the MWA tile and the EDA. It was observed that due to higher mutual coupling in the $50-140$ MHz region, the MWA has a lower receiver noise when compared to the EDA. The decrease in T_{rcv} was due to the increase in transducer gain.

The increased G_T at lower frequencies was due to the additional external noise power delivered to the array via coupling. This improvement was seen for both the MWA tile and the EDA but since the MWA tile has higher coupling, the

T_{rcv} was lower than the EDA. In addition, higher fluctuation in G_T as a function of pointing angles with higher levels of coupling. For this reason, mutual coupling could either be a hindrance or aid when it comes to reducing T_{rcv} depending on whether the internal or external noise dominates the overall contribution.

Additionally, it was demonstrated that the PWF is able to make use of embedded element patterns to calculate the efficiency of the array without the need for re-simulation. In conclusion, the PWF presented in [15] is a general method suited to compute receiver noise temperature for multiport devices and extendable to include phased arrays as demonstrated in this paper. This framework can be utilized to optimize and characterize future generation telescopes such as the Square Kilometre Array [7].

APPENDIX A
DERIVATION OF M MATRIX

The standard S-parameter representation of incident and reflected wave are as shown below.

$$\mathbf{a} = \mathbf{S}^{\text{LNA}}\mathbf{b} + \mathbf{n} \tag{33}$$

$$\mathbf{b} = \mathbf{S}^{\text{load}}\mathbf{a} \tag{34}$$

where $\mathbf{a}$ is a vector containing the outgoing wave from the the input and output ports of multiport amplifier indicated by the red arrows in Fig. 5, $\mathbf{n}$ is a vector containing the noise waves c_1 and c_2, $\mathbf{b}$ is the vector containing the reflected wave due to the attached load at the input and output ports of the network, $\mathbf{S}^{\text{LNA}}$ and $\mathbf{S}^{\text{load}}$ are the S-parameters of the network and loads respectively.

The noise wave vector $\mathbf{n}$ appears in (33) to represent noise wave originating from the network. By substituting (34) into (33) and solving for $\mathbf{a}$ yields,

$$\mathbf{a} = \left[1 - \mathbf{S}^{\text{LNA}}\mathbf{S}^{\text{load}}\right]^{-1}\mathbf{n} \tag{35}$$

$$\mathbf{a} = \mathbf{M}\mathbf{n}. \tag{36}$$

The outgoing power due to internal noise alone is simply given by

$$\mathbf{A}_{\text{int}}^{\text{out}} = \mathbf{a}\mathbf{a}^H \tag{37}$$

$$= \mathbf{M}\hat{\mathbf{N}}\mathbf{M}^H \tag{38}$$

where $\hat{\mathbf{n}}\hat{\mathbf{n}}^H = \hat{\mathbf{N}}$.

If desired, $\mathbf{n}$ can be shifted to (34) and this represents noise originating from the loads (external noise). Following the exact derivation shown above will yield (12). Solving for $\mathbf{b}$ and repeating steps above on the other hand, will produce expression seen in (26) and (27).

APPENDIX B
DERIVATION OF $\mathbf{l}_{\text{p}}$

The quantity $\mathbf{l}_{\text{p}}$ is defined as follows

$$V_{\text{LNA}} = \frac{Z_L}{Z_L + Z_{tx}}\mathbf{l}_{\text{eff}}\mathbf{E}^{\text{inc}} \tag{39}$$

$$= \mathbf{l}_{\text{p}}\mathbf{E}^{\text{inc}} \tag{40}$$

where the effective length ($\mathbf{l}_{\text{eff}}$) is given by [6]

$$\mathbf{l}_{\text{eff}} = -j\frac{4\pi}{\omega\mu_0 I_{tx}}\bar{\mathbf{E}} \tag{41}$$

where V_{LNA} is the voltage dropped across the input of the LNA, $\mathbf{E}^{\text{inc}}$ is the incident plane wave, Z_L and Z_{tx} are the impedance of the load and antenna under transmit condition respectively, ω is the angular frequency, μ_0 is the permeability of free space, I_{tx} is the port current under transmit condition and $\bar{\mathbf{E}} = \left[E_{\hat{\theta}}^{tx}, E_{\hat{\phi}}^{tx}\right]$ is embedded element radiation pattern.

Realising that I_{tx} is simply

$$I_{tx} = \frac{V_{tx}}{Z_L + Z_{tx}} \tag{42}$$

and by substituting (42) into (41) to obtain

$$\mathbf{l}_{\text{p}} = -j\frac{4\pi}{\omega\mu_0}\frac{Z_L}{Z_L + Z_{tx}}\frac{1}{\frac{V_{tx}}{Z_L+Z_{tx}}}\left[E_{\hat{\theta}}^{tx}, E_{\hat{\phi}}^{tx}\right]^T \tag{43}$$

$$= -j\frac{4\pi}{\omega\mu_0}\frac{Z_L}{V_{tx}}[E_{\hat{\theta}}^{tx}, E_{\hat{\phi}}^{tx}]^T \tag{44}$$

where V_{tx} is the source voltage applied in simulation which produces the corresponding $\bar{\mathbf{E}}$ and Z_{tx} is the impedance of the antenna given that all other surrounding elements are terminated with a load impedance Z_L.

ACKNOWLEDGEMENT

The author would like to thank Randall Wayth for useful feedback on this manuscript. The author acknowledges the contribution of an Australian Government Research Training Program Scholarship in supporting this research. The International Centre for Radio Astronomy Research (ICRAR) is a Joint Venture of Curtin University and The University of Western Australia, funded by the Western Australian State government. The MWA Phase II upgrade project was supported by Australian Research Council LIEF grant LE160100031 and the Dunlap Institute for Astronomy and Astrophysics at the University of Toronto. This scientific work makes use of the Murchison Radio-astronomy Observatory, operated by CSIRO. We acknowledge the Wajarri Yamatji people as the traditional owners of the Observatory site. Support for the operation of the MWA is provided by the Australian Government (NCRIS), under a contract to Curtin University administered by Astronomy Australia Limited. We acknowledge the Pawsey Supercomputing Centre which is supported by the Western Australian and Australian Governments.

REFERENCES

[1] K. F. Warnick, B. Woestenburg, L. Belostotski, and P. Russer, "Minimizing the noise penalty due to mutual coupling for a receiving array," *IEEE Transactions on Antennas and Propagation*, vol. 57, no. 6, pp. 1634–1644, June 2009.

[2] M. V. Ivashina, R. Maaskant, and B. Woestenburg, "Equivalent system representation to model the beam sensitivity of receiving antenna arrays," *IEEE Antennas and Wireless Propagation Letters*, vol. 7, pp. 733–737, 2008.

[3] L. Belostotski, B. Veidt, K. F. Warnick, and A. Madanayake, "Low-noise amplifier design considerations for use in antenna arrays," *IEEE Transactions on Antennas and Propagation*, vol. 63, no. 6, pp. 2508–2520, June 2015.

[4] K. F. Warnick, M. V. Ivashina, R. Maaskant, and B. Woestenburg, "Unified definitions of efficiencies and system noise temperature for receiving antenna arrays," *IEEE Transactions on Antennas and Propagation*, vol. 58, no. 6, pp. 2121–2125, June 2010.

[5] R. Maaskant, "Analysis of large antenna systems," Ph.D. dissertation, Department of Electrical Engineering, Technische Universiteit Eindhoven, 2010.

[6] K. F. Warnick, R. Maaskant, M. V. Ivashina, D. B. Davidson, and B. D. Jeffs, *Phased Arrays for Radio Astronomy, Remote Sensing, and Satellite Communications*, ser. EuMA High Frequency Technologies Series. Cambridge University Press, 2018.

[7] P. E. Dewdney, P. J. Hall, R. T. Schilizzi, and T. J. L. W. Lazio, "The square kilometre array," *Proceedings of the IEEE*, vol. 97, no. 8, pp. 1482–1496, Aug 2009.

[8] S. J. Tingay, R. Goeke, J. D. Bowman, D. Emrich, S. M. Ord *et al.*, "The Murchison Widefield Array: The Square Kilometre Array Precursor at Low Radio Frequencies," *PASA*, vol. 30, p. e007, Jan. 2013.

[9] R. B. Wayth, S. J. Tingay, C. M. Trott, D. Emrich, M. Johnston-Hollitt *et al.*, "The Phase II Murchison Widefield Array: Design overview," *PASA*, vol. 35, Nov. 2018.

[10] R. Wayth, M. Sokolowski, T. Booler, B. Crosse, D. Emrich *et al.*, "The Engineering Development Array: A Low Frequency Radio Telescope Utilising SKA Precursor Technology," *PASA*, vol. 34, p. e034, Aug. 2017.

[11] J. D. Bowman, D. G. Barnes, F. H. Briggs, B. E. Corey, M. J. Lynch *et al.*, "*Field Deployment of Prototype Antenna Tiles for the Mileura Widefield Array Low Frequency Demonstrator*," *AJ*, vol. 133, pp. 1505–1518, Apr. 2007.

[12] A. T. Sutinjo, T. M. Colegate, R. B. Wayth, P. J. Hall, E. de Lera Acedo *et al.*, "Characterization of a low-frequency radio astronomy prototype array in western australia," *IEEE Transactions on Antennas and Propagation*, vol. 63, no. 12, pp. 5433–5442, Dec 2015.

[13] A. Chippendale, D. Hayman, and S. Hay, "Measuring noise temperatures of phased-array antennas for astronomy at csiro," *Publications of the Astronomical Society of Australia*, vol. 31, p. 14, 01 2014.

[14] A. P. Chippendale, A. J. Brown, R. J. Beresford, G. A. Hampson, R. D. Shaw *et al.*, "Measured aperture-array noise temperature of the mark ii phased array feed for askap," in *2015 International Symposium on Antennas and Propagation (ISAP)*, Nov 2015, pp. 1–4.

[15] J. Randa, "Noise characterization of multiport amplifiers," *IEEE Transactions on Microwave Theory and Techniques*, vol. 49, no. 10, pp. 1757–1763, Oct 2001.

[16] A. T. Sutinjo, D. C. X. Ung, and B. Juswardy, "Cold-source noise measurement of a differential input single-ended output low-noise amplifier connected to a low-frequency radio astronomy antenna," *IEEE Transactions on Antennas and Propagation*, vol. 66, no. 10, pp. 5511–5520, Oct 2018.

[17] D. Ung, A. Sutinjo, and D. Davidson, "Evaluating receiver noise temperature of a radio telescope in the presence of mutual coupling: Comparison of current methodologies," in *2019 13th European Conference on Antennas and Propagation (EuCAP)*, March 2019, pp. 1–3.

[18] S. W. Wedge and D. B. Rutledge, "Wave techniques for noise modeling and measurement," *IEEE Transactions on Microwave Theory and Techniques*, vol. 40, no. 11, pp. 2004–2012, Nov 1992.

[19] G. Gonzalez, *Microwave Transistor Amplifiers: Analysis and Design*. Prentice Hall, 1997, ch. 2.

[20] S. W. Wedge and D. B. Rutledge, "Noise waves and passive linear multiports," *IEEE Microwave and Guided Wave Letters*, vol. 1, no. 5, pp. 117–119, May 1991.

[21] R. Wayth, T. Colegate, M. Sokolowski, A. Sutinjo, and D. Ung, "Advanced, efficient primary beam modeling for the murchison widefield array radio telescope," in *2016 International Conference on Electromagnetics in Advanced Applications (ICEAA)*, Sept 2016, pp. 431–434.

[22] D. Ung, A. Sutinjo, D. Davidson, M. Johnston-Hollitt, and S. Tingay, "Radiation efficiency calculation of the murchison widefield array using a power wave based framework," in *2019 IEEE International Symposium on Antennas and Propagation and USNC-URSI Radio Science Meeting*, July 2019, pp. 401–402.

[23] C. G. T. Haslam, C. J. Salter, H. Stoffel, and W. E. Wilson, "A 408 MHz all-sky continuum survey. II - The atlas of contour maps," *Astronomy and Astrophysics Supplement Series*, vol. 47, p. 1, Jan. 1982.

Appendix B

Statement of Attribution

Table B.1: Statement of attribution for "Evaluating receiver noise temperature of a radio telescope in the presence of mutual coupling: Comparison of current methodologies".

	Concept and Design	Data Acquisition and Method	Data Conditioning and Manipulation	Analysis	Interpretation and Discussion	Final Approval	Total % contribution
co-Author 1: Daniel Ung	75%	100%	100%	100%	80%	0%	76%
Co Author 1 Acknowledgement I acknowledge that these represent my contribution to the above research output Signed:							
co-Author 2: Adrian Sutinjo	25%	0%	0%	0%	20%	70%	19%
Co Author 2 Acknowledgement I acknowledge that these represent my contribution to the above research output Signed:							
co-Author 3: David B. Davidson	0%	0%	0%	0%	0%	30%	5%
Co Author 3 Acknowledgement I acknowledge that these represent my contribution to the above research output Signed:							
Total %	100%	100%	100%	100%	100%	100%	100%

Table B.2: Statement of attribution for "Radiation efficiency calculation of the Murchison Widefield Array using a power wave based framework".

	Concept and Design	Data Acquisition and Method	Data Conditioning and Manipulation	Analysis	Interpretation and Discussion	Final Approval	Total % contribution
co-Author 1: Daniel Ung	80%	100%	100%	100%	80%	0%	77%
Co Author 1 Acknowledgement I acknowledge that these represent my contribution to the above research output Signed:							
co-Author 2: Adrian Sutinjo	20%	0%	0%	0%	20%	45%	14%
Co Author 2 Acknowledgement I acknowledge that these represent my contribution to the above research output Signed:							
co-Author 3: David B. Davidson	0%	0%	0%	0%	0%	25%	4%
Co Author 3 Acknowledgement I acknowledge that these represent my contribution to the above research output Signed:							
co-Author 4: Melanie Johnston-Hollitt	0%	0%	0%	0%	0%	25%	4%
Co Author 4 Acknowledgement I acknowledge that these represent my contribution to the above research output Signed:							
co-Author 5: Steven Tingay	0%	0%	0%	0%	0%	5%	1%
Co Author 5 Acknowledgement I acknowledge that these represent my contribution to the above research output Signed:							
Total %	100%	100%	100%	100%	100%	100%	100%

Table B.3: Statement of attribution for "Noise Temperature of Phased Array Radio Telescope: The Murchison Widefield Array and the Engineering Development Array".

	Concept and Design	Data Acquisition and Method	Data Conditioning and Manipulation	Analysis	Interpretation and Discussion	Final Approval	Total % contribution
co-Author 1: Daniel Ung	75%	75%	90%	90%	70%	0%	67%
Co Author 1 Acknowledgement I acknowledge that these represent my contribution to the above research output Signed:							
co-Author 2: Marcin Sokolowski	0%	25%	10%	10%	10%	30%	13%
Co Author 2 Acknowledgement I acknowledge that these represent my contribution to the above research output Signed:							
co-Author 3: Adrian Sutinjo	25%	0%	0%	0%	15%	35%	13%
Co Author 3 Acknowledgement I acknowledge that these represent my contribution to the above research output Signed:							
co-Author 4: David B. Davidson	0%	0%	0%	0%	5%	35%	7%
Co Author 4 Acknowledgement I acknowledge that these represent my contribution to the above research output Signed:							
Total %	100%	100%	100%	100%	100%	100%	100%

Appendix C

Network Parameters

The characteristics of a linear network can be determined by measuring the voltage and current response at the ports of the network under specific loading condition at the ports. For example, the impedance matrix (Z-parameters) is defined by [59]

$$\begin{bmatrix} V_1 \\ V_2 \\ \vdots \\ V_N \end{bmatrix} = \begin{bmatrix} Z_{11} & Z_{12} & \cdots & Z_{1N} \\ Z_{21} & & & \vdots \\ \vdots & & & \vdots \\ Z_{N1} & \cdots & \cdots & Z_{NN} \end{bmatrix} \begin{bmatrix} I_1 \\ I_2 \\ \vdots \\ I_N \end{bmatrix} \tag{C.1}$$

$$\mathbf{v} = \mathbf{Zi} \tag{C.2}$$

and

$$Z_{ij} = \left. \frac{V_i}{I_j} \right|_{I_k=0, k\neq j} \tag{C.3}$$

where $\mathbf{v}$ and $\mathbf{i}$ is a column vector containing the voltages and currents at the port and the condition $I_k = 0, k \neq j$ implies open circuit condition at all other ports except for the j^{th} port.

Another set of parameters known as Y-parameters (admittance matrix) is

defined by [59]

$$\begin{bmatrix} I_1 \\ I_2 \\ \vdots \\ I_N \end{bmatrix} = \begin{bmatrix} Y_{11} & Y_{12} & \cdots & Y_{1N} \\ Y_{21} & & & \vdots \\ \vdots & & & \vdots \\ Y_{N1} & \cdots & \cdots & Y_{NN} \end{bmatrix} \begin{bmatrix} V_1 \\ V_2 \\ \vdots \\ V_N \end{bmatrix} \tag{C.4}$$

$$\mathbf{i} = \mathbf{Y}\mathbf{v} \tag{C.5}$$

and

$$Y_{ij} = \left.\frac{I_i}{V_j}\right|_{V_k=0, k\neq j} \tag{C.6}$$

where the condition $V_k = 0, k \neq j$ implies short circuit condition at all other ports except for the j^{th} port.

Each parameter has its own advantages and disadvantages and is selected based on the typical operation of the network and the desired quantity to be computed. For the purposes of this thesis, we will be predominantly interested in power transfer and S-parameters are most suited for this application [60]. The scattering matrix is defined by [59–61]

$$\mathbf{b} = \mathbf{S}\mathbf{a} \tag{C.7}$$

and

$$S_{ij} = \left.\frac{b_i}{a_j}\right|_{a_k=0, k\neq j} \tag{C.8}$$

where $\mathbf{b} = [b_1, b_2, \ldots b_n]^T$ and $\mathbf{a} = [a_1, a_2, \ldots a_n]^T$ are column vectors containing the reflected and incident voltage wave respectively, the condition $b_k = 0, k \neq j$ implies no reflected voltage wave at all other ports except the j^{th} port and this is achieved by terminating all other ports with matched reference impedance.

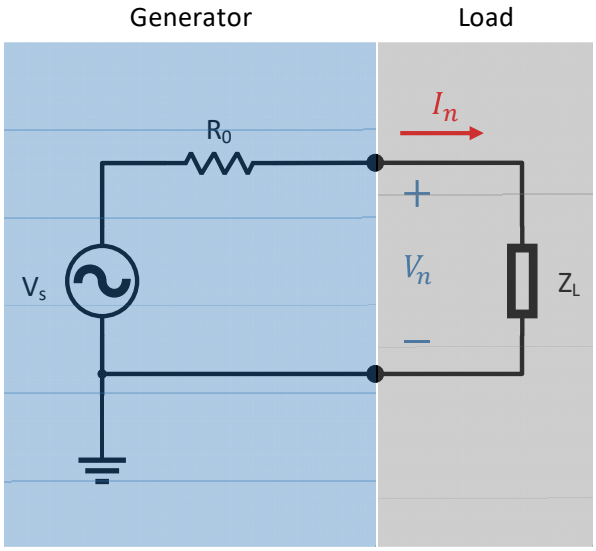

Figure C.1: Circuit diagram of a equivalent one-port network.

The formulation of S-parameter begins by defining the voltage and current at the network ports as follows

$$v_n = \sqrt{Z_{s,n}}\,(v_{i,n} + v_{r,n}) \tag{C.9}$$

$$i_n = \frac{1}{\sqrt{Z_{s,n}}}\,(v_{i,n} + v_{r,n}) \tag{C.10}$$

where v_n and i_n is the defined measured voltage and current at the n^{th} port as a combination of incident $v_{i,n}$ and reflected $v_{r,n}$ voltage wave with respect to the reference source impedance Z_s.

It then follows that the incoming and reflected voltage wave is given by [61]

$$a_n = v_{i,n} = \frac{V_n + Z_s I_n}{2\sqrt{|\mathbb{R}\mathrm{e}\{Z_{s,n}\}|}} \tag{C.11}$$

$$b_n = v_{r,n} = \frac{V_n - Z_s^* I_n}{2\sqrt{|\mathbb{R}\mathrm{e}\{Z_{s,n}\}|}} \tag{C.12}$$

where a_n and b_n is now used to represent the incident and reflected wave which follows the standard notation found in literature and have units of $\{\text{volt} - \text{amps}\}^{1/2}$

and .* represents a complex conjugate operator.

While in general the reference impedance Z_s can be complex with either a positive or negative real part, we shall restrict it to a positive real resistance R_0 as this reflects the mode of operation in subsequent discussions. To observe relationship of a_n and b_n to power representation, let us consider a simple equivalent one-port circuit as shown in Fig. C.1. If we substitute voltage $V_n = V_s - I_s R_0$ into (C.11) and (C.12) and take the squared of the magnitude we obtain

$$|a_n|^2 = \frac{|V_s|^2}{4R_0} \tag{C.13}$$

$$|b_n|^2 = \frac{|V_s|^2}{4R_0} + |I_n|^2 R_0 - \mathbb{R}\mathrm{e}\{V_s I_n^*\} \tag{C.14}$$

We can see that (C.13) represents the maximum available power that can be delivered by the source and (C.14) represents the reflected power which consists of power dissipated by the source load and undelivered power due to mismatch between source and load impedance. The difference of $|a_n|^2 - |b_n|^2$ is the power delivered to the load.

The conversion between parameters are as follows [59]

$$\mathbf{Y} = \mathbf{Z}^{-1} \tag{C.15}$$

$$\mathbf{Z} = Z_s \left[\mathbf{I} + \mathbf{S}\right] \left[\mathbf{I} - \mathbf{S}\right]^{-1} \tag{C.16}$$

$$\mathbf{S} = \left[\mathbf{Z} + Z_s \mathbf{I}\right]^{-1} \left[\mathbf{Z} - Z_s \mathbf{I}\right] \tag{C.17}$$

where $\mathbf{I}$ is an identity matrix.

Appendix D

Thermal Noise

Noise refers to interference or unwanted signal that interferes with the desired incoming signal to be measured. It is akin to two people attempting to converse in a noisy environment such as a restaurant. A noisy environment will interfere with the communication process and depending on the noise level, communication would be impossible. Likewise, it is the same with aperture arrays attempting to detect cosmic signals. If the receiver is noisy then detecting such signal would be impossible.

It is therefore important to quantify noise such that we can predict system performance. To do this, the concept of noise temperature is introduced. A resistor R that is heated to a physical temperature of T is able to supply a maximum power given by Planck's equation [62]

$$P = kT \left[\frac{\frac{hf}{kT}}{e^{\frac{hf}{kT}} - 1} \right] \tag{D.1}$$

where $h = 6.62607015 \times 10^{-34}$ is Plank's constant [63], $k = 1.380649 \times 10^{-23}$ Boltzmann's constant [63] and f is the frequency in Hz.

For special cases where $kT \gg hf$, $P \approx kT$ known as the Rayleigh-Jeans approximation ($P_{R-J} \approx kT$) can be used. This provides a simple relation of physical temperature to maximum power delivered by the resistor to a noiseless

matched load (available power). This relation will be used when referring 'noise temperature' of a device/network in subsequent discussions however, the noise temperature in this case will not represent the physical temperature of the actual device/network. Rather, we use this relation to quantify device/network's power spectral density which produces the same power spectral density as resistor at a physical temperature T.

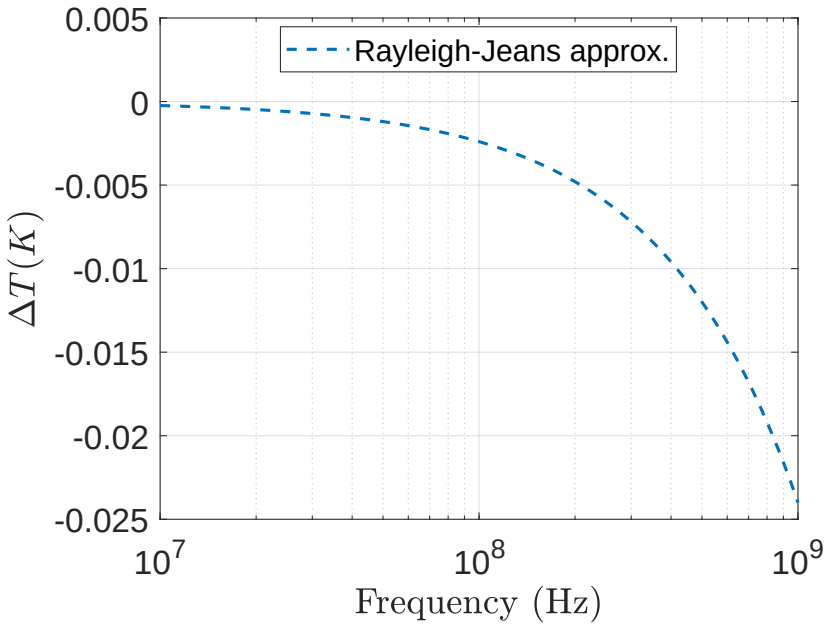

Figure D.1: Difference between physical temperature and noise temperature calculated using Rayleigh-Jeans approximation (dashed curve).

Fig. D.1 shows the difference between physical temperature and noise temperature calculated using Rayleigh-Jeans approximation at a physical temperature of 30 °C. We see that the Rayleigh-Jeans approximation is valid at our frequency range of interest with $|\Delta T|$ less than 0.03 K.

Appendix E

Power flux Density of Homogeneous Sky

The power delivered to the load attached to a receiving antenna is given by

$$P_{\text{load}} = A_r S_{\text{inc}} \tag{E.1}$$

Given that the flux density of a radiating black-body is given by [64]

$$S_{\text{inc}} = \frac{2k}{\lambda^2} T_B \Delta\Omega \tag{E.2}$$

where T_B and Ω is the temperature and solid angle of the radiating black-body respectively.

To find the total power delivered to the load given that T_B is distributed as a function of θ and ϕ, we simply substitute (E.2) into (E.1) and integrate over Ω as follows

$$P_{\text{load}} = \frac{2k}{\lambda^2} \int_{\Omega} A_r(\theta, \phi) T_B(\theta, \phi) \; d\Omega \tag{E.3}$$

Bibliography

[1] H. T. Friis, "Karl Jansky: His Career at Bell Telephone Laboratories," *Science*, vol. 149, no. 3686, pp. 841–842, 1965. [Online]. Available: http://www.jstor.org/stable/1716039

[2] J. Hey, "Commentaries on electrical disturbances apparently of extraterrestrial origin," *CC*, no. 23, p. 16, June 1984. [Online]. Available: http://garfield.library.upenn.edu/classics1984/A1984SS75500001.pdf

[3] K. G. Jansky, "Directional Studies of Atmospherics at High Frequencies," *Proceedings of the Institute of Radio Engineers*, vol. 20, no. 12, pp. 1920–1932, Dec 1932.

[4] K. G. Jansky, "Electrical Disturbances Apparently of Extraterrestrial Origin," *Proceedings of the Institute of Radio Engineers*, vol. 21, no. 10, pp. 1387–1398, Oct 1933.

[5] G. Reber, "Cosmic Static," *Proceedings of the IRE*, vol. 30, no. 8, pp. 367–378, Aug 1942.

[6] G. Reber, "Cosmic Static," *Proceedings of the IRE*, vol. 36, no. 10, pp. 1215–1218, Oct 1948.

[7] F. Bacciotti, E. Whelan, and L. Testi, *Jets from Young Stars II: Clues from High Angular Resolution Observations*, ser. Lecture Notes in Physics. Springer Berlin Heidelberg, 2007. [Online]. Available: https://books.google.com.au/books?id=TphwyyMgu1oC

[8] M. H. Cohen, "Genesis of the 1000-foot Arecibo dish," *Journal of Astronomical History and Heritage*, vol. 12, pp. 141–152, Jul. 2009.

[9] R. Nan, D. Li, C. Jin, Q. Wang, L. Zhu *et al.*, "The Five-Hundred Aperture Spherical Radio Telescope (FAST) Project," *International Journal of Modern Physics D*, vol. 20, no. 6, pp. 989–1024, Jan 2011.

[10] C. J. Jin, R. D. Nan, and H. Q. Gan, "The FAST telescope and its possible contribution to high precision astrometry," *Proceedings of the International Astronomical Union*, vol. 3, no. S248, p. 178–181, 2007.

[11] D. Emerson, "Why Single-Dish?" in *Single-Dish Radio Astronomy: Techniques and Applications*, ser. Astronomical Society of the Pacific Conference Series, S. Stanimirovic, D. Altschuler, P. Goldsmith, and C. Salter, Eds., vol. 278, Dec. 2002, pp. 27–43.

[12] A. R. Thompson, J. M. Moran, and G. W. Swenson, Jr., *Interferometry and Synthesis in Radio Astronomy, 3rd Edition*. Springer, Cham, 2017.

[13] S. Stanimirovic, "Short-Spacings Correction from the Single-Dish Perspective," in *Single-Dish Radio Astronomy: Techniques and Applications*, ser. Astronomical Society of the Pacific Conference Series, S. Stanimirovic, D. Altschuler, P. Goldsmith, and C. Salter, Eds., vol. 278, Dec. 2002, pp. 375–396.

[14] R. Braun and R. A. M. Walterbos, "A solution to the short spacing problem in radio interferometry," *AAP*, vol. 143, pp. 307–312, Feb. 1985.

[15] D. R. DeBoer, R. G. Gough, J. D. Bunton, T. J. Cornwell, R. J. Beresford *et al.*, "Australian SKA Pathfinder: A High-Dynamic Range Wide-Field of View Survey Telescope," *Proceedings of the IEEE*, vol. 97, no. 8, pp. 1507–1521, Aug 2009.

[16] S. J. Tingay, R. Goeke, J. D. Bowman, D. Emrich, S. M. Ord *et al.*, "The Murchison Widefield Array: The Square Kilometre Array Precursor at Low Radio Frequencies," *PASA*, vol. 30, p. e007, Jan. 2013.

[17] R. B. Wayth, S. J. Tingay, C. M. Trott, D. Emrich, M. Johnston-Hollitt *et al.*, "The Phase II Murchison Widefield Array: Design overview," *PASA*, vol. 35, Nov. 2018.

[18] R. Ekers, "The History of the Square Kilometre Array (SKA) - Born Global," *arXiv e-prints*, p. arXiv:1212.3497, Dec 2012.

[19] M. Sokolowski, T. Colegate, A. Sutinjo, D. Ung, R. Wayth *et al.*, "Calibration and Stokes Imaging with Full Embedded Element Primary Beam Model for the Murchison Widefield Array," *Publications of the Astronomincal Society of Australia (PASA)*, vol. 34, 11 2017.

[20] O. M. Smirnov, "Revisiting the radio interferometer measurement equation. II. Calibration and direction-dependent effects," *AAP*, vol. 527, p. A107, Mar. 2011.

[21] J. M. Wrobel and R. C. Walker, "Sensitivity," in *Synthesis Imaging in Radio Astronomy II*, ser. Astronomical Society of the Pacific Conference Series, G. B. Taylor, C. L. Carilli, and R. A. Perley, Eds., vol. 180, Jan 1999, p. 171.

[22] "Murchison Widefield Array," http://mwatelescope.org/team/people, accessed: 2018-05-25.

[23] D. Ung, A. Sutinjo, and D. Davidson, "Evaluating Receiver Noise Temperature of a Radio Telescope in the Presence of Mutual Coupling: Comparison of Current Methodologies," in *2019 13th European Conference on Antennas and Propagation (EuCAP)*, March 2019, pp. 1–3.

[24] K. F. Warnick, M. V. Ivashina, R. Maaskant, and B. Woestenburg, "Unified Definitions of Efficiencies and System Noise Temperature for Receiving Antenna Arrays," *IEEE Transactions on Antennas and Propagation*, vol. 58, no. 6, pp. 2121–2125, June 2010.

[25] "IEEE Standard for Definitions of Terms for Antennas," *IEEE Std 145-2013 (Revision of IEEE Std 145-1993)*, pp. 1–50, March 2014.

[26] K. F. Warnick, R. Maaskant, M. V. Ivashina, D. B. Davidson, and B. D. Jeffs, *Phased Arrays for Radio Astronomy, Remote Sensing, and Satellite Communications*, ser. EuMA High Frequency Technologies Series. Cambridge University Press, 2018.

[27] H. C. Ko, "On the Reception of Quasi-Monochromatic, Partially Polarized Radio Waves," *Proceedings of the IRE*, vol. 50, no. 9, pp. 1950–1957, Sep. 1962.

[28] I. 80000-2:2019(E), "Quantities and units - Part 2: Mathematics," International Organization for Standardization, Geneva, CH, Standard, Aug. 2019.

[29] P. Hannan, "The element-gain paradox for a phased-array antenna," *IEEE Transactions on Antennas and Propagation*, vol. 12, no. 4, pp. 423–433, July 1964.

[30] D. F. Kelley, "Embedded element patterns and mutual impedance matrices in the terminated phased array environment," in *2005 IEEE Antennas and Propagation Society International Symposium*, vol. 3A, July 2005, pp. 659–662 vol. 3A.

[31] K. F. Warnick and B. D. Jeffs, "Gain and Aperture Efficiency for a Reflector Antenna With an Array Feed," *IEEE Antennas and Wireless Propagation Letters*, vol. 5, pp. 499–502, 2006.

[32] R. Hu and S. Weinreb, "A novel wide-band noise-parameter measurement method and its cryogenic application," *IEEE Transactions on Microwave Theory and Techniques*, vol. 52, no. 5, pp. 1498–1507, May 2004.

[33] J. Lange, "Noise Characterization of Linear Twoports in Terms of Invariant Parameters," *IEEE Journal of Solid-State Circuits*, vol. 2, no. 2, pp. 37–40, Jun 1967.

[34] L. Belostotski, "No Noise Is Good Noise: Noise Matching, Noise Canceling, and Maybe a Bit of Both for Wide-Band LNAs," *IEEE Microwave Magazine*, vol. 17, no. 8, pp. 28–40, Aug 2016.

[35] S. W. Wedge and D. B. Rutledge, "Wave techniques for noise modeling and measurement," *IEEE Transactions on Microwave Theory and Techniques*, vol. 40, no. 11, pp. 2004–2012, Nov 1992.

[36] J. Randa, "Noise characterization of multiport amplifiers," *IEEE Transactions on Microwave Theory and Techniques*, vol. 49, no. 10, pp. 1757–1763, Oct 2001.

[37] L. Belostotski, B. Veidt, K. F. Warnick, and A. Madanayake, "Low-Noise Amplifier Design Considerations For Use in Antenna Arrays," *IEEE Transactions on Antennas and Propagation*, vol. 63, no. 6, pp. 2508–2520, June 2015.

[38] K. F. Warnick, B. Woestenburg, L. Belostotski, and P. Russer, "Minimizing the Noise Penalty Due to Mutual Coupling for a Receiving Array," *IEEE Transactions on Antennas and Propagation*, vol. 57, no. 6, pp. 1634–1644, June 2009.

[39] H. A. Haus, W. R. Atkinson, G. M. Branch, W. B. Davenport, W. H. Fonger *et al.*, "Representation of Noise in Linear Twoports," *Proceedings of the IRE*, vol. 48, no. 1, pp. 69–74, Jan 1960.

[40] R. Maaskant, "Analysis of large antenna systems," Ph.D. dissertation, Department of Electrical Engineering, Technische Universiteit Eindhoven, 2010.

[41] D. Ung, A. Sutinjo, D. Davidson, M. Johnston-Hollitt, and S. Tingay, "Radiation Efficiency Calculation of the Murchison Widefield Array Using a Power Wave Based Framework," in *2019 IEEE International Symposium on Antennas and Propagation and USNC-URSI Radio Science Meeting*, July 2019, pp. 401–402.

[42] D. Ung, M. Sokolowski, A. T. Sutinjo, and D. B. Davidson, "Noise Temperature of Phased Array Radio Telescope: The Murchison Widefiled Array and the Engineering Development Array," *IEEE Transactions on Antennas and Propagation*, Submitted.

[43] J. D. Kraus, *Antennas*, 2nd ed., A. E. Elken, Ed. McGraw-Hill, 1988.

[44] S. W. Wedge and D. B. Rutledge, "Noise waves and passive linear multiports," *IEEE Microwave and Guided Wave Letters*, vol. 1, no. 5, pp. 117–119, May 1991.

[45] R. Wayth, T. Colegate, M. Sokolowski, A. Sutinjo, and D. Ung, "Advanced, efficient primary beam modeling for the Murchison Widefield Array radio telescope," in *2016 International Conference on Electromagnetics in Advanced Applications (ICEAA)*, Sept 2016, pp. 431–434.

[46] A. T. Sutinjo, D. C. X. Ung, and B. Juswardy, "Cold-Source Noise Measurement of a Differential Input Single-Ended Output Low-Noise Amplifier Connected to a Low-Frequency Radio Astronomy Antenna," *IEEE Transactions on Antennas and Propagation*, vol. 66, no. 10, pp. 5511–5520, Oct 2018.

[47] A. Sutinjo, J. O'Sullivan, E. Lenc, R. B. Wayth, S. Padhi *et al.*, "Understanding instrumental Stokes leakage in Murchison Widefield Array polarimetry," *Radio Science*, vol. 50, pp. 52–65, Jan. 2015.

[48] M. Sokolowski, T. Colegate, A. T. Sutinjo, D. Ung, R. Wayth *et al.*, "Calibration and Stokes Imaging with Full Embedded Element Primary Beam Model for the Murchison Widefield Array," *PASA*, vol. 34, p. e062, Nov 2017.

[49] A. T. Sutinjo, T. M. Colegate, R. B. Wayth, P. J. Hall, E. de Lera Acedo *et al.*, "Characterization of a Low-Frequency Radio Astronomy Prototype Array in Western Australia," *IEEE Transactions on Antennas and Propagation*, vol. 63, pp. 5433–5442, Dec. 2015.

[50] S. K. Padhi, B. Juswardy, and M. Josh, "Microwave characterization of MRO soil," internal Report.

[51] J. D. Bowman, D. G. Barnes, F. H. Briggs, B. E. Corey, M. J. Lynch *et al.*, "Field Deployment of Prototype Antenna Tiles for the Mileura Widefield Array Low Frequency Demonstrator," *AJ*, vol. 133, pp. 1505–1518, Apr. 2007.

[52] R. Wayth, M. Sokolowski, T. Booler, B. Crosse, D. Emrich *et al.*, "The Engineering Development Array: A Low Frequency Radio Telescope Utilising SKA Precursor Technology," *PASA*, vol. 34, p. e034, Aug. 2017.

[53] A. T. Sutinjo, T. M. Colegate, R. B. Wayth, P. J. Hall, E. de Lera Acedo *et al.*, "Characterization of a Low-Frequency Radio Astronomy Prototype Array in Western Australia," *IEEE Transactions on Antennas and Propagation*, vol. 63, no. 12, pp. 5433–5442, Dec 2015.

[54] C. G. T. Haslam, C. J. Salter, H. Stoffel, and W. E. Wilson, "A 408 MHz all-sky continuum survey. II - The atlas of contour maps," *Astronomy and Astrophysics Supplement Series*, vol. 47, p. 1, Jan. 1982.

[55] A. E. E. Rogers, P. Pratap, E. Kratzenberg, and M. A. Diaz, "Calibration of active antenna arrays using a sky brightness model,"

Radio Science, vol. 39, no. 2, 2004. [Online]. Available: https://agupubs.onlinelibrary.wiley.com/doi/abs/10.1029/2003RS003016

[56] G. Gonzalez, *Microwave Transistor Amplifiers: Analysis and Design*. Prentice Hall, 1997, ch. 2.

[57] M. Sokolowski, R. B. Wayth, and M. Lewis, "The statistics of low frequency radio interference at the Murchison Radio-astronomy Observatory," in *2015 IEEE Global Electromagnetic Compatibility Conference (GEMCCON)*, Nov 2015, pp. 1–6.

[58] P. E. Dewdney, P. J. Hall, R. T. Schilizzi, and T. J. L. W. Lazio, "The Square Kilometre Array," *Proceedings of the IEEE*, vol. 97, no. 8, pp. 1482–1496, Aug 2009.

[59] D. Pozar, "Microwave Network Analysis," in *Microwave Engineering, 4th Edition*. Wiley, 2011, ch. 4, pp. 165–228.

[60] H. Carlin, "The Scattering Matrix in Network Theory," *IRE Transactions on Circuit Theory*, vol. 3, no. 2, pp. 88–97, June 1956.

[61] K. Kurokawa, "Power Waves and the Scattering Matrix," *IEEE Transactions on Microwave Theory and Techniques*, vol. 13, no. 2, pp. 194–202, March 1965.

[62] A. R. Kerr and J. Randa, "Thermal Noise and Noise Measurements; a 2010 Update," *IEEE Microwave Magazine*, vol. 11, no. 6, pp. 40–52, Oct 2010.

[63] D. B. Newell, F. Cabiati, J. Fischer, K. Fujii, S. G. Karshenboim *et al.*, "The CODATA 2017 values of h, e, k, and N_A for the revision of the SI," *Metrologia*, vol. 55, no. 1, pp. L13–L16, jan 2018. [Online]. Available: https://iopscience.iop.org/article/10.1088/1681-7575/aa950a

[64] T. L. Wilson, K. Rohlfs, and S. Hüttemeister, *Tools of Radio Astronomy*. Springer, Berlin, Heidelberg, 2013.

Every reasonable effort has been made to acknowledge the owners of copyright material. I would be pleased to hear from any copyright owner who has been omitted or incorrectly acknowledged.